國立交通大學

加速器光源科技與應用學程（材料組）

博士論文

鉍鐵氧化物薄膜之製備及特性研究

Physical characteristics and fabrication of $BiFeO_3$ ferroelectric thin films

研究生：劉晏廷

指導教授：陳三元 博士

共同指導教授：李信義 博士

中華民國 一百零三 年 六 月

鉍鐵氧化物薄膜之製備及特性研究

Physical characteristics and fabrication of $BiFeO_3$ ferroelectric thin films

研究生 ： 劉晏廷
指導教授 ： 陳三元 博士
共同指導教授 ： 李信義 博士

國立交通大學
加速器光源科技與應用學程（材料組）
博士論文

A Dissertation
College of Engineering, National Chiao Tung University,
Submitted to the Graduate Faculty
Of the
National Chiao Tung University
of Graduate Program for Science and Technology of Accelerator Light Source

by
Yen-Ting Liu

In partial fulfillment of the Requirements
For the Degree of
DOCTOR OF PHILOSOPHY
June 2014
Hsinchu, Taiwan, Republic of China

鉍鐵氧化物薄膜之製備及特性研究

研究生：劉晏廷　　　　　　　　　　　　　　　指導教授：陳三元 博士

李信義 博士

國立交通大學加速器光源科技與應用博士學位學程（材料組）

摘要

本論文在研究多鐵性鐵酸鉍（鉍鐵氧化物）材料之晶體結構與鐵電特性。首先我們利用射頻磁控濺鍍系統成長單層之鐵酸鉍薄膜於鍍有鎳酸鑭(導電材料)緩衝層之矽（001）單晶基板上。由高解析之X光繞射量測分析得知，其薄膜沿著(001)面擁有高度優選指向之方向性。在成長溫度範圍為400-600℃，隨著成長的溫度提高其結晶性也跟著變佳。根據X光反射率的擬合分析結果顯示，鐵酸鉍薄膜的密度較塊材小了些許。其殘留極化值隨著成長溫度的提高而提升，此與X光繞射分析之結果相互印證，由此得知鐵電特性與結晶性及電子密度有著正相關性。此實驗結果我們得知：鐵酸鉍薄膜的鐵電特性大小的主要貢獻來自於其薄膜結晶性。

根據第一個研究主題結果顯示：對於鐵電薄膜材料而言，其薄膜的結晶性是一項相當重要的議題；為了提升鐵酸鉍薄膜之鐵電特性，成長具有磊晶品質的薄膜為一適當的研究方向。因此第二個研究主題是利用射頻磁控濺鍍系統，成長具有對稱性結構鐵酸鉍/鎳酸鑭之人工超晶格磊晶薄膜於鈮摻雜鈦酸鍶的單晶基板上。超晶格薄膜包含了 6-30 個週期，其單一層厚

度為1.7-8.5奈米，而總膜厚則固定在100奈米，其成長溫度範圍為560-810℃，實驗結果顯示此超晶格結構之薄膜具備了令人滿意的結晶結構及應變效應。此種鐵電材料與導電材料所形成之超晶格，可做為探討在單一超晶格結構內，應變對於鐵酸鉍薄膜層之鐵電特性的影響。利用高解析之X光繞射實驗，顯示除了主要的繞射峰兩側外皆有顯著的衛星峰；以及由X光反射率曲線之 Kiessig 干涉條紋中可明顯分辨出超晶格之特徵峰，證實此濺鍍薄膜確實具有超晶格結構。此薄膜的層狀結構亦由X光反射率、飛行時間二次離子質譜儀及高解析穿透式電子顯微鏡分析得到確認，而且所有的實驗皆得到一致性結果。在所有的成長溫度及不同疊層厚度下，超晶格薄膜在其鈦酸鍶(002)布拉格繞射峰周圍皆有顯著的主繞射峰與衛星峰，代表著於鈦酸鍶基板上可形成高品質之鐵酸鉍/鎳酸鑭人工超晶格結構。由高解析之X光繞射量測結果得知無論是提高沈積溫度或是減少疊層厚度，皆會提升其超晶格薄膜之結晶性，並沿著 c 軸方向有著拉伸應力以及沿著試片表面有著壓縮應變的存在。

超晶格薄膜之殘留極化值顯示出與單層鐵酸鉍薄膜具有相同的趨勢；其極化值隨著沈積溫度的增加而增加，在溫度 660 ℃ 時達到最大值。在量測頻率為 0.5 及 1 千赫茲時，遲滯曲線顯現出極大的漏電流存在；極化值隨著量測頻率的增加而減少。

因射頻磁控濺鍍系統有著先天上的物理極限，因此在最後的研究主題

裡我們利用原子層沈積系統，成長厚度小於 10 奈米，具有高度(001)優選指向之超薄鐵酸鉍薄膜於鎳酸鑭緩衝層之矽(001)基板上，同時我們也利用射頻磁控濺鍍系統成長相同厚度之樣品作為對照。結合了氣流中斷及鉍與鐵前驅物之交替式反應，使原子層沈積系統為一優越成長三元化合物之方法。根據X光繞射分析，在沈積溫度低於550°C 時所生成的相只有鐵酸鉍。藉由同步輻射X光繞射異常精細結構光譜，透過鐵酸鉍(001)繞射訊號可以確認其鍵結之價數。利用X光光電子能譜術可得到其薄膜之成分比，結果顯示利用原子層沈積法所成長之鐵酸鉍成分計量比射頻磁控濺鍍法來的正確，並符合繞射異常精細結構之結果。利用高解析穿透視電子顯微鏡影像鑒別薄膜之層狀結構與表面形貌，由原子層沈積法所成長之薄膜呈現相當程度的覆蓋範圍，且較射頻磁控濺鍍系統來的一致性。因此利用原子層沈積法所成長出之鐵酸鉍薄膜具有絕佳的低漏電特性，與射頻磁控濺鍍系統相比大幅的改善了一千倍之多，使得這種方法更適合用於製造鐵電隨機存取記憶體元件。由遲滯曲線可得知最大的殘留極化值為 $2Pr = 2.0\ \mu C\ cm^{-2}$ 。

Physical characteristics and fabrication of $BiFeO_3$ ferroelectric thin films

Student: Yen-Ting Liu Advisor: Dr. San-Yuan Chen

Dr. Hsin-Yi Lee

Graduate Program for Science and Technology of Accelerator Light Source National Chiao Tung University

ABSTRACT

To study the crystal structure and ferroelectric properties of multiferroic material $BiFeO_3$ (BFO), we first investigated the BFO thin film as a single layer grown on a Si (001) substrate coated with $LaNiO_3$ (LNO) with a RF magnetron sputtering (RF-sputtering) system. The measurements of high-resolution X-ray diffraction (HRXRD) showed a highly orientated crystal structure along (001) direction. The crystal quality increases with increasing deposition temperature in a range of 400-600 ^{o}C; according to the fitted results of X-ray reflectivity (XRR), the densities of BFO thin films were slightly less than their bulk values. Increasing the deposition temperature increases the remnant polarization, and is consistent with the results of XRD, indicating that the ferroelectric property has a positive relation with the crystal quality and electron density. The results indicate that the crystal quality dominates the ferroelectric property of BFO thin films.

According to the first theme, the crystal quality is an important issue of a ferroelectric material; an epitaxial thin film is a proper direction to improve the ferroelectric property of a BFO thin film. The second theme is about an artificial superlattice of multiferroic BFO and conductive LNO grown epitaxially, with a

RF-sputtering system, on a single-crystal substrate of (001) Nb-doped $SrTiO_3$ (STO) in a range 560-810 ºC. The superlattice structure contains the features of a satisfactory crystal structure and the strain effect in a single thin-film structure. The superlattice contained 6-30 periods of symmetric BFO/LNO bi-layers with each layer of thickness 1.7-8.5 nm. The total thickness of the films was fixed at ~100 nm. A ferroelectric and conductive superlattice material serves for an investigation of the strain dependence of the ferroelectric properties of BFO layers in a superlattice structure. The formation of the superlattice structure is confirmed from the appearance of satellite peaks on both sides of the main peak from the HRXRD pattern. The appearance of superlattice peaks separated by Kiessig fringes in the XRR curve. The layer structure is confirmed with XRR, a time-of-flight secondary-ion mass spectrometer (TOF-SIMS), and a high-resolution transmission electron microscope (HRTEM). All results are consistent with one another. The clearly discernible main peak and satellite peaks on both sides of the substrate peak around the (002) STO Bragg peak indicate the high-quality BFO/LNO artificial superlattice structure formed on a STO substrate at all deposition temperatures and with various thicknesses of sublayer. HRXRD measurements showed that these superlattice films become subject to greater tensile stress along the *c*-axis and compressive strain in the in-plane direction, and possess increased crystalline quality with both increasing temperature of deposition and decreasing thickness of the sublayer.

The remanent polarization of the superlattice showed the same behavior as the single-layer BFO thin film; the polarization increases with increasing deposition and approaches a maximum at 660 ºC. The hysteresis loops showed a large current leakage at frequencies 0.5 and 1 kHz; the polarization decreases with increasing measuring frequency.

Because of the physical limitation of RF-sputtering, the final theme is about highly (001)-oriented ultrathin $BiFeO_3$ films of total thickness less than 10 nm deposited on Si (001) substrates via deposition of atomic layers (ALD) with a $LaNiO_3$ buffer. A radio-frequency (RF)-sputtered sample of the same thickness was prepared for comparison. The ALD, combined with interrupted flow and an exchange reaction between Bi and Fe precursors, provides a superior method to grow ternary compounds. According to X-ray diffraction, upon deposition at a temperature less than 550 °C, the only phase in the film is $BiFeO_3$. Anomalous fine structure from synchrotron X-ray diffraction certifies the valence bonding through the (001) diffraction signal. The stoichiometric ratio of $BiFeO_3$ obtained from X-ray photoelectron spectra indicates that ALD has a proportion much improved over the RF preparation, in agreement with the diffraction anomalous fine structure. The use of high-resolution transmission electron and atomic-force microscopes shows that the layer structure and morphology from ALD presented a satisfactory coverage, more conformal than that with the RF method. The $BiFeO_3$ thin film deposited with ALD shows improved leakage at least 1000 times with respect to the RF preparation, making this method suitable for the fabrication of ferroelectric random-access memory devices. From the hysteresis loop, the largest remanent polarization is $2Pr$ = 2.0 μC cm^{-2}.

致謝

首先我要感謝國家同步輻射研究中心 李信義博士，同時也是我的指導教授。我在大學三年級時就已進入李博士的實驗室做專題研究，在當時受到李博士的照顧也學到了許多。雖然沒有應屆考上研究所但李博士依然鼓勵我再接再厲，隔年順利考上國立交通大學加速器光源科技與應用學程，也進入李博士的實驗室做研究。李博士花費極大的心力在我身上，細心的指導我，教導我實驗的方法、論文的寫作以及做人的態度，真的很感謝李博士，沒有他就沒有我。也要感謝 陳三元博士，在這段時間大力的支持我、指導我，讓我能順利完成我的博士論文。也要感謝 杜繼舜博士、黃嘉宏博士、周振嘉博士以及林志明博士使得本論文的內容更加地圓融與充實，同時也給我許多新的啟發。

此外要感謝 古慶順博士，在我的碩博士生涯給予我許多幫助與指導在他身上學到研究的態度與新的思維，並且時常給予我適時幫助在我低潮時給予我鼓勵與方向，讓我有動力繼續向前。也要感謝 劉恆睿博士與邱上睿博士，在我剛進研究所時對一切都還很陌生，帶領我踏入這個未知的環境讓我有所依靠，在此衷心的感謝。還要感謝實驗室的所有學弟妹的幫忙，最後要感謝我的家人，在我求學階段一直以來對我的照顧與關心，讓我無後顧之憂的專注於課業與研究上，謝謝您們。

Contents

摘要…………………………………………………………………………. .i

Abstract…………………………………………………………………...….iv

致謝…………………………………………………………..……………...vii

Table Captions…………………………………………………………………xi

Figure Captions………..………………………………………………..……..xii

Chapter 1 Introduction…………………………………………………...……….1

Chapter 2 Literature review……………………………………………………6

2.1 Multiferroic material…………………………………..……..……6

2.1.1 Ferroelectric properties……………………………………………...6

2.1.2 Ferroelectric hysteresis loop and polarization switching………......8

2.2 Structure and physical properties of $BiFeO_3$ (BFO)…………………11

2.2.1 Crystal structure of BFO………………………………….……11

2.2.2 Physical properties of BFO……………………………………..12

2.3 Structure and physical properties of $LaNiO_3$ (LNO)…………….……..14

2.4 Structure and physical properties of $SrTiO_3$ (STO)…………………16

Chapter 3 Experiments………………………………………….…..…………18

3.1 Deposition systems……………………………...…………………18

3.1.1 High-vacuum RF Magnetron Sputtering System (HV RF-sputtering)…………………………………………………………18

3.1.2 Ultrahigh-vacuum RF- Magnetron Sputtering System (UHV RF-sputtering)…………………………………………………..…..20

3.1.3 Atomic Layer Deposition (ALD)……………………………………23

3.2 Characterization of structure…………………………………………26

3.2.1 X-ray Diffraction and X-ray Reflectivity (XRD & XRR)…………26

Contents (continued)

3.2.2 Synchrotron Radiation X-ray Scattering (SRXRS)………………..28

3.2.3 Atomic Force Microscope (AFM)...…….……………………………34

3.2.4 High Resolution Transmission Electron Microscope (HRTEM)….36

3.3 Characterization of properties…………………………...………37

3.3.1 Diffraction Anomalous Fine Structure (DAFS)..…………………37

3.3.2 Time-of-Flight Secondary-ion Mass Spectrometer (TOF-SIMS)…38

3.3.3 X-ray Photoelectron Spectra (XPS)………………………………39

3.3.4 Ferroelectric Test System (FTS)…………………………………40

3.3.5 Positive up and negative down (PUND)…………………………43

Chapter 4 Results and Discussion…..……………………………………44

4.1 Structure and physical properties of the single-layer BFO thin film..44

4.1.1 Crystal structure of the BFO thin film………………..…………44

4.1.2 Electrical properties of the BFO thin film……..…………...……53

4.2 Epitaxial growth and effect of strain on the BFO/LNO superlattice..56

4.2.1 Structure of the BFO/LNO superlattice……………..……………56

4.2.2 Electrical properties of BFO/LNO superlattice…………………......75

4.3 Sublayer thickness and leakage effect of the BFO/LNO superlattice…………………………………………………….……..78

4.3.1 Crystal structure of the BFO/LNO superlattice with varied sublayer thickness……………………..……………………………78

4.3.2 Electrical properties of the BFO/LNO superlattice with various sublayer thicknesses..……………….…………………………85

4.4 Growth of ultra-thin undoubted BFO films by atomic layer deposition…..…………………………………………………..91

4.4.1 Crystal structure and composition of ultra-thin BFO films………91

Contents (continued)

4.4.2 Leakage property of the ultra-thin BFO films……………….........99

4.4.3 Cross-sectional image and surface morphology of ultra-thin BFO films……………………………………………………...……101

4.4.4 Ferroelectric property of ultra-thin BFO films……………..……..105

Chapter 5 Conclusions……………………………………………….…….111

References……………………………….……………………………114

Table Captions

Table 3.1 The growth conditions of BFO/LNO superlattice : deposition temperature and sublayer thickness..…………………………...21

Table 4.1.1 Parameters from best-fitted results of reflectivity curves of BFO films deposited on the LNO-coated Si substrate at various temperatures..…………………..…………………..……….50

Table 4.2.1 Parameters obtained from best-fit results of reflectivity curves of BFO/LNO superlattice films deposited on the Nb-doped STO substrate with varied deposition temperature……………......……72

Table 4.3.1 Thickness parameters of the BFO/LNO superlattice obtained from the results of X-ray diffraction, X-ray reflectivity and SIMS…….80

Table 4.4.1 Parameters obtained from best-fit results of XPS spectra of BFO thin films deposited on the LNO-coated Si substrate by (a) ALD and (b) RF-sputtering…………………..……………………..…..…98

Figure Captions

Figure 2.1 Illustration of the changes in a ferroelectric material which transforms from a paraelectric cubic into ferroelectric tetragonal phase with temperature……………………………………………………………8

Figure 2.2 Ferroelectric (P –E) hysteresis loop. Circles with arrows represent the polarization states……………………..…………………………....10

Figure 2.3 Crystal structures of $BiFeO_3$; (A) tetragonal (B) unit cells………...11

Figure 2.4 (a) Crystallographic and (b)magnetic structure of BFO…………...12

Figure 2.5 Polarization of $BiFeO_3$: bulk single crystal (top) and epitaxial thin film (bottom)……………………………………………………………13

Figure 2.6 Structure of LNO crystal…………………………………………....15

Figure 2.7 Structure of STO crystal……………………………………………17

Figure 3.1 High vacuum RF-sputtering……………………………...…………19

Figure 3.2 BFO/LNO superlattices…………………………………...………...22

Figure 3.3 Ultra high vacuum RF-sputtering…………………………..……22

Figure 3.4 ALD deposition process of BFO thin film for one cycle…………..24

Figure 3.5 Time table of modified ALD process for BFO thin film growth…...25

Figure 3.6 X-ray diffraction and X-ray reflectivity……………………………..27

Figure 3.7 Synchrotron Radiation……………………………………………...29

Figure 3.8 Taiwan Light Source (TLS at NSRRC)…………………………....30

Figure 3.9 Insertion device………………………………………………...……..33

Figure 3.10 NSRRC BL17b1 eight circle diffractometer……………………...33

Figure 3.11 Sketch diagram of AFM apparatus…………………………….…35

Figure 3.12 TEM……………………………………………………………..…...36

Figure 3.13 Schematic diagram of TF Analyzer 2000…………………………41

Figure 3.14 Excitation signal for a triangular voltage hysteresis measurement..41

Figure 3.15 Waveform of the leakage current measurement………………..…42

Figure 3.16 Typical excitation of PUND measurement……..……….……….43

Figure 4.1.1 XRD **"θ–2θ"** scan of BFO films deposited on a LNO-coated Si substrate at various temperatures. The inset shows the width of the BFO (002) rocking curve (**ω** scan)……………………………...45

Figure 4.1.2 In-plane grazing-incidence XRD pattern of BFO films deposited on a Si substrate at various temperatures……………………………46

Figure 4.1.3 X-ray reflectivity curve (open circle) of BFO films deposited on a Si substrate at various temperatures and their best-fitted data (solid line) as a function of momentum transfer. The inset shows an expanded view of the best-fitted curve (solid line) and experimental data (open circles) of a BFO film deposited at 500 °C……………..………………...…………………………………..48

Figure 4.1.4 AFM images of single-layer BFO deposited on the LNO coated si substrate at substrate temperatures/°C: (a) 300, (b) 400, (c) 500 and (d) 600……………………………………………………49

Figure 4.1.5 Rocking-curve measurement of the BFO film deposited at 500 °C. The arrows indicate two diffuse scattering peaks on the shoulder. The inset shows a comparison of intensity curves between specular and diffuse X-ray scattering...52

Figure 4.1.6 P–E hysteresis loops of BFO films (thickness 60 nm) deposited on the LNO-coated Si substrate at various temperatures…...….......54

Figure 4.1.7 J-E curve of single-layer BFO thin films deposited at 300 – 700

°C…………………………………………………………...…....55

Figure 4.2.1 Intensity distribution of the (002) radial scan of the BFO/LNO superlattice film deposited at various substrate temperatures. The inset shows an expanded view of the superlattice film deposited at 660 °C……………………………….……………..………..…...57

Figure 4.2.2 X-ray intensity of the radial scans along the (200) in-plane Bragg peak of BFO/LNO superlattice films deposited at various substrate temperatures. An arrow marks the position of the superlattice main peak……………………………………………………......……58

Figure 4.2.3 Azimuthally scan (Φ scan) of the surface peak and the substrate Bragg peak for a superlattice film deposited at 660 °C……...…..60

Figure 4.2.4 Intensity distribution of the (111) radial scan of the BFO/LNO superlattice film deposited at 660 °C……………..……....……60

Figure 4.2.5 HRTEM cross-sectional images of the BFO/LNO superlattice on the (001) $SrTiO_3$ substrate deposited at 660 °C; (a) large scale image, and (b) image of the interface regions between individual layers and between film and substrate……………....……...61,62

Figure 4.2.6 DAFS result of the (002) superlattice diffraction peak and the extra peak as shown in figure 4.2.1 (marked *) for film deposited at 710 °C (a) Ni K-edge, and (b) La L1-edge…………………...………64

Figure 4.2.7 In-plane compressive strain and out-of plane tensile strain of the BFO layer as a function of deposition temperature…………....….67

Figure 4.2.8 Rocking curves of the in-plane (200) main peak of BFO/LNO superlattice films deposited at various temperatures...……...…..68

Figure 4.2.9 Reflectivity curves of BFO/LNO superlattice films deposited at various substrate temperatures and their best-fit results (solid line)

as a function of momentum transfer……………………………70

Figure 4.2.10 AFM images of BFO/LNO superlattice films deposited at substrate temperatures/°C: (a) 560, (b) 610, (c) 660, (d) 710, (e) 760, and (f) 810……………………………...……..…...74

Figure 4.2.11 P-E hysteresis loops of BFO/LNO superlattice deposited at various substrate temperature………..……..…………...….76

Figure 4.2.12 J-E curve of BFO/LNO superlattice films deposited at 560 – 710 °C……………………..……………………………………...77

Figure 4.3.1 Intensity distribution of the (002) radial scan for the BFO/LNO superlattice with varied thickness of sublayer and periods. The inset shows the best fits (solid line) for the experimental XRD patterns for BFO/LNO superlattices at thicknesses 3.6 and 8.5 nm………..…………..…………………..…………………..79

Figure 4.3.2 SIMS depth profile of the $(BFO_{8.5}/LNO_{8.5})_6$ superlattice film…....81

Figure 4.3.3 X-ray intensity of a set of radial scans along the (200) in-plane Bragg line of BFO/LNO superlattice films deposited for varied periods. An arrow marks the position of the superlattice main peak. The inset shows an azimuthal scan (Φ scan) of the surface peak and the substrate Bragg peak for a $(BFO_{1.7}/LNO_{1.7})_{30}$ superlattice film…………………………………………………………...83

Figure 4.3.4 Strain dependent and J–E curve of BFO/LNO superlattice films with varied sublayer thickness (a) in-plane strain and out-of-plan strain, and (b) the **J–E** curve……………….……………………86

Figure 4.3.5 P–E hysteresis loops of a BFO/LNO superlattice at thicknesses 1.7, 3.6 and 8.5 nm of sublayers and single-layer BFO thin film (thickness 60 nm)…………………..…………………….…..88

Figure 4.3.6 Polarization measurements for all sublayer thicknesses and a single-layer BFO (a) polarization value (2**Pr**) at varied frequencies from **P–E** hysteresis loops, and (b) the remanent polarization obtained from the PUPD test…………………………………...………90
Figure 4.4.1 ALD growth rate as a function of substrate temperature for BFO thin films deposited on the LNO-coated Si substrate……………92
Figure 4.4.2 Surface normal radial XRD spectra of BFO thin film deposited at various substrate temperatures……………………….……………94
Figure 4.4.3 DAFS results of BFO thin film deposited at 500 °C (a) Fe^{3+} K-edge, and (b) Bi^{3+} L_3-edge……………………..…..…..………………96
Figure 4.4.4 XPS spectra of BFO thin film by (a)-(c) ALD (d)-(f) RF-sputtering……………………………………………..………..98
Figure 4.4.5 J-E curves of the BFO thin films with different substrate temperatures…………………………………………………..…100
Figure 4.4.6 Cross-section view of HRTEM for BFO thin films grown on LNO buffer layer by (a) ALD (b) RF-sputtering……………………..102
Figure 4.4.7 AFM images of BFO thin films grown by (a) ALD and (b) RF-sputtering…………………….……………………….……….104
Figure 4.4.8 P-E hysteresis loops of BFO thin film deposited in the range of substrate temperature 480-550 °C…...…………...……………106
Figure 4.4.9 The relationship among crystal structure, leakage current, and polarization at various deposition temperatures of ALD……...107
Figure 4.4.10 Normalized polarization as a function of film thickness grown by RF-sputtering, PLD, CVD, Sol-gel, and ALD this work………110

Chapter 1

Introduction

Multiferroic materials with a structure of perovskite type, in which ferroelectric and magnetism coexist, have attracted much attention, due to the physical properties that they offer prospective applications in devices taking advantage of two coupled parameters based on a local lattice distortion and electron spin [1-4]. Multiferroic oxide thin films are hence intensively investigated because of their scientific importance and technological promise for applications as non-volatile memories, such as ferroelectric random-access memories (FRAM), magneto-resistive random-access memories (MRAM) etc [4-8]. Among various multiferroic oxide materials, BFO has attracted much attention because of its high Curie temperature, T_C = 1043 K, and high Néel temperature, T_N = ~647 K [9,10]. BFO possesses a large polarization and a low crystallization temperature; both properties are desirable for highly dense FRAM. A randomly oriented ferroelectric capacitor tends to increase the variation of polarization bit to bit. As the material is free of lead, it becomes a worthy candidate for practical industrial applications. Ferroelectric thin films promise diverse applications in microelectronics and data-storage devices, such as sensors, transistors, and nonvolatile memories [11]. Considerable efforts have been focused on the deposition of BFO thin films with the most desirable film texture and electrical behavior for several technologically demanding applications, including RF magnetron sputtering, pulse-laser deposition (PLD), sol–gel synthesis, and chemical vapor deposition (CVD) [4,12-14]. PLD has been used to grow epitaxial superlattice films of complicated oxide materials. An advantage of this method is easily to control stoichiometry and crystal

structure etc. For this reason epitaxial superlattice films of complicated oxides are typically prepared by PLD at high temperature [15,16]. RF magnetron sputtering is also an important method to grow epitaxial perovskite oxide thin-film materials because of the great reproducibility of the chemical composition and the facile control of the process [17-19]. RF magnetron sputtering has the advantages of large throughput at low cost and a large uniform region of deposition; both properties match well the requirements of industrial applications. A randomly oriented ferroelectric capacitor tends to increase the variation of polarization. To decrease this variation, epitaxial films might be the best option [20]. Epitaxial superlattice thin films have demonstrated perfect ferroelectric properties that have advantages in scaling for highly dense ferroelectric memory devices [17].

Integrated circuits (IC) constitute an application in which improved materials are critically required. FRAM are electroceramics at the current state of the art in commercial electro devices, but many other IC designs might benefit from electroceramics in the future. To fulfill the requirements of the semiconductor industry and to introduce the multiferroic material into this field for FRAM in a new generation [3], growing a thin layer onto a wafer scale and conformal coverage with decreasing leakage properties for devices are urgent need. The improved method to process thin films, such as ALD, is an application for this purpose.

In this dissertation, the first part describes the fundamental properties of BFO thin films; BFO thin films were deposited on a $LaNiO_3$-coated Si substrate with a RF magnetron sputtering system. X-ray reflectivity and diffraction were used to characterize the microstructure of the crystal quality, buried interface, and surface morphology of BFO thin films. We used LNO because it is a

metallic material that can serve both as the bottom electrode in fabricating integrated ferroelectric capacitors on Si and an effective interface for the growth of highly oriented ferroelectric thin films [21- 24].

The second part is to explore how the substrate-induced strain affects the ferroelectric behavior of ferroelectric thin films. Epitaxial strains can greatly enhance the ferroelectric polarization and the Curie temperature of thin films relative to their bulk counterparts [25]. We fabricated BFO/LNO superlattice films on Nb-doped $SrTiO_3$ (STO) substrate with an ultrahigh-vacuum RF magnetron sputtering system to improve the crystal quality and electrical properties; Nb-doped STO can serve as the bottom electrode. The crystalline phases, interfacial structure, and morphology of thin films are important because they have strong impacts on physical properties and applications. As there exists little information on the microstructure and morphology of the interfacial structure of multiferroic superlattice thin films, the investigation of superlattice structure on a microscopic scale becomes highly significant for applications involving the dense memory in multiferroic materials [26].

Whereas X-ray diffraction at grazing incidence is a valuable analytical tool to characterize epitaxial thin films, X-ray reflectivity has been demonstrated to be a powerful tool to determine the thin film structure of the interfaces and surface morphology layer by layer. We used LNO (lattice parameter 0.3861 nm of pseudocubic unit cell) because it has a crystallographic compatibility for the heteroepitaxial growth of a BFO (lattice parameter 0.3962 nm of rhombohedral unit cell) layer; a lattice parameter smaller than that of BFO introduces a strain through a lattice mismatch at the interface [27-30]. In this superlattice system, the ferroelectric properties of the superlattice films result mainly from the ferroelectric layers, i.e., BFO, because of the conductive property of the LNO

material. For a ferroelectric and conductive superlattice thin film, those materials can therefore serve for an investigation of the strain dependence of ferroelectric properties of BFO layers in superlattice structures.

In the final part, the leakage current is a major problem in BFO thin films; to improve the leakage issue of the BFO thin films, ALD was first introduced to grow of BFO thin films. ALD is a self-limiting process to grow thin films that possess several practical advantages including accurate and simple control of the film thickness, larger grown area and larger batch capability, effective conformality, and reproducibility [31]. The convectional ALD process is highly suitable for the growth of binary compounds; only a few reports were published about ternary compounds with ALD [32-34], among which BFO is absent. The most straightforward approach for ALD of multicomponent oxides is to use separate binary cycles of deposition and to adjust the composition with a variation of the cycle ratio [35]. All cation precursors must be compatible, i.e. volatile, thermally stable and reactive at the same process temperature. These requirements yield a fairly narrow window of the process, which is just below the decomposition temperature of the least stable precursor. The bilayer structure of two binary compounds that are not true ternary compounds is due to poor valence binding between two cation atoms when the bilayer ratio is large [35]. For the purpose of preparing the ternary BFO, we implemented an ultra-rapid ALD diaphragm valve installed between the reactor and the vacuum pump in a novel ALD process, with interruption of the flow rate. To retain a precursor in the reactor chamber, the valve was closed first for a small interval before a precursor was introduced into the reactor [36]. The main influences of this step are to enhance the precursor density in the reactor and to extend the duration of the reaction at the sample surface, which provides a satisfactory condition to

grow thin films.

In this work, we report for the first time the highly (001)-oriented BFO thin films grown with the ALD on a Si (100) substrate with LNO buffer layer and the deposition temperatures are in a range of 480 - 550 ^{o}C, which shows satisfactory results for the crystal structures and ferroelectric properties.

Chapter 2

Literature review

2.1 Multiferroic material

Multiferroics or magnetoelectrics, have more than two switchable states such as polarization, magnetization and strain [37,38]. Multiferroics show multifunctional materials of an appealing class that exhibit several ferroic orders as ferroelectricity and antiferromagnetism at the same time [3]. The coexistence of several order parameters drives new physical phenomena and provide possibilities for novel device functions [39].

A multiferroic that is ferromagnetic and ferroelectric has demonstrated large linear magnetoelectric effects. As a result of the ferroelectric and ferromagnetic materials that typically possess large permittivity and permeability respectively, α_{ij} is bounded by the geometric mean of the diagonalized tensors ε_{ii} and μ_{jj} such that:

$$\alpha_{ij}^2 \leq \varepsilon_0 \mu_0 \varepsilon_{ii} \mu_{jj}$$ [40]

Both magnetization and polarization are indicated to encode information independently in a single multiferroic. A four-state memory has been demonstrated [41], but in reality it is agreed that the two order parameters are coupled [42,43]. Coupling could in theory allow data to be written electrically and read magnetically. It would take advantage of the best field of FRAM and magnetic data storage; this condition is attractive [3].

2.1.1 Ferroelectric properties

Ferroelectrics are polar materials that are provided with two equilibrium orientations of the spontaneous polarization vector in the absence of an external electric field, and in which the spontaneous polarization vector can be switched

between those orientations with an electric field [44-46]. Most ferroelectric materials experience a phase transition of crystal structure from a high-temperature nonferroelectric phase into a low-temperature ferroelectric phase (Fgure 2.1). The paraelectric phase might be piezoelectric or non-piezoelectric and is rarely polar [44]. The symmetry of the ferroelectric phase is invariably less than the symmetry of the paraelectric phase. The temperature of the phase transition is called the Curie point (T_C). Above the Curie point the dielectric permittivity decreases with increasing temperature according to the Curie–Weiss law

$$\varepsilon = \varepsilon_0 + \frac{C}{T - T_0} \approx \frac{C}{T - T_0}$$

in which C is the Curie constant and T_0 ($T_0 \leqq T_C$) is the Curie–Weiss temperature.

Only a transition temperature into the first ferroelectric phase is called the Curie point. The transition into a ferroelectric phase generally leads to strong anomalies in the dielectric, elastic, thermal, and other properties [44], and is accompanied with changes in the dimensions of the unit cell [47].

Ferroelectric, dielectric and piezoelectric properties

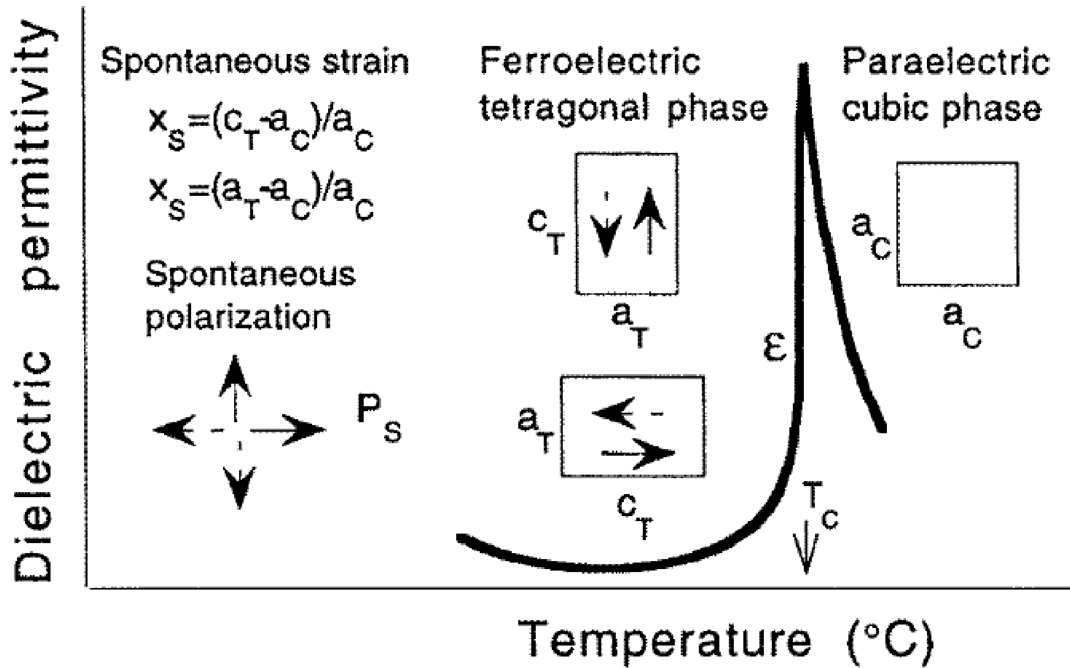

Figure 2.1 Illustration of the changes in a ferroelectric material which transforms from a paraelectric cubic into ferroelectric tetragonal phase with temperature. The arrows show possible directions of the spontaneous polarizations (in two dimensions). The unit cells are represented by a square for the cubic phase and rectangle for the tetragonal phase [47].

2.1.2 Ferroelectric hysteresis loop and polarization switching

The most important characteristic of ferroelectric materials is the polarization switching with an electric field. One outcome of the domain-wall switching in ferroelectric materials is the occurrence of a ferroelectric hysteresis loop (Figure 2.2) [47]. This hysteresis loop can be observed experimentally with a Sawyer - Tower circuit [48]. With small values of an AC electric field, the polarization increases linearly with the field amplitude, according to relation

$$P_i = \chi_{ij} E_j$$

This condition corresponds to segment AB in Figure 2.2. In this area, the field is insufficiently strong to switch domains with the unfavorable direction of polarization. With increasing field, the polarization of domains with an unfavorable direction of polarization begins to switch in the direction of the field; the measured charge density (segment BC) increases rapidly. The polarization response in this region is strongly nonlinear and the equation is no longer effective. In case all domains are aligned (point C), the ferroelectricity again becomes linear (segment CD). If the field intensity begins to decrease, some domains switch back, but at zero field the polarization is nonzero (point E). To measure a zero polarization state, the field must be reversed (point F). Further increased field in the negative direction causes a new alignment of dipoles and saturation (point G). The field strength is then decreased to zero and reversed to complete the cycle. The value of polarization at zero field (point E) is called the remanent polarization (P_r). The field required to cause the polarization to zero is called the coercive field (E_C) [47].

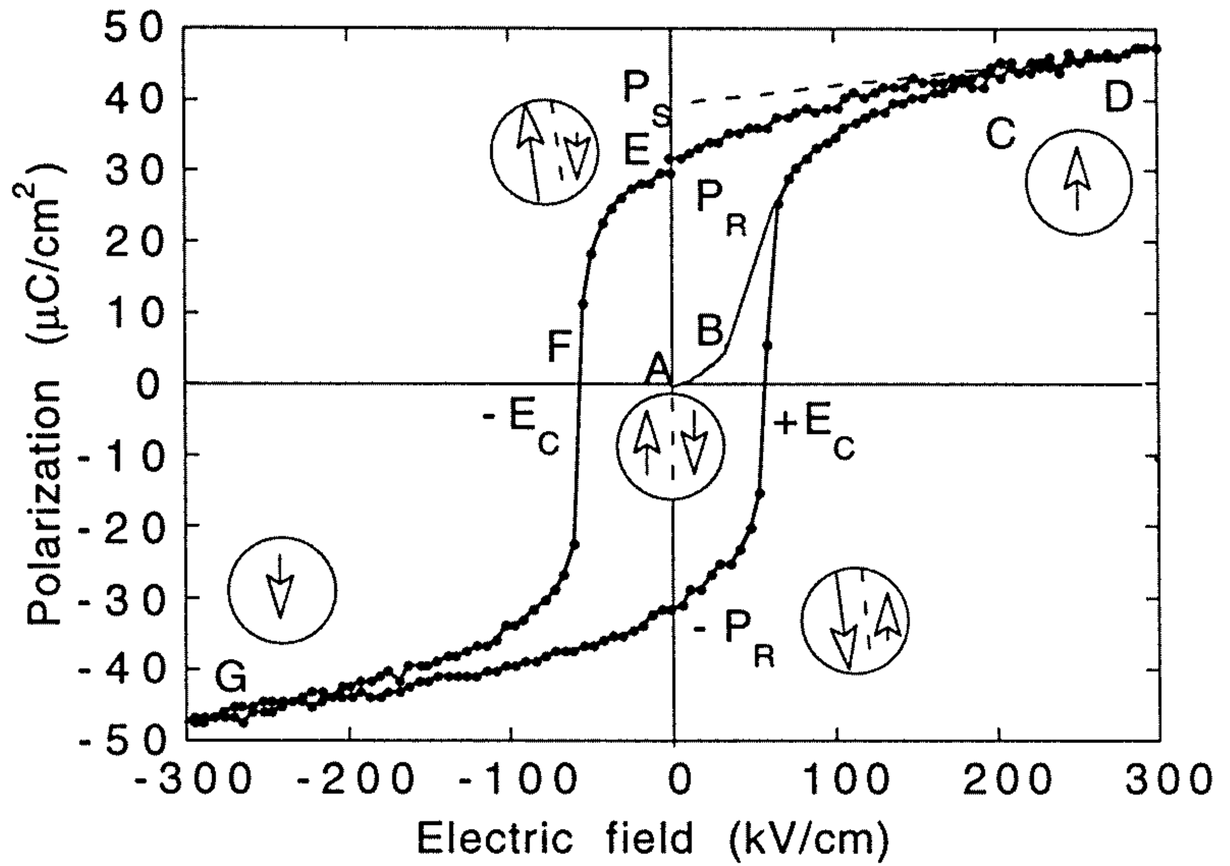

Figure 2.2 Ferroelectric (P –E) hysteresis loop. Circles with arrows represent the polarization states [47].

2.2 Structure and physical properties of $BiFeO_3$ (BFO)

2.2.1 Crystal structure of BFO

The phase of BFO at 300 K is classified as rhombohedral (point group R3c) [49]. The unit cell of perovskite type has lattice parameter 0.3965 nm and rhombohedral angle of 89.3 – 89.48^o [50,51], with ferroelectric polarization along $[111]_{pseudocubic}$ [51]. The unit cell is also describable in a hexagonal frame of reference, with the hexagonal *c*-axis parallel to the diagonals of the perovskite cube, i.e., $[001]_{hexagonal}$ || $[111]_{pseudocubic}$. In some cases, a pseudocubic representation has been used, in which $[111]_c$ is equivalent to $[001]_{hex}$. Oxygen atoms occupy face-centered sites of the Bi cubic framework. The coefficient of thermal expansion is neither completely linear nor isotropic [52-54], and accounts of values [52,53] vary notably, ranging from 6.5×10^{-6} to 13×10^{-6} K^{-1}. BFO is a material with a high ferroelectric Curie (T_C=1083 K) [55] and antiferromagnetic Neel (T_N=643 K) [56] temperatures.

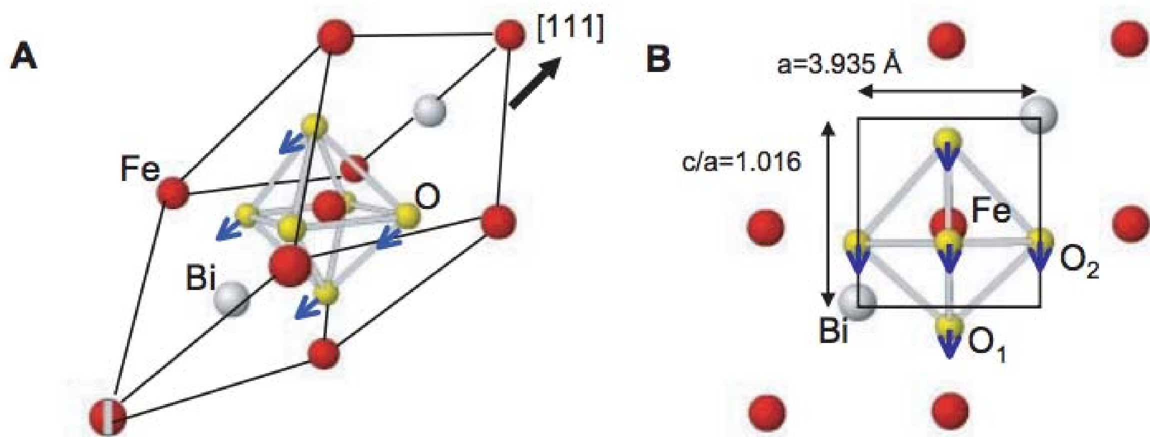

Figure 2.3 Crystal structures of $BiFeO_3$;(A) tetragonal (B) unit cells [2].

2.2.2 Physical properties of BFO

BFO has been reported to be ferroelectric with its polarization oriented along the rhombohedral *c*-axis $[111]_c$ due to the displacement of Bi, and Fe, O relative to each other [57] shown in Figure 2.4(a); neutron diffraction experiments revealed antiferromagnetic ordering along $[111]_c$ [58]. Spins in neighboring positions are antiparallel with each other, producing a G-type antiferromagnetic ordering, as presented in Figure 2.4(b).

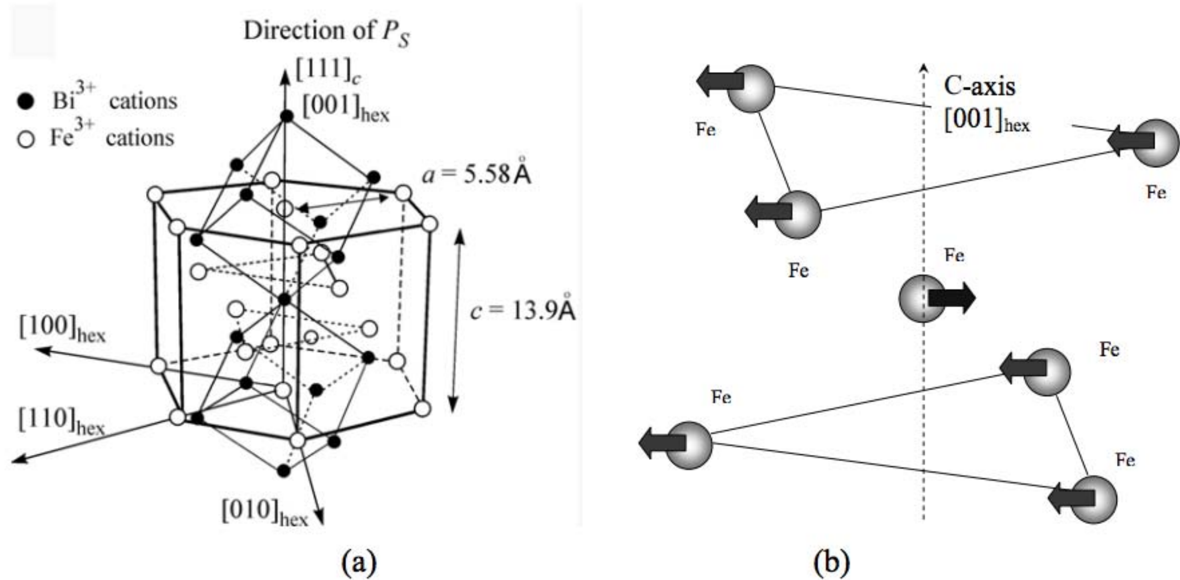

Figure 2.4 (a) Crystallographic and (b) magnetic structure of BFO [59].

The early measurements of bulk ferroelectric materials in the 1960s and 1970s yielded only small values of the polarization, but the small value of $P_r = 6$ $\mu C\ cm^{-2}$ reported by Teague et al [55]. for single crystals was viewed by those authors as limited without saturation. The greatest polarization of the thin films was initially thought [2] to be resulted from strain enhancement; great single crystals were grown finally [60-64], with P_r values near those of the films about 60 $\mu C\ cm^{-2}$ normal to (001) orientation (Figure 2.25) and, therefore, near 100 μC cm^{-2} along $[111]_{pseudocubic}$; a large polarization property was also discovered in

ceramics [65]. Calculations of electronic structure agree with the statement that the polarization of bulk BFO is intrinsically large [66,67] (90–100 μC cm^{-2}) and insensitive to strain [67].

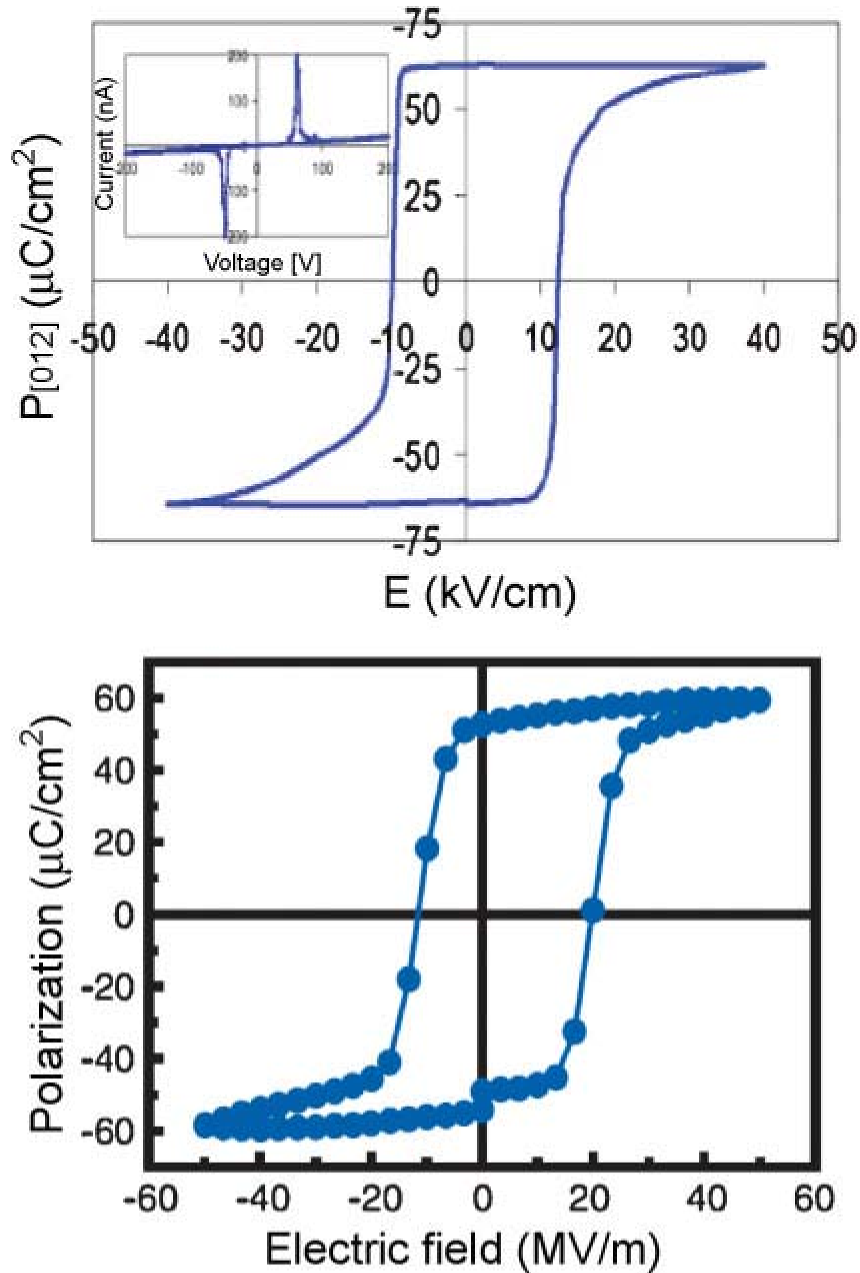

Figure 2.5 Polarization of $BiFeO_3$: bulk single crystal (top) [60] and epitaxial thin film (bottom) [2].

2.3 Structure and physical properties of $LaNiO_3$ (LNO)

Among perovskite oxide materials of many kinds, LNO is an uncommon instance exhibiting paramagnetic metallic behavior. The interest in this material has led to the development of extremely conductive electrodes for ferroelectric thin-film devices, including nonvolatile memories for technological applications [68]. Superior heteroepitaxy with doped lanthanum manganites [69] means that LNO thin films can also serve as electrodes in magnetoelectronic devices in view of highly spin-polarized compounds [70,71].

LNO is a perovskite material with a distorted rhombohedral structure of rhombohedral angle of 60.41° and lattice parameter a=0.5461 nm. A pseudocubic lattice parameter of LNO is 0.383 nm is shown in Figure 2.6. LNO is n-type metallic oxide without doping. The oxide is characterized by a small electron density at E_F like the new series of high T_c copper oxides [72]. The resistivity at 300 K is about 1 mΩ · cm. The LNO single crystal can serve as a metallic bottom electrode, an ohmic contact material, a conservatory metallic layer, and a lattice-matched metallic-oxide material.

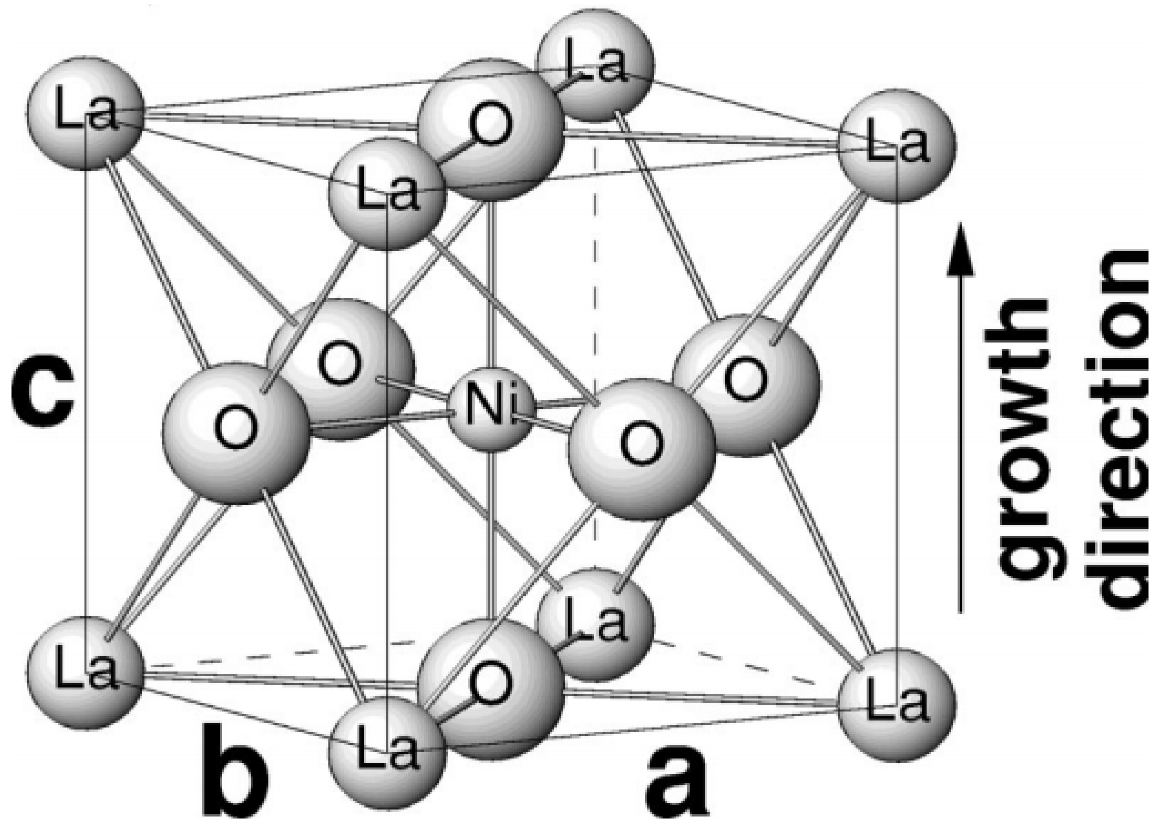

Figure 2.6 Structure of LNO crystal [73].

2.4 Structure and physical properties of $SrTiO_3$ (STO)

Strontium titanate ($SrTiO_3$) has been variously used as a substrate to grow oxide thin films of perovskite type, because STO is chemically and compositionally stable, and has a small lattice mismatch with many perovskite-oxide materials [74-76]. The electrical conductivity of STO is readily controlled from a *n*-type semiconductor to metal-like conduction (up to 10^{-4} Ω cm), and even to superconductivity at temperature T_C<0.3 K when Ti is partly substituted with Nb or La [78-81].

STO is a popular material of perovskite type with a cubic structure with lattice parameter of a=0.3905 nm. Because of its large relative permittivity and small dielectric loss, STO is applicable to electronic devices. The conductive Nb-doped STO substance with variable conductivity is not only used as a bottom electrode for the deposition of functional perovskite oxides [82-84] but also provides a possibility to fabricate fascinating and novel devices such as multilayer structure [85,86], superlattice [87], tunnel junctions [88], field-effect transistor [89], Schottky junction [90], and *p*-*n* junction [91,92].

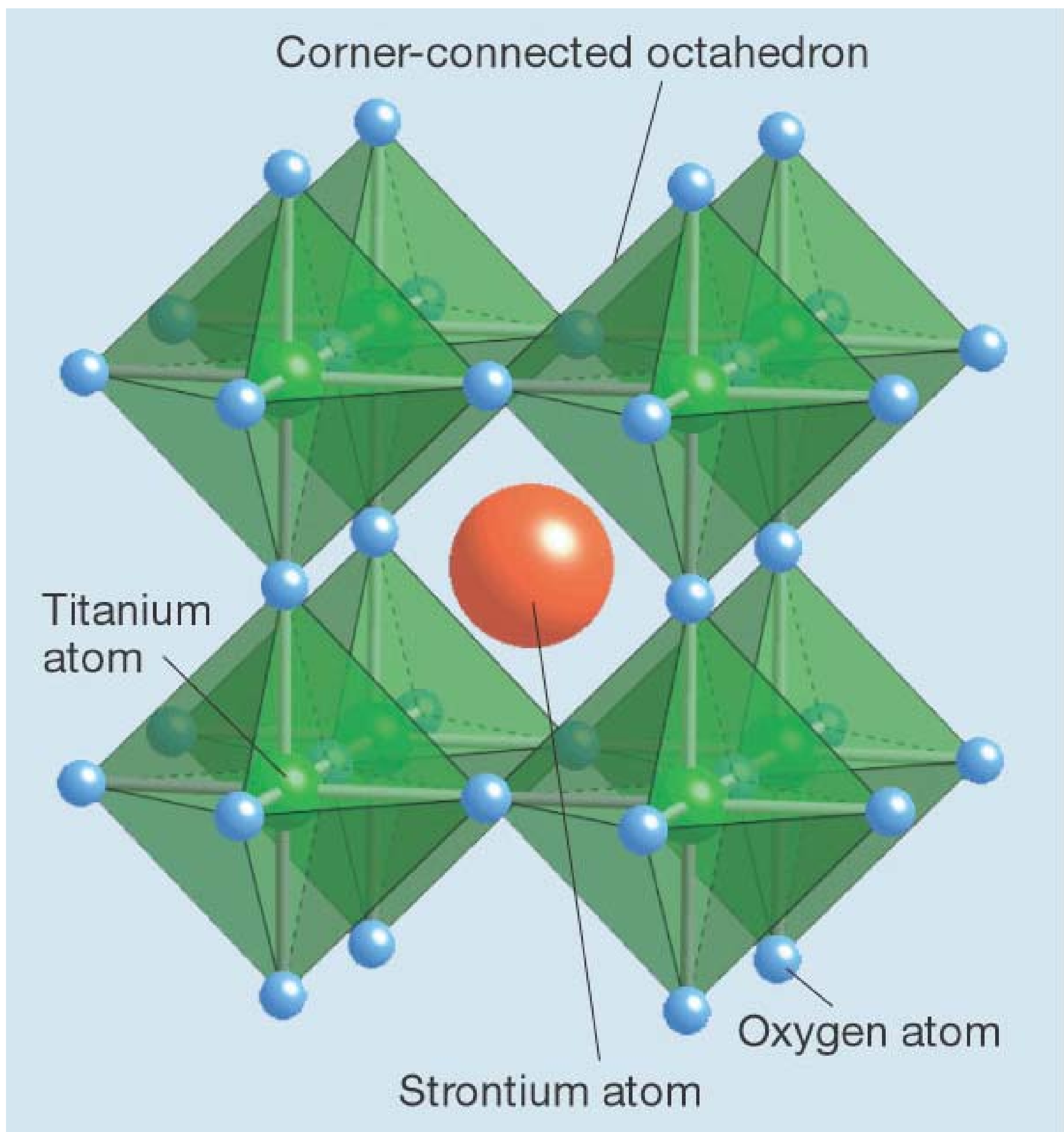

Figure 2.7 Structure of STO crystal [93].

Chapter 3

Experiments

3.1 Deposition systems

3.1.1 High-vacuum RF Magnetron Sputtering System (HV RF-sputtering)

The single-layer BFO thin film for study of the fundamental physical properties was deposited with a HV RF-sputtering system. The deposition chamber was connected to a pumping system consisting of a turbomolecular pump of speed 500 L/min; the base pressure was kept at 1×10^{-6} Torr to avoid contamination during deposition. The sputtering target of BFO was prepared through a conventional solid reaction on sintering a calcined mixed powder in a stoichiometric molar ratio Bi : Fe : O = 1.2 : 1 : 3; the excess bismuth compensated for Bi volatilization during deposition [94]; the LNO target with standard atomic ratio La : Ni : O = 1 : 1 : 3 was prepared on sintering calcined La_2O_3 and NiO powders (99.99 % purity) with standard atomic ratio La : Ni : O = 1 : 1 : 3 at 950 ^{o}C for 2 h. Highly pure working gas argon (99.9995 %) and reactive gas oxygen (99.9995 %) were controlled with mass-flow controllers (MFC) to maintain a stable flow rate with argon at 8 sccm and oxygen at 2 sccm. The MFC were precisely calibrated; the accuracy of the gas flow rate was within 2 %. The distance from the target to substrate was 140 mm; the working pressure was fixed at 1.5×10^{-2} Torr for growth of thin film. The sputtering was performed at power density of 1 W cm^{-2}; a LNO bottom electrode of thickness 50 nm was deposited on a (001) Si substrate at 500 ^{o}C. The BFO thin films were deposited on a LNO-coated Si substrate; the thickness of each sample was fixed at ~60 nm at a temperature in the range of 300-700 ^{o}C. With these parameters, the growth rate of deposited thin films of BFO is 1.37 nm/min.

The Si substrates were cleaned with supersonic rinsing with acetone and methanol for 10 min before deposition; the substrate was dried with nitrogen gas.

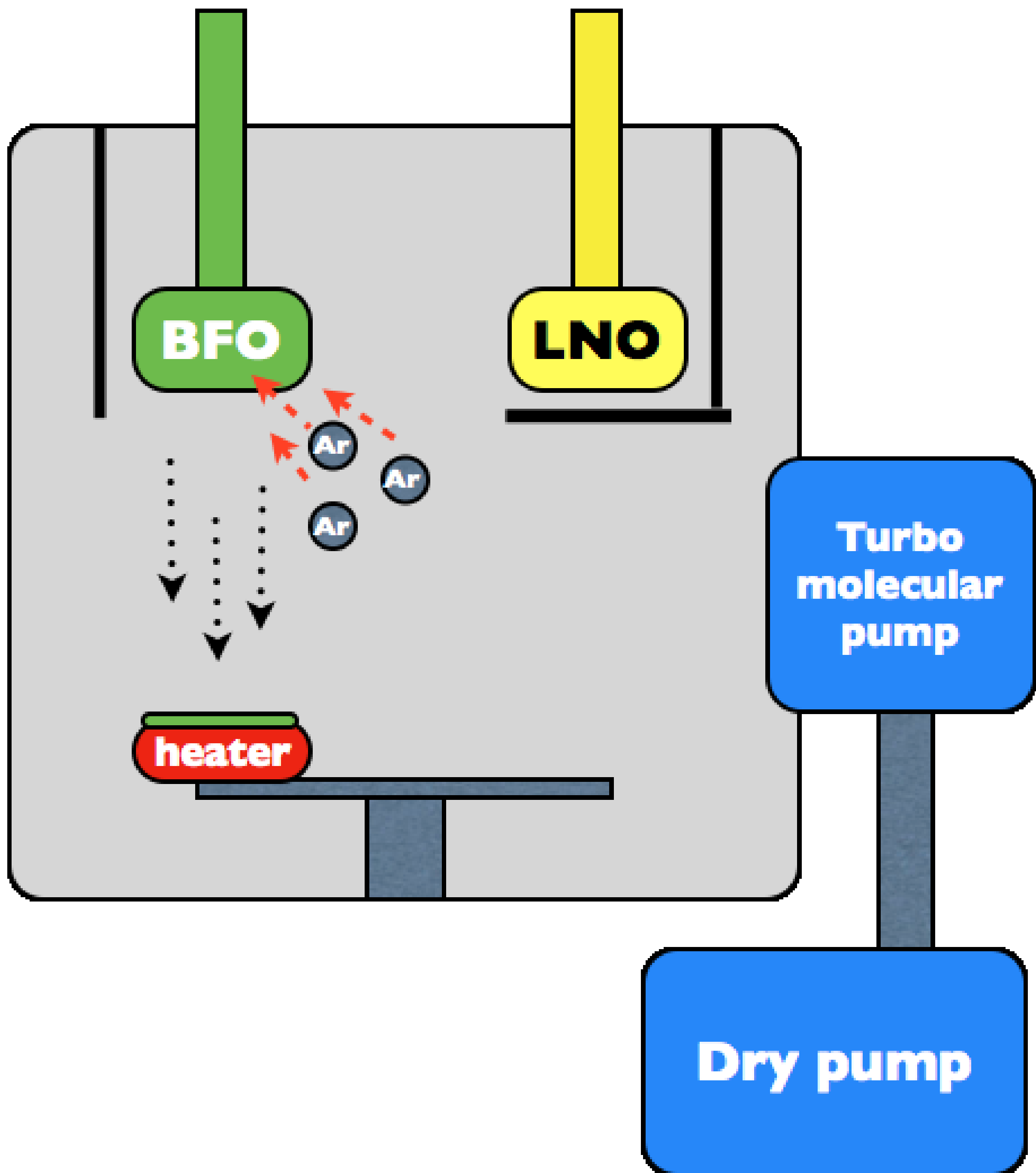

Figure 3.1 High vacuum RF-sputtering.

3.1.2 Ultrahigh-vacuum RF Magnetron Sputtering System (UHV RF- sputtering)

To grow a superlattice thin film of high quality, the UHV RF-sputtering system with a double gun was employed in this experiment. The vacuum chamber was connected to a pumping system comprising three turbomolecular pumps, two for the main chamber and one for the preparation chamber. The sample was transferred into the main chamber from the preparation chamber with a load lock; the shutter opening was controlled with a computer. We thereby controlled precisely the duration of deposition of each layer during the deposition of a superlattice thin film. The base pressure of the main chamber was kept at 3×10^{-8} Torr to avoid contamination at all times. The same sputtering target of BFO and LNO was used with the HV RF-sputtering. Highly pure working gas argon (99.9995 %) and reactive gas oxygen (99.9995 %) were also used and controlled with the MFC to maintain a stable flow rate with Ar at 8 sccm and O_2 at 2 sccm. The distance from the target to the substrate is 90 mm; the working pressure is fixed at 1.5×10^{-2} Torr. The RF sputtering was performed at power density 0.74 W cm^{-2} (BFO) and 0.98 W cm^{-2} (LNO) without a bias voltage. The growth rate of thin films are 0.6 nm/min for BFO and 0.4 nm/ min for LNO; a shutter interrupts the deposition for 12 s between growths of consecutive sublayers. To design and optimize the growth condition of both the BFO/LNO superlattice and the thin-film structure for the electrical properties, we designed the superlattice to contain 30 periods of symmetric BFO/LNO with each sublayer of thickness 1.7 nm; the deposition temperature of the superlattice was set at 560, 610, 660, 710, 760 and 810 ^{o}C for the desired properties. Based on an optimum growth condition of the superlattice, a symmetric sublayer structure $(BFO_m/LNO_m)_n$, in which *m* is the thickness/nm of sublayer and *n* is the number of repeating periods, was adopted to investigate the strain effect on the

ferroelectric properties. The superlattice structure contained BFO/LNO sublayers in 6-30 periods with a sublayer thickness in the range 1.7-8.5 nm at deposition temperature 660 ^{o}C. The total thickness of films was fixed at ~100 nm.

The STO substrate was cleaned with supersonic rinsing with acetone and methanol for 10 min, and subsequently heated at 710 ^{o}C for 10 min in a dioxygen atmosphere at 4×10^{-2} Torr to clean the sample surface.

Table 3.1 The growth conditions of BFO/LNO superlattice : deposition temperature and sublayer thickness.

nm / oC	1.7	2.6	3.6	5.2	8.5
560	◎	--	--	--	--
610	◎	--	--	--	--
660	◎	◎	◎	◎	◎
710	◎	--	--	--	--
760	◎	--	--	--	--
810	◎	--	--	--	--

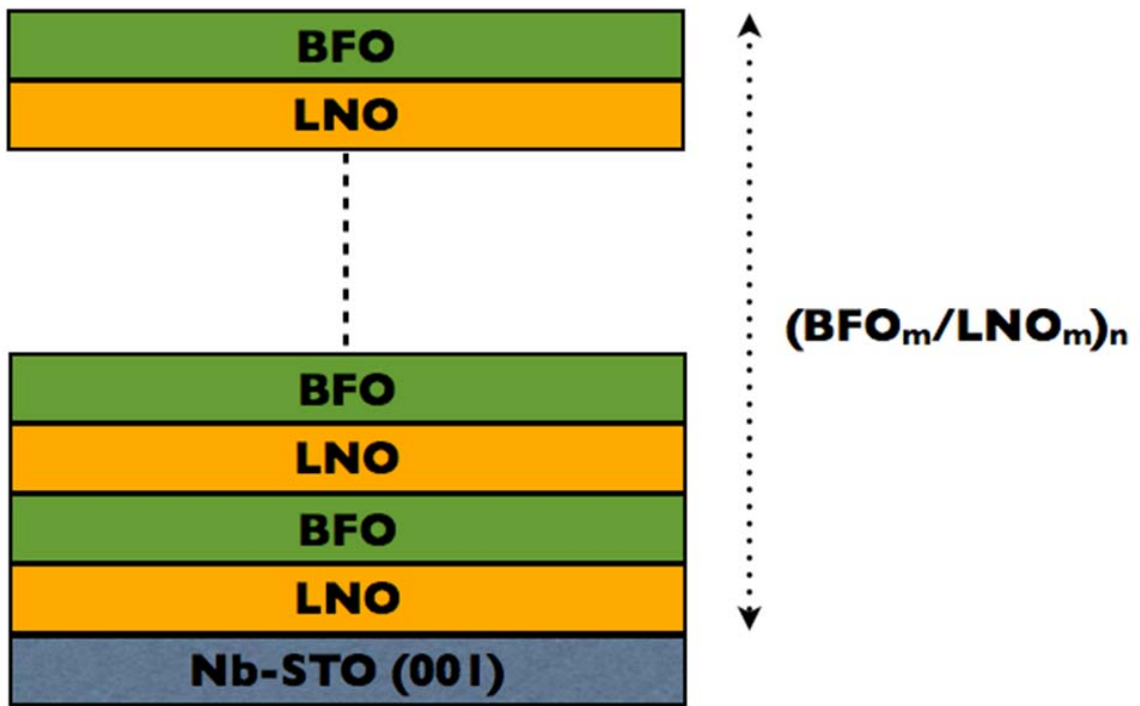

Figure 3.2 BFO/LNO superlattices.

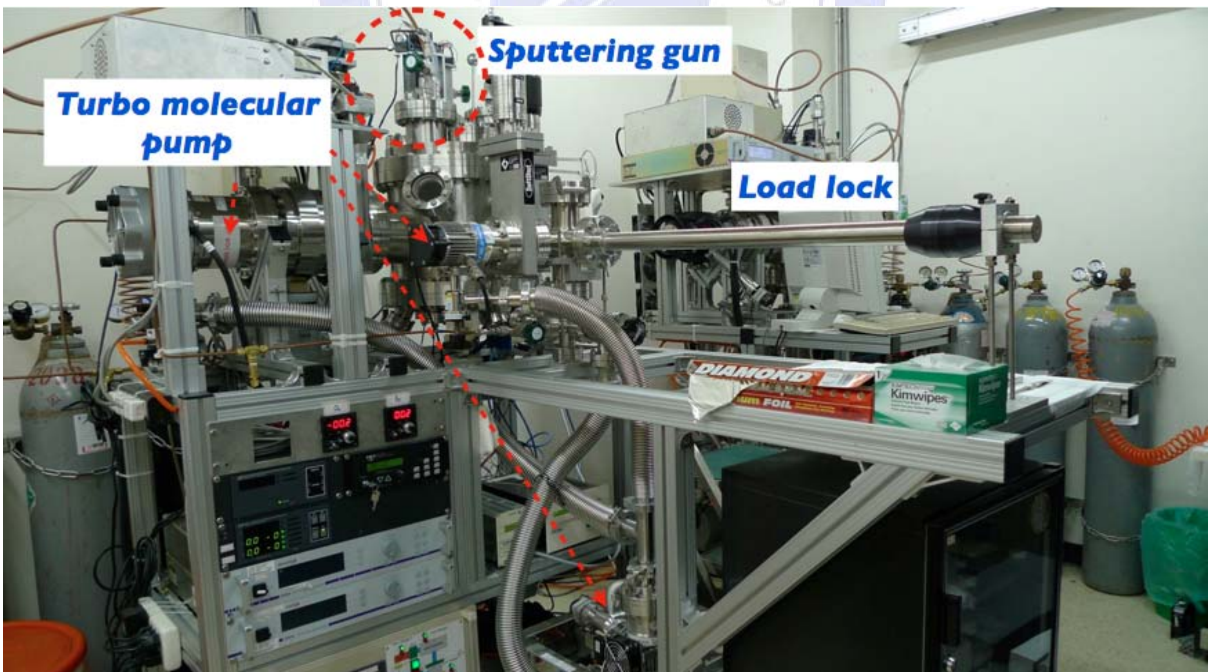

Figure 3.3 Ultrahigh vacuum RF-sputtering.

3.1.3 Atomic Layer Deposition (ALD)

ALD is a self-limiting process to grow thin films that possess several practical advantages including accurate and simple control of thickness, large area, large batch capability, effective conformality, reproducibility, straightforward doping, scaling, ability to produce sharp, and tailored interfaces to prepare multilayer structures.[31]

ALD involves a self-limiting vapor-phase chemisorption that relies on consecutive surface reactions and utilizes critical purging steps to prevent interactions between reactive precursors.[95] The BFO thin films were grown on the LNO-coated Si (001) substrate with ALD; trimethylbismuth [$(CH_3)_3Bi$, purity 95 % min, Nanjing Chemlin Chemical Industry Co., Ltd], cyclohexadieneiron tricarbonyl [$C_6H_8Fe(CO)_3$; purity 97 % min, Alfa Aesar], and deionized water (H_2O) served as precursors for atoms of Bi, Fe and O, respectively. Thin films of BFO were deposited to a desired thickness ~10nm in a range of 480 - 550 ^{o}C. A LNO buffer layer of thickness 50-70 nm was deposited on a Si(001) substrate at 500 ^{o}C with a RF-sputtering system, which provided a satisfactory condition for the growth of BFO.[96] Herein, a unique ALD process was adopted to grow the BFO thin film that differed from the conventional ALD process; the precursors were O, Fe, and Bi to form 1 ALD cycle. The duration of pulses for O, Fe, and Bi were 100，400 and 15 ms, respectively. Between a precursor pulse for evacuation of the chamber, the interval in which the ALD valve was closed to ensure that the precursor maintained a constant vapor pressure in the chamber so as to increase the reaction duration, we called the *stock time* [31,36], 2 s for O, 4 s for Fe, and 0.5 s for Bi. After the stock time, highly pure gaseous N_2 (99.9995%) was employed

to purge the chamber for 5 s at 1.1 torr before being evacuated with a rotary pump for 7 s to base pressure $3x10^{-2}$ Torr before the next precursor was admitted to the chamber, as shown in Figure 3.5. Purging and pumping were performed in the same manner as with the conventional ALD method. An enhanced affinity with a ferroelectric oxide had advantages for the interfacial properties between the conductive and ferroelectric oxides because of their similar structures of perovskite type provided by conductive oxides; the lattice parameter of LNO was a = 0.386 nm with a similar perovskite structure, which is compatible with the lattice parameter of BFO, a=0.396 nm [97].

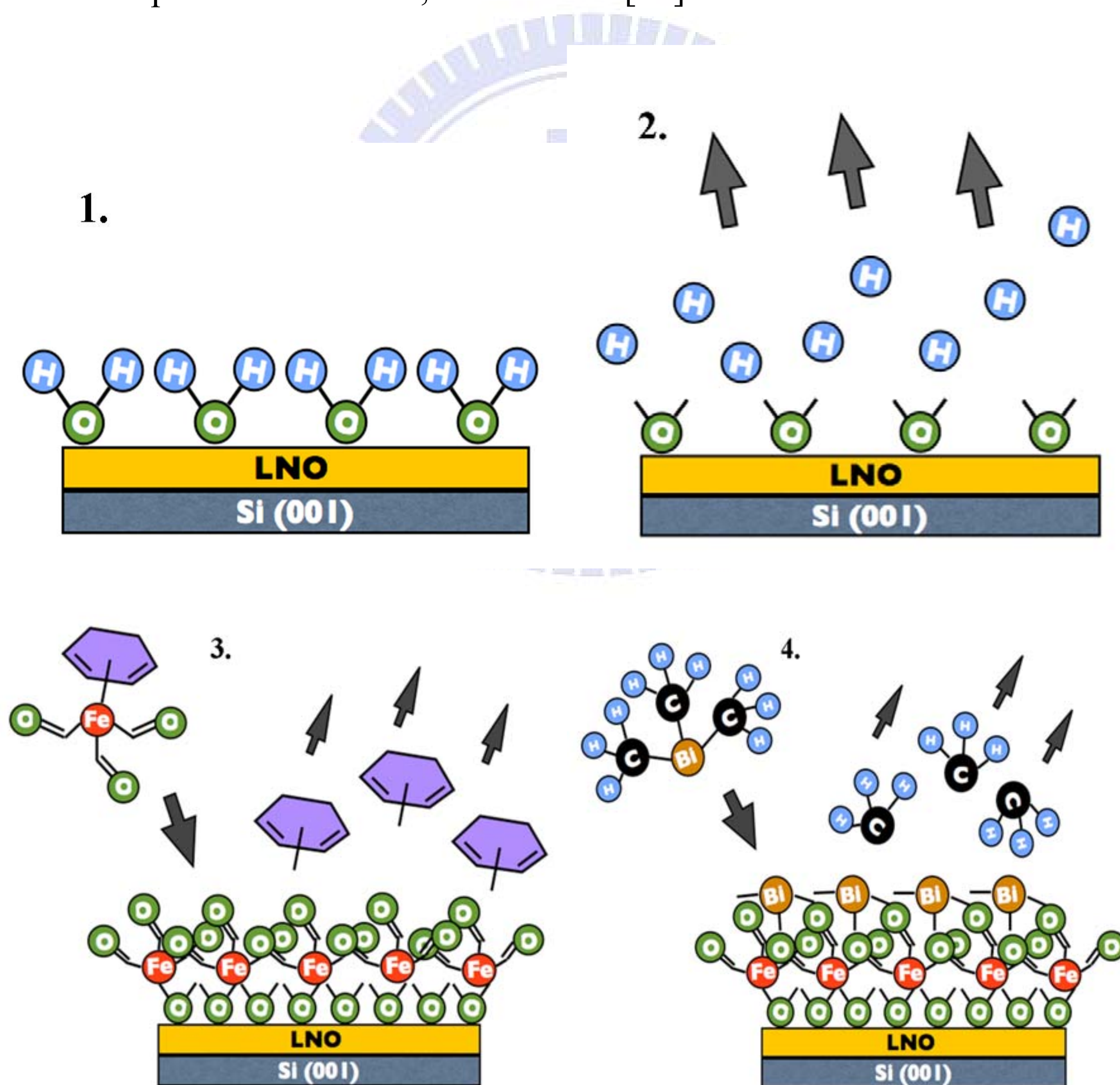

Figure 3.4 ALD deposition process of BFO thin film for one cycle.

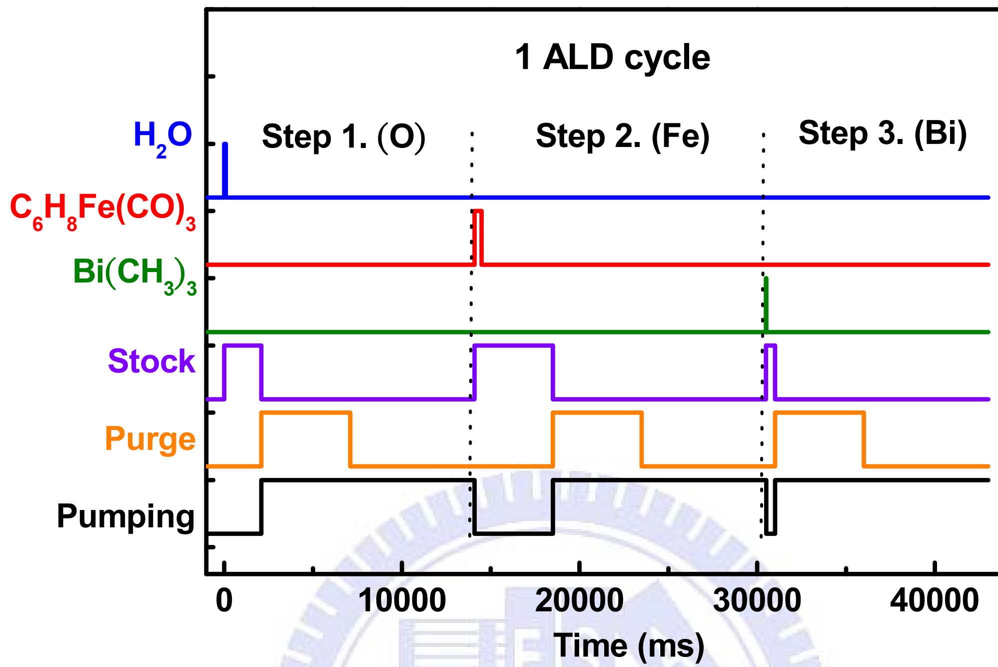

Figure 3.5 Time table of modified ALD process for BFO thin film growth.

3.2 Characterization of structure

3.2.1 X-ray Diffraction and X-ray Reflectivity (XRD & XRR)

X-ray diffraction is a powerful tool to determine the crystal structure and crystalline quality. For this XRD we used a rotating anode for Cu-Kα radiation in a commercial standard two-circle X-ray diffractometer (Max science M18XHF KXY-8019-1) operated at 50 kV and 200 mA in the X-ray laboratory at National Synchrotron radiation Research Center (NSRRC), Hsinchu, Taiwan. The XRD was measured with a 'θ-2θ' scan with scan speed 4° min^{-1} and scaling 0.02^o. Techniques to analyze a thin film play an important role in industry to determine the characteristics of thickness, electron density, interface and surface roughness of thin films. The XRR technique involves the measurement of the radiation reflected from the interfaces and the surface of a multilayer structure that can provide information about the interface [98-101]. Relative to other methods to measure a surface, XRR yields a nondestructive measurement with high resolution from 0.1 nm 1 μm [102]. For XRR that is performed with a Huber two-circle diffractometer, we used the same X-ray source as for XRD. The incident light was made monochromatic with a flat Ge (111) crystal; two pair sets of slits served to eliminate Cu $K\alpha_2$ contamination so yielding a wave-vector resolution in the scattering plane of order 0.015 nm^{-1}.

To derive the physical parameters of a superlattice, the simulation of specular reflectivity is based on the recursive formalism of Parratt [103]. The reflectivity curve is fitted with the $Bede_{RERFS}$ Mercury code [104] to determine the physical parameters of the thin films, including the thickness of each layer, the electron density and the roughness of the surface or interface. This program calculates the reflectivity of the thin film with the dynamic Fresnel equations of

multilayer reflectivity, taking into account the absorption, instrumental resolution, interface roughness and abruptness and sample curvature.

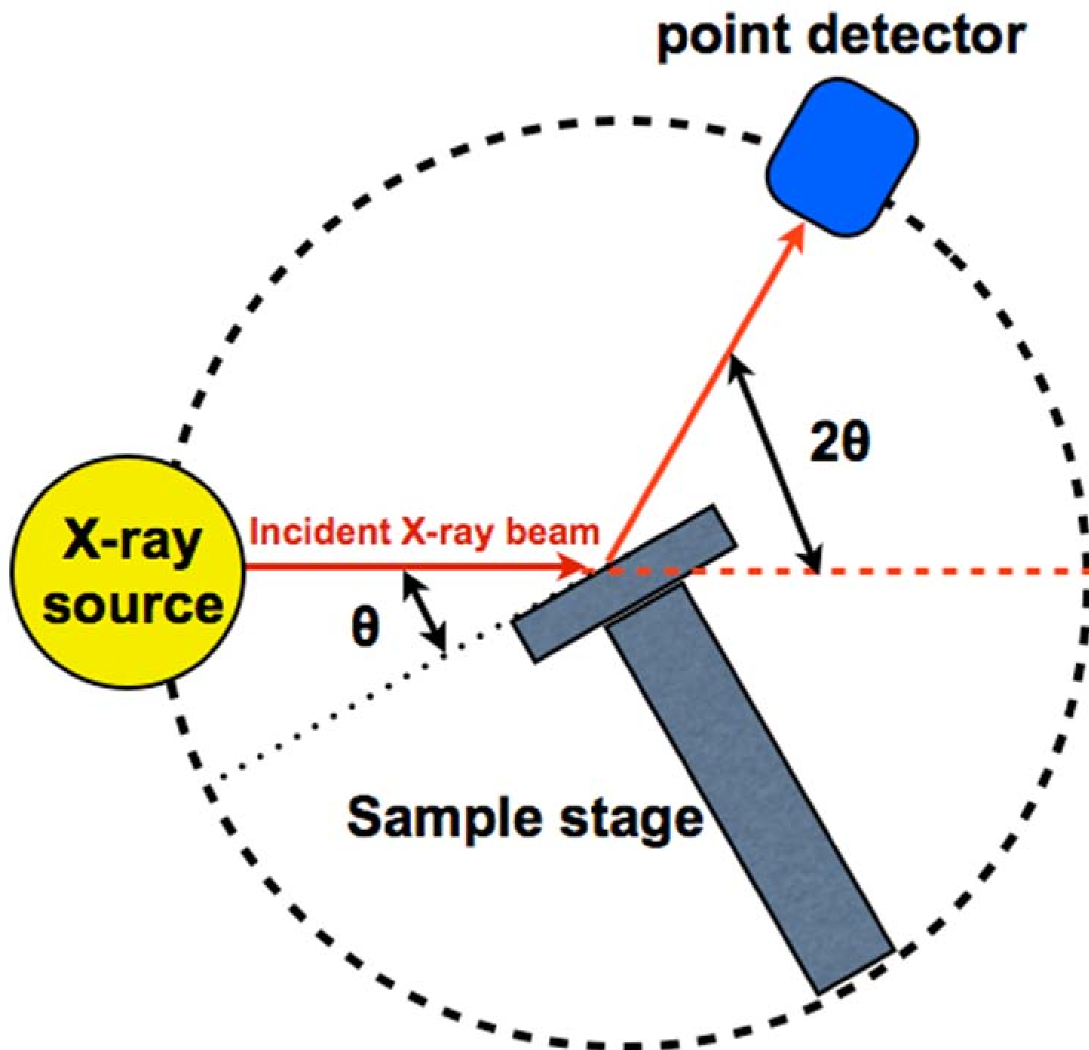

Figure 3.6 X-ray diffraction and X-ray reflectivity.

3.2.2 Synchrotron Radiation X-ray Scattering (SRXRS)

A synchrotron is a cyclic particle accelerator of a particular type in which a magnetic field (to turn the particles so that they circulate) and an electric field (to accelerate the particles) are carefully synchronized with the traveling particle beam. With each turn in the accelerator, an accelerating RF voltage is applied to the charged particles. As the energy of the particles increases, so does the magnetic field of the ring, which maintains a constant radial orbit. Synchrotrons were originally developed by L. W. Alvarez for purposes of high-energy particle physics [105].

An accelerator takes stationary charged particles, such as electrons, and drives them to nearly the speed of light. In being forced by magnets to travel around a circular storage ring, charged particles emit electromagnetic radiation tangentially and, consequently, lose energy. This energy emitted in the form of light is known as synchrotron radiation. The synchrotron produces light on accelerating electrons almost to the speed of light. Magnets restrict the electrons to circular paths. As the electrons turn, photons (packets of radiant energy) are emitted. The infrared and UV light and X-ray are sent down pipes called beamlines, to work areas at which scientists conduct their experiments. The components of a synchrotron include an electron gun, linear accelerator, a circular booster ring (to increase the speed of the electrons), storage ring (to re-circulate electrons) and beamlines [105].

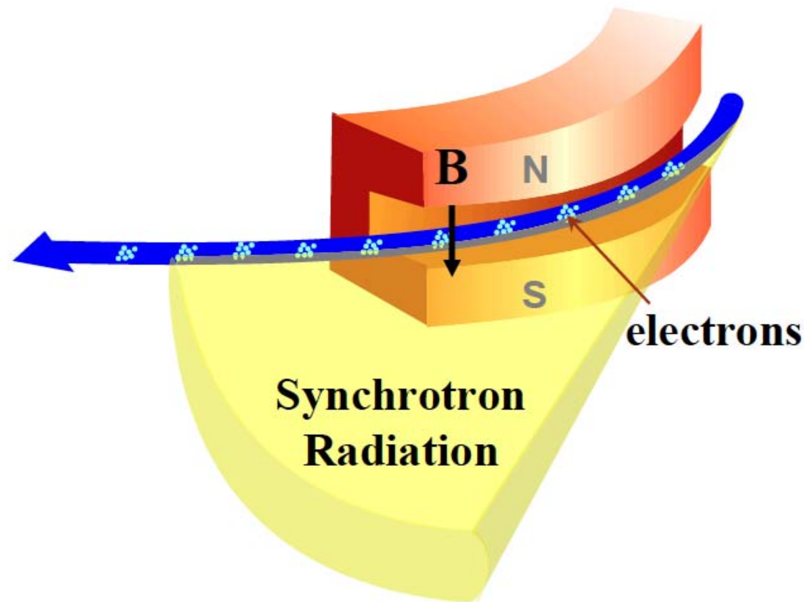

Figure 3.7 Synchrotron Radiation [105].

Basic Theory

Accelerated charged particles emit electromagnetic waves (radiations). A magnetic force is applied to the charged particles -- electrons or positrons -- to provide a central acceleration and to alter the trajectory of the charged particles. Radiation emits tangentially from the trajectory of the charged particles; its spectrum depends on the energy of the charged particles and the applied magnetic field. A RF cavity restores the lost energy of the charged particles and maintains a constant operating energy of the storage ring [105].

The properties of synchrotron radiation (SR) are high intensity and brightness ($I_{SR} > 10^6 \times I_{tube}$), a wide range of continuous spectrum (35 keV > E > 0.05 eV at NSRRC), excellent collimation, low emittance, a pulsed temporal structure, and polarization (linear or elliptical) and coherence [105].

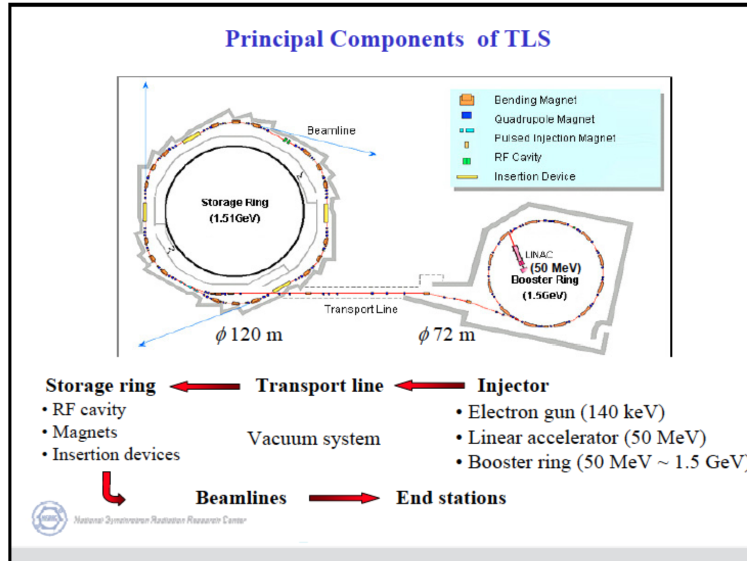

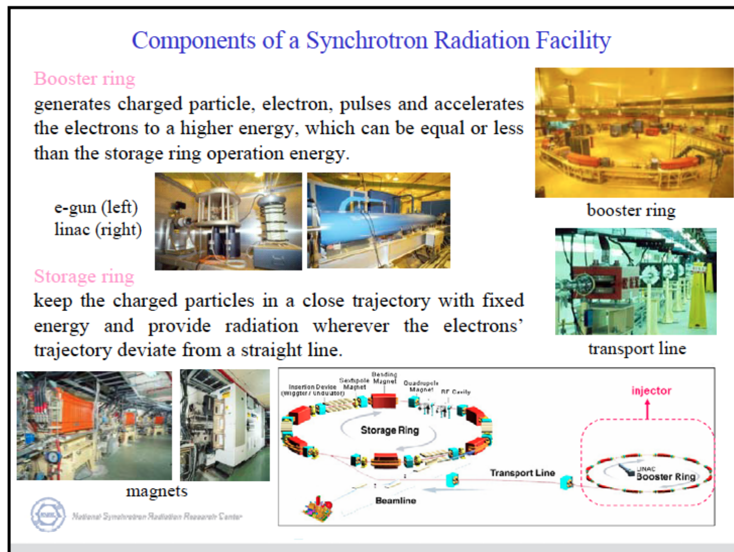

TLS Storage Ring Parameters

Parameter	Value
Number of superperiods	6
Energy	1.5 GeV
Dipole Field	1.432 Tesla
Bending radius	3.495 m
Circumference	120 m
Lattice	Triple bend achromat (TBA)
Rev. freq.	2.49827 MHz
Rev. time (Orbital period)	400 ns
Harmonic No.	200
Bunch length (1σ)	25 ps;
Single bunch current	25 mA
Beam current	300 mA (max. 400 mA)
Natural horizontal beam emittance	$2.56e^{-8}$ m.rad
RF freq.	499.654 MHz
RF voltage	1.6 MV
SR loss/turn	128/161 keV
Critical photon E/wavelength	2.14 keV/5.8 Å λ(Å) = 12.39852/E(keV)
Life time (1.5 GeV, 200 mA)	> 9 hr.

Figure 3.8 Taiwan Light Source (TLS at NSRRC) [105].

The measurement of high-resolution X-ray diffraction (HRXRD) of the radial scan and grazing-incidence X-ray diffraction in plane (GIXRD) were performed at wiggler beamline BL-17B1 with a Huber eight-circle diffractometer at NSRRC, Hsinchu, Taiwan. With two pairs of slits between the sample and the detector, the typical scattering vector resolution in the vertical scattering plane was set to $\sim 1\times10^{-3}$ nm^{-1} in these experiments. The energy range is 4.8 ~ 14.2 keV, wavelength 0.087 nm ~ 0.25 m, energy resolution 2.2×10^{-4}, flux 2×10^{11}, spot size of full width at half maximum 0.6 mm (H) x 0.5 mm (V); the optics comprised a vertically collimating pre-mirror, a fixed-exit double-crystal Si (111) monochromator, a toroidal focusing mirror, and a scintillation counter as detector.

Although SR provides a strong and powerful X-ray source, in some experiments such as for analysis of a thin-film structure, great intensity and flux are urgently needed. An insertion device (ID), used for this purpose in the synchrotron facility, is a component in a modern synchrotron light source that has periodic magnetic structures that stimulate highly brilliant, forward-directed emission of synchrotron radiation on forcing a stored beam of charged particles to perform wiggles, or undulations, as they pass through the device. The Lorentz force causes this motion; from this oscillatory motion we derive the names for the devices of two classes -- wigglers and undulators. An ID is traditionally inserted into a straight section of a storage ring. As the beam of stored particles, generally electrons, pass through the ID, the alternating magnetic field experienced by the particles causes their trajectory to undergo a transverse oscillation. As there is little mechanical difference between a wiggler and an undulator, the criterion normally used to distinguish between them is the K-factor, which is a dimensionless parameter defined as

$$K = \frac{qB\lambda_u}{2\pi\beta mc}$$

in which q is the charge of the particle passing through the ID, B is the maximum magnetic field of the ID, λ_u is the period of the ID, $\beta = v/c$ relates to the speed, or energy of the particle, m is the mass of the accelerated particle, and c is the speed of light. Wigglers are deemed to have $K >> 1$ and undulators to have $K < 1$ [106].

As an insertion device in a synchrotron, a wiggler comprises magnets in a series designed to deflect laterally and periodically (wiggle) charged particles (invariably electrons or positrons) in a beam inside a storage ring of a synchrotron. These deflections create a altered acceleration that in turn produces emission of synchrotron radiation in a broad spectrum tangent to the curve, much like that of a bending magnet, but the intensity is greater because of the contribution of many magnet dipoles in the wiggler. Furthermore, a wavelength (λ) decreased means a frequency (f) increased; this increased frequency is directly proportional to the energy, so that the wiggler creates a wavelength of light with a larger energy [107].

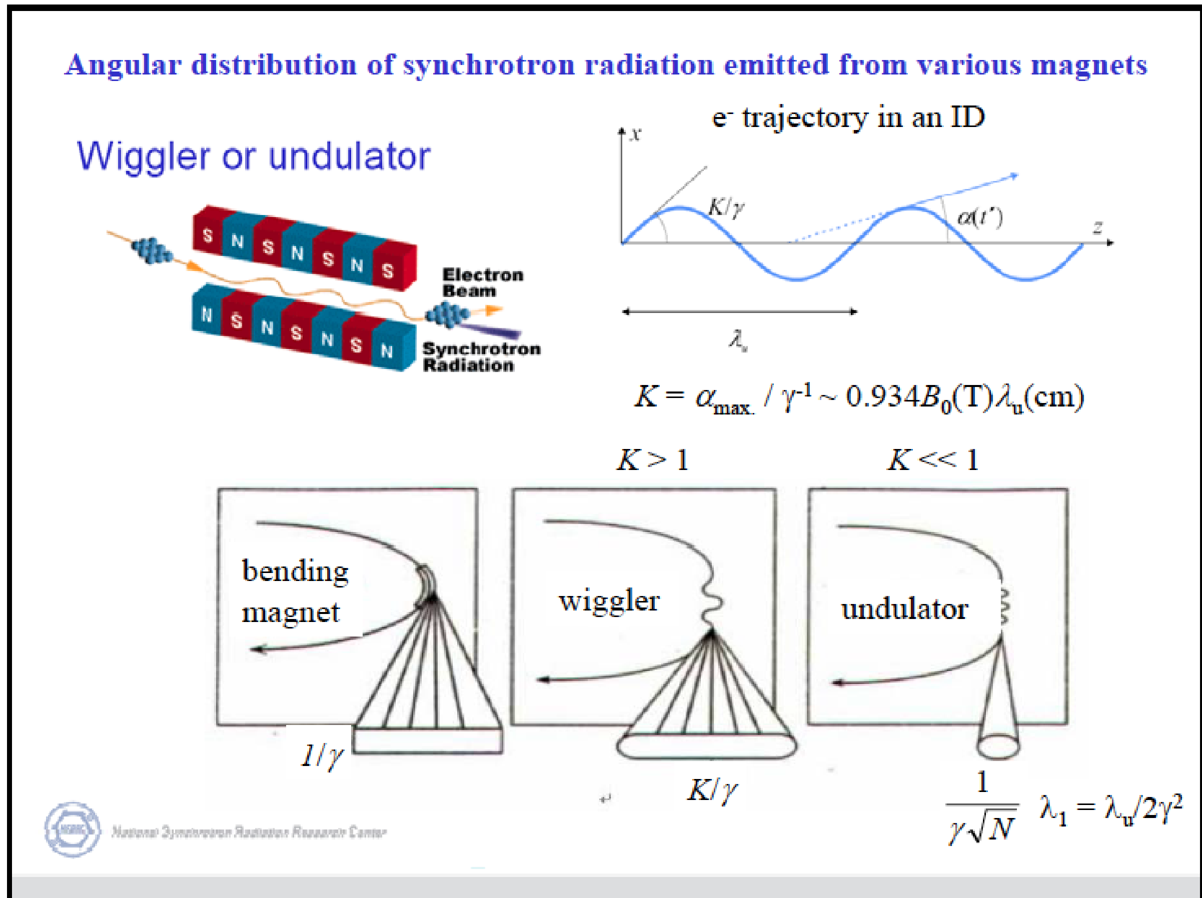

Figure 3.9 Insertion device [105].

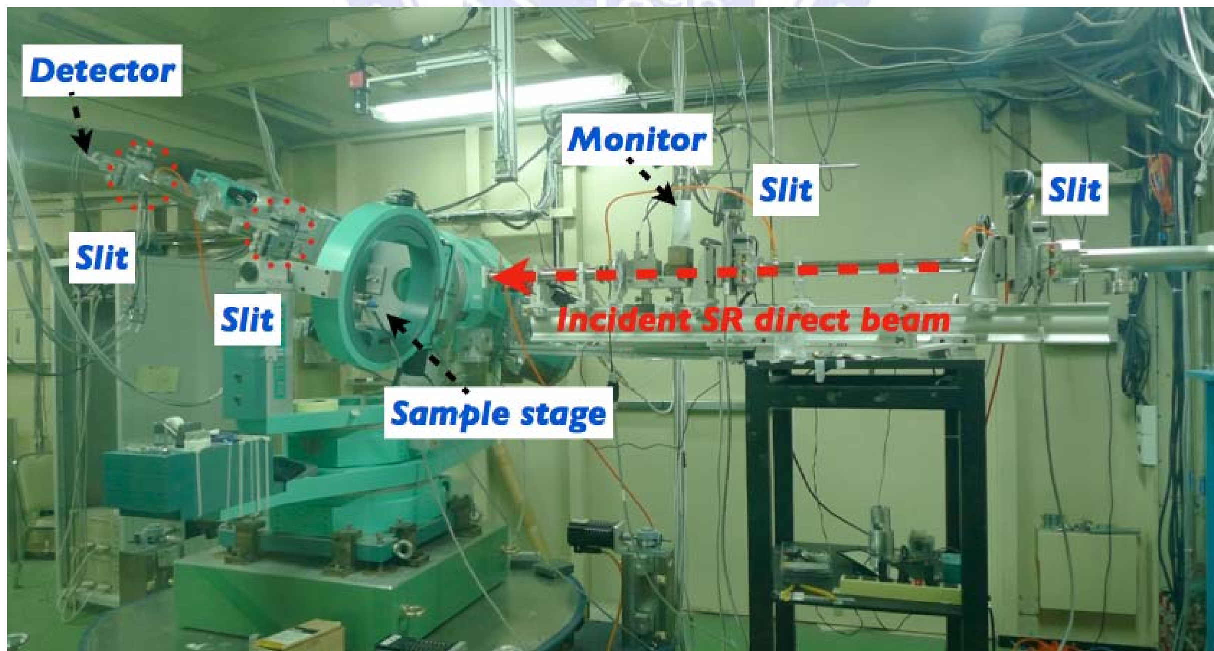

Figure 3.10 NSRRC BL17b1 eight circle diffractometer.

3.2.3 Atomic Force Microscope (AFM)

An atomic-force microscope is a surface-sensitive technique for the surface science of thin-film materials. In a tapping mode, an AFM operates by scanning a tip approaching the end of an oscillating cantilever across the sample surface; the cantilever is driven to oscillate vertically near its resonance frequency with a small piezoelectric element mounted in the AFM tip holder similar to a non-contact mode. The amplitude of oscillation is greater than 10 nm, typically 100 to 200 nm. The interaction of forces acting on the cantilever when the tip approaches the surface -- van der Waals forces, dipole-dipole interactions, electrostatic forces, etc. -- cause the amplitude of this oscillation to decrease as the tip moves nearer the sample. A tapping AFM image is therefore produced on imaging the force of the intermittent contacts of the tip with the sample surface [108]. The feedback loop maintains a constant amplitude of oscillation on maintaining a constant RMS oscillatory signal acquired by the split photodiode detector. The vertical position of the scanner at each data point (x,y) to maintain a constant *setpoint* amplitude is stored in the computer to form the topographic image of the sample surface.

The surface roughness of the superlattice films of BFO/LNO/Si and BFO/LNO was observed with AFM (NT-MDT Solver P47H and Digital Instrument MultiMode) operated in a tapping mode with a silicon-nitride tip. The sample was fixed to an iron disk holder with double-side adhesive tape. The method to detect the cantilever deflection relies on optical interference. As the tip traces various surface features, its vertical movement shifts the laser beam between upper and lower photodiode components, creating voltage differences that are electronically converted into height information. The image is captured with a feedback-loop controller system. The scan rate of the tip was kept

constant at 0.3, 0.5 and 1 Hz; the scanned lines numbered 512; the *z* height was 500 nm, and the scan size was set at 1 x 1 μm^2 and 2 x 2 μm^2.

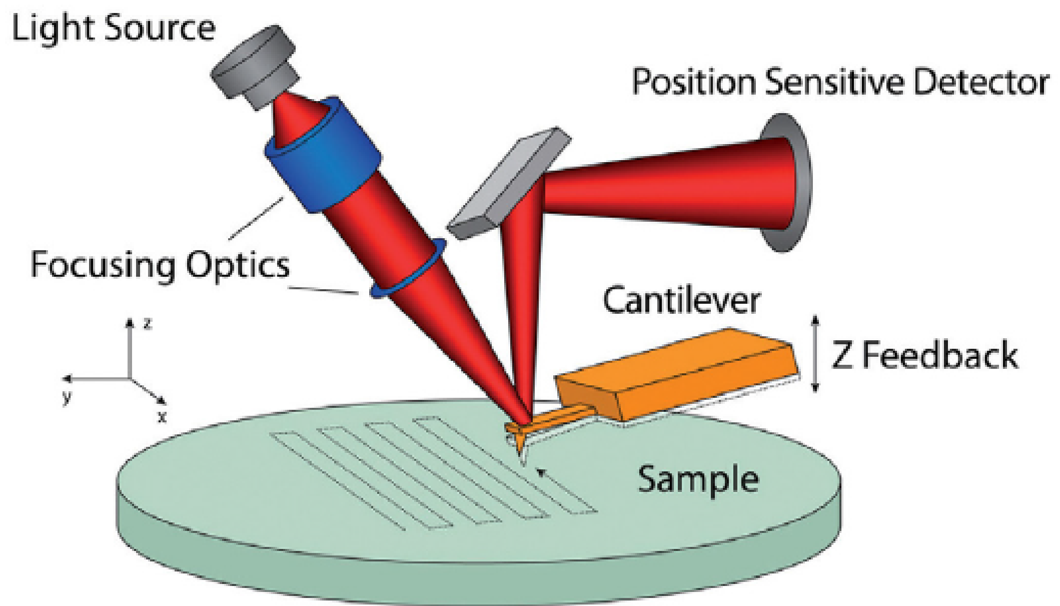

Figure 3.11 Sketch diagram of AFM apparatus [108].

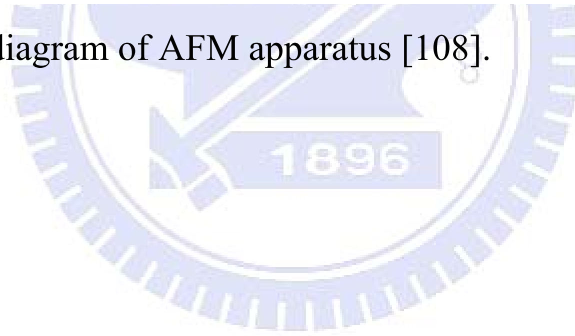

3.2.4 High Resolution Transmission Electron Microscope (HRTEM)

For high-resolution transmission electron microscopy (HRTEM), an imaging mode of the transmission electron microscope allows for direct imaging of the atomic structure of the sample [109]. HRTEM is a powerful tool to study, on an atomic scale, the crystal structure of materials such as semiconductors, metals, nanoparticles and trigonal carbon, e.g. graphene, C nanotubes.

The layer structure and interface roughness of the single-layer BFO thin film and BFO/LNO superlattice are investigated with cross-sectional images from a HRTEM (JEOL JEM2010) to confirm layer and epitaxy of films.

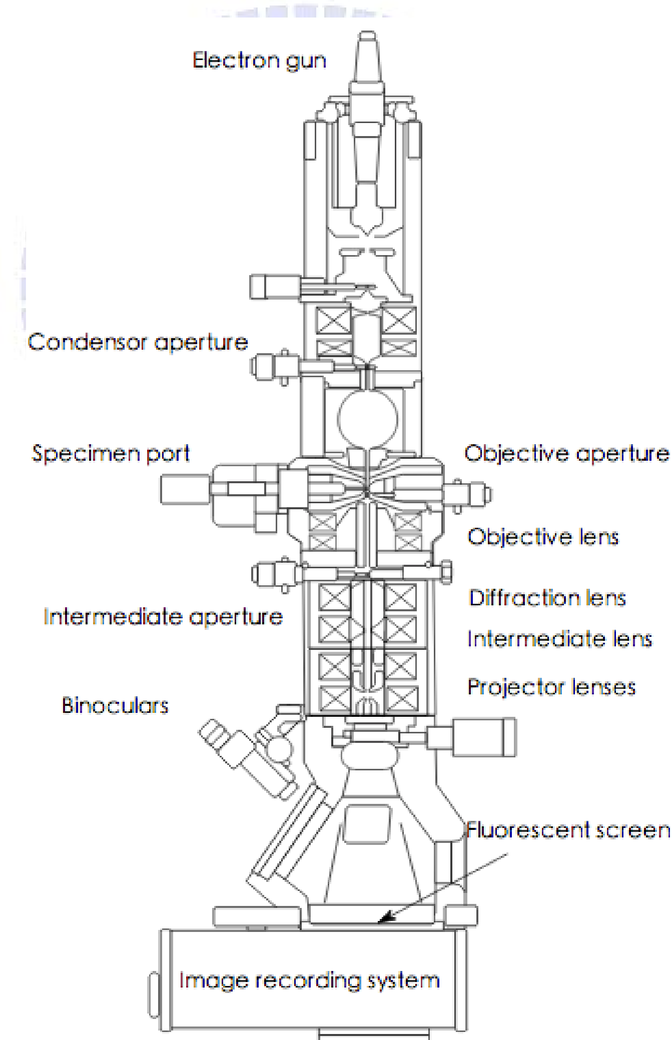

Figure 3.12 Transmission Electron Microscope [110]

3.3 Characterization of properties

3.3.1 Diffraction Anomalous Fine Structure (DAFS)

In general, X-ray scattering represents only information about the long-range ordering of atomic structure, but measurements of X-ray absorption fine structure (XAFS) provide short-range chemical information. DAFS combines all capabilities of XRD and XAFS in a single technique; it provides the advantages of information about short-range order of the set or subset of long-range ordered atoms selected by the diffraction condition [111]. DAFS is specific chemically and to valence, and is sensitive to the positions of neighboring atoms; atoms can be separated on measuring the DAFS intensities of Bragg peaks with varied diffraction structure-factor contributions. DAFS provides the same structural and spectral sensitivities as X-ray absorption near-edge structure, namely the valence, empty orbital and bonding information for the resonant atoms [112,113].

Measurement of DAFS was performed with a synchrotron source at wiggler beamline BL-17B1 with an eight-circle diffractometer at NSRRC, Hsinchu, Taiwan.

3.3.2 Time-of-Flight Secondary-ion Mass Spectrometer (TOF-SIMS)

Secondary-ion mass spectrometry (SIMS) is a technique used in material and surface sciences to analyze the composition of solid surfaces and thin films by sputtering the surface of the specimen with a focused beam of primary ions and collecting and analyzing the ejected secondary ions. The ratios of mass to charge of these secondary ions are measured with a mass spectrometer to determine the elemental or isotopic or molecular composition of the surface to a depth 1 - 2 nm. Because of a large variation in ionization probabilities among materials, SIMS is generally considered to be a qualitative technique, although quantization is possible with the use of standards. SIMS is the most sensitive technique for surface analysis, with limits of elemental detection ranging from parts per million to parts per billion [114].

The composition of the depth profile of the BFO/LNO superlattice was examined with a TOF-SIMS and a Cs^+ ion source (12.5 keV with current 50 nA, CAMECA ims4f, in National Tsing Hua University). The raster size was 250 μm × 250 μm; the rate of sputtering was 0.06 nm s^{-1}.

3.3.3 X-ray Photoelectron Spectra (XPS)

The chemical compositions of BFO thin films were measured with X-ray photoelectron spectra at a vacuum of 10^{-10} torr (PHI 1600 instrument). All XPS data were collected with Mg Kα X-rays at energy 1253.6 eV. The fits of XPS spectra were analyzed with software (XPSPEAK 4.1). The background was subtracted with a linear method and peaks were fitted with a mixed Gaussian-Lorentzian distribution. The atomic fraction of each element of the $BiFeO_3$ films was calculated from the integrated intensity of signals and divided by the relative sensitivity factor, for Bi-4f 9.14, for Fe-2p 2.957, and for O-1s 0.71. The integrated intensity of Bi-4f, Fe-2p and O-1s signals were calculated to obtain the content of Bi, Fe and O with this equation,

$$C_i = \frac{I_i}{I_{Bi} + I_{Fe} + I_O} \times 100\ \%$$

in which i pertains to Bi, Fe or O, and C_i is the content of element i in the thin film.

3.3.4 Ferroelectric Test System (FTS)

Ferroelectricity is a property of a material that has a spontaneous electric polarization that becomes reversible on application of an external electric field [115,116]. The ferroelectric properties of the polarization – electric field (P-E) hysteresis loop of single-layer BFO thin films and BFO/LNO superlattice films were measured with a ferroelectric test system (TF Analyzer 2000 FE-Module, axiACCT Co.) at varied applied frequency in a range 1-5 kHz; the voltage was set at 5 or 6 V with applied current 1mA; a triangular waveform for samples near 300 K. The hysteresis measured the charge stored in a ferroelectric sample on integrating the current required to maintain one terminal of the sample at zero bias. On eliminating the external capacitor, the circuit decreased the effect of parasitic capacitor and allowed a highly accurate characterization of ferroelectric devices. Figure 3.13 shows a schematic diagram of the ferroelectric test system.

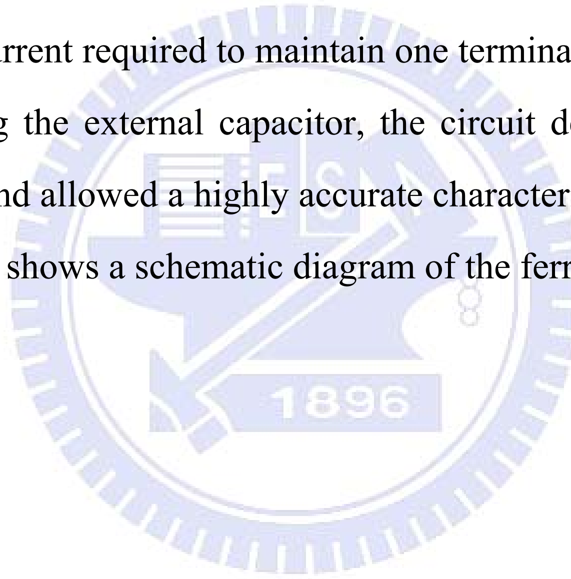

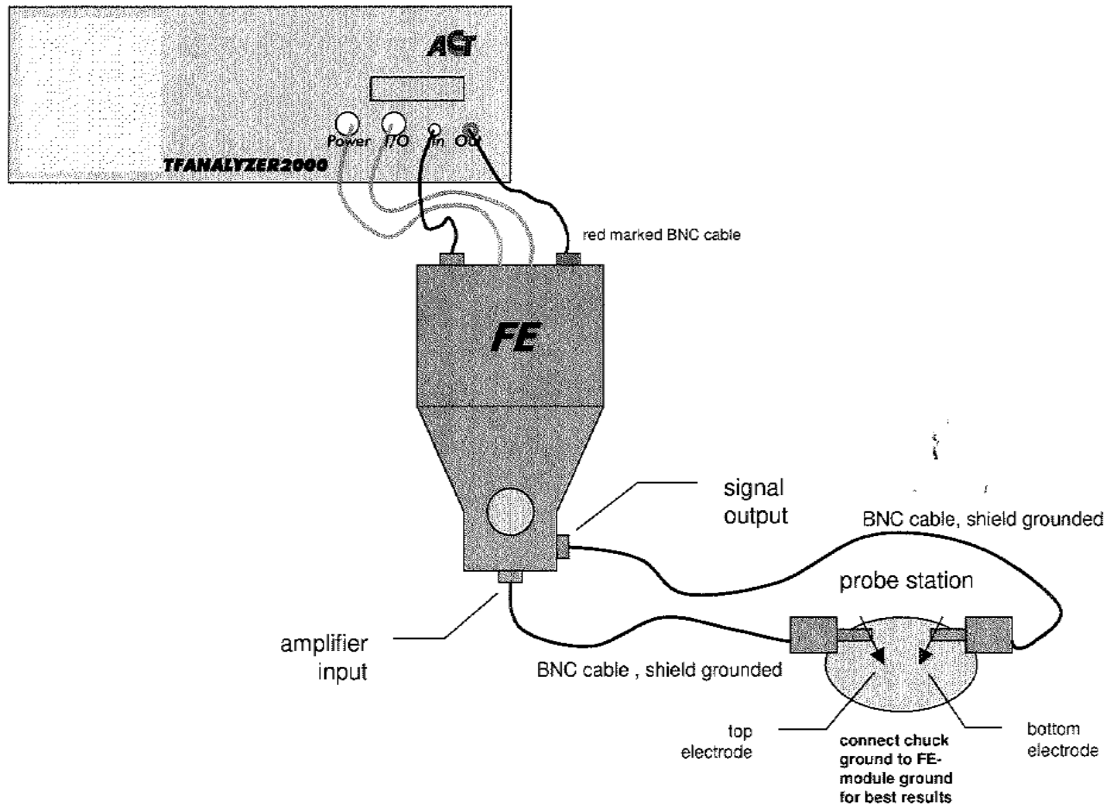

Figure 3.13 Schematic diagram of TF Analyzer 2000 [117].

The excitation signal to measure the hysteresis of a triangular voltage is plotted in Figure 3.14. The polarization pulse establishes a defined state of polarization, the negative state of the relaxed remnant polarization. Following the polarization pulse are three consecutive bipolar excitation signals; each signal is separated with a relaxation time pulse, 1 s [117].

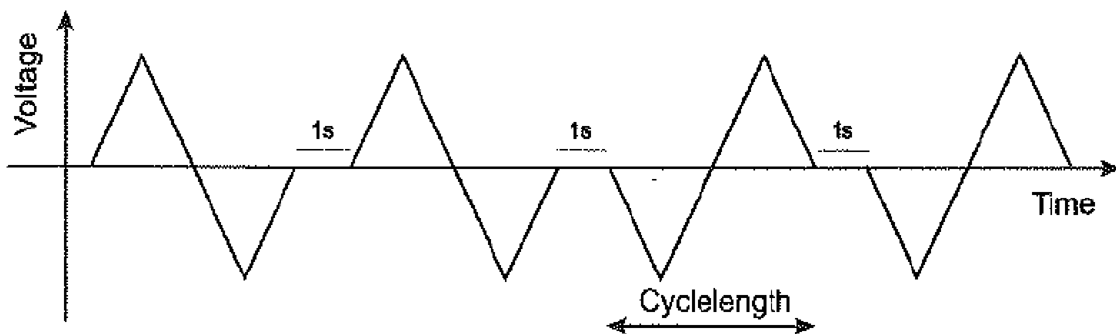

Figure 3.14 Excitation signal for a triangular voltage hysteresis measurement [117].

The leakage current (with TF Analyzer 2000) was measured on applying a voltage waveform of special step shape (shown in Figure 3.15) to the thin films and measuring the current response with a virtual ground amplifier. A ferroelectric capacitor was connected parallel to the sample as the model capacitor, RC-time constants and a voltage-dependent resistor [117].

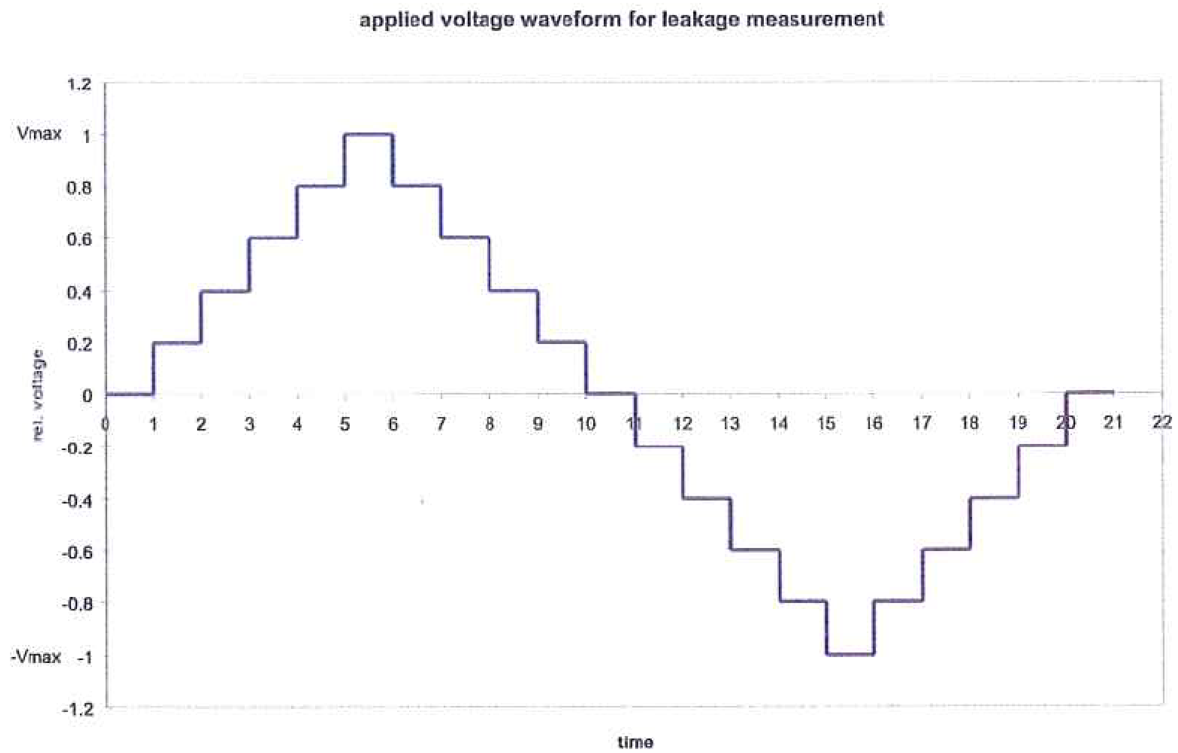

Figure 3.15 Waveform of the leakage current measurement [117].

3.3.5 Positive up and negative down (PUND)

Pulsed polarization analyses, also called positive up and negative down (PUND), is one method to measure the polarization properties of a ferroelectric material. This method avoids the interference from a large leakage and the dielectric properties in the measurement of ferroelectric properties. A PUND polarization test is a powerful tool to probe the ferroelectric behavior of a ferroelectric material without other electrical effect and to derive there from an accurate polarization; the transient current estimated with PUND is related to the leakage current of a ferroelectric material [118-122]. To confirm the results of the P-E hysteresis loops, we determined the ferroelectric properties of the BFO thin films also with the PUND.

The measurement of PUND is made with the same test system (TF Analyzer 2000) at 1 kHz. Figure 3.16 displays a typical function of a PUND measurement. To determine the value of the intrinsic pulsed polarization of a thin film, a pulsed voltage, composed of two positive and two negative pulses, was applied [117].

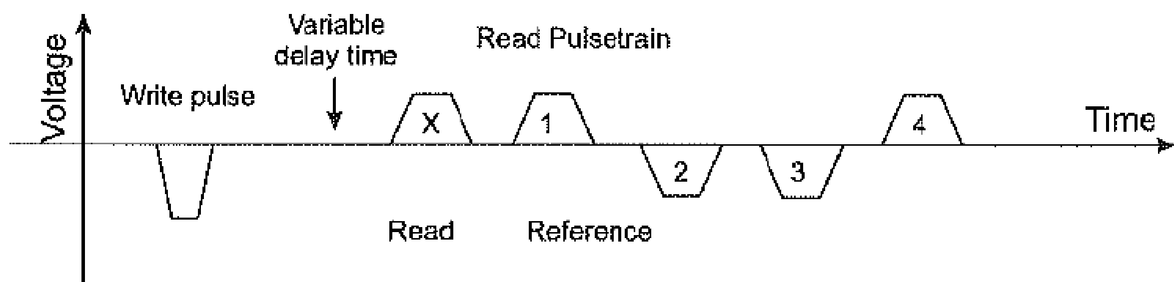

Figure 3.16 Typical excitation of PUND measurement [117].

Chapter 4

Results and Discussion

4.1 Structure and physical properties of the single-layer BFO thin film

4.1.1 Crystal structure of the BFO thin film

To derive the fundamental properties of BFO thin film in terms of the crystal structure and the electrical properties, we investigated initially single-layer BFO thin film. A LNO bottom electrode of thickness 50 nm was deposited on the (001) Si substrate at 500 °C with RF sputtering. BFO films of thickness 60 nm were then deposited on the LNO-coated Si substrate with the RF-sputtering system at temperatures in the range of 300 –700 °C. We used LNO because it was metallic and can serve both as the bottom electrode in fabricating integrated ferroelectric capacitors on Si and as an effective interface for the growth of highly textured ferroelectric thin films [21-24].

Figure 4.1 illustrates the results of conventional XRD ‘θ–2θ’ scan of BFO films deposited on the LNO-coated Si substrate at various temperatures. The film deposited at 300 °C exhibits a weak XRD pattern with broad lines, indicating a poorly crystallized film. At substrate temperature 700 °C, a randomly polycrystalline BFO film resulted, whereas a highly (001)-oriented BFO film was obtained for a substrate temperature in the range of 400 – 600 °C. The BFO (001) and (002) peaks are intense and narrow, indicating the satisfactory crystalline quality of BFO films deposited at 400 – 600 °C. To examine further the texture of the deposited films, we measured the width of the BFO (002) rocking curve (ω scan) as shown in the inset of Figure 4.1.1. The full width at half maximum (FWHM) of BFO (002) rapidly decreased to 3° for deposition temperatures of 400 – 600 °C. Such a narrow rocking curve clearly

demonstrates that the BFO films have a dominant <001> orientation. The narrower is the FWHM of this rocking curve, the better is known to be the crystalline quality.

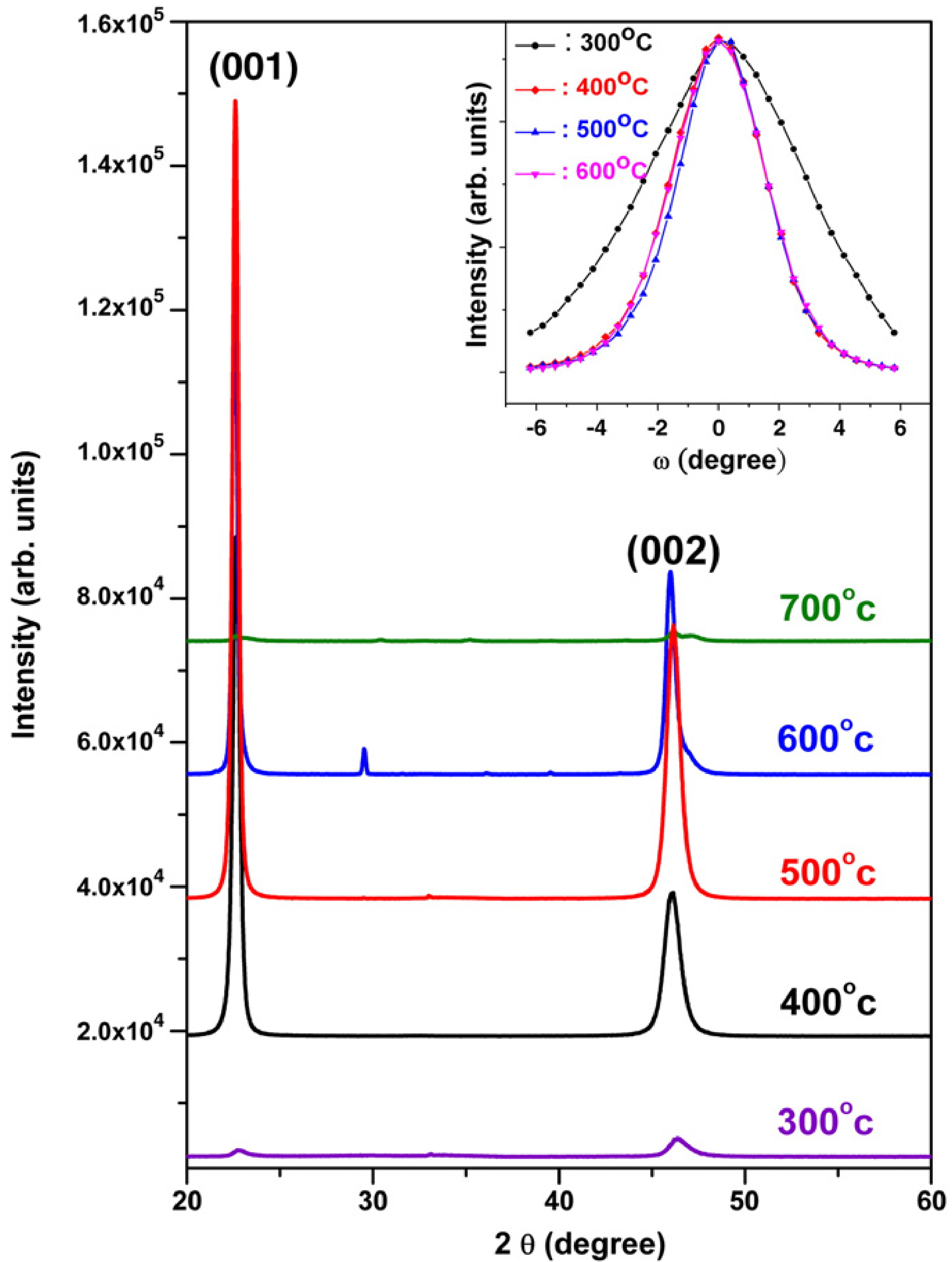

Figure 4.1.1 XRD **"θ–2θ"** scan of BFO films deposited on a LNO-coated Si substrate at various temperatures. The inset shows the width of the BFO (002) rocking curve (**ω** scan).

To examine the in-plane structure of the BFO films, we measured in-plane grazing incidence X-ray diffraction as shown in Figure 4.1.2. The coexistence of (100), (200), (110) and (120) Bragg peaks in the in-plane radial scan along an arbitrary azimuth signifies that the in-plane structure is randomly oriented, as confirmed by the lack of intensity variation of the (110) Bragg peaks in an azimuthal scan (φ scan). The sputter-deposited BFO thin film has an extremely ***c***-oriented columnar textural structure. The XRD result shows that the BFO film deposited at 500 °C has the best (001)-oriented crystal structure.

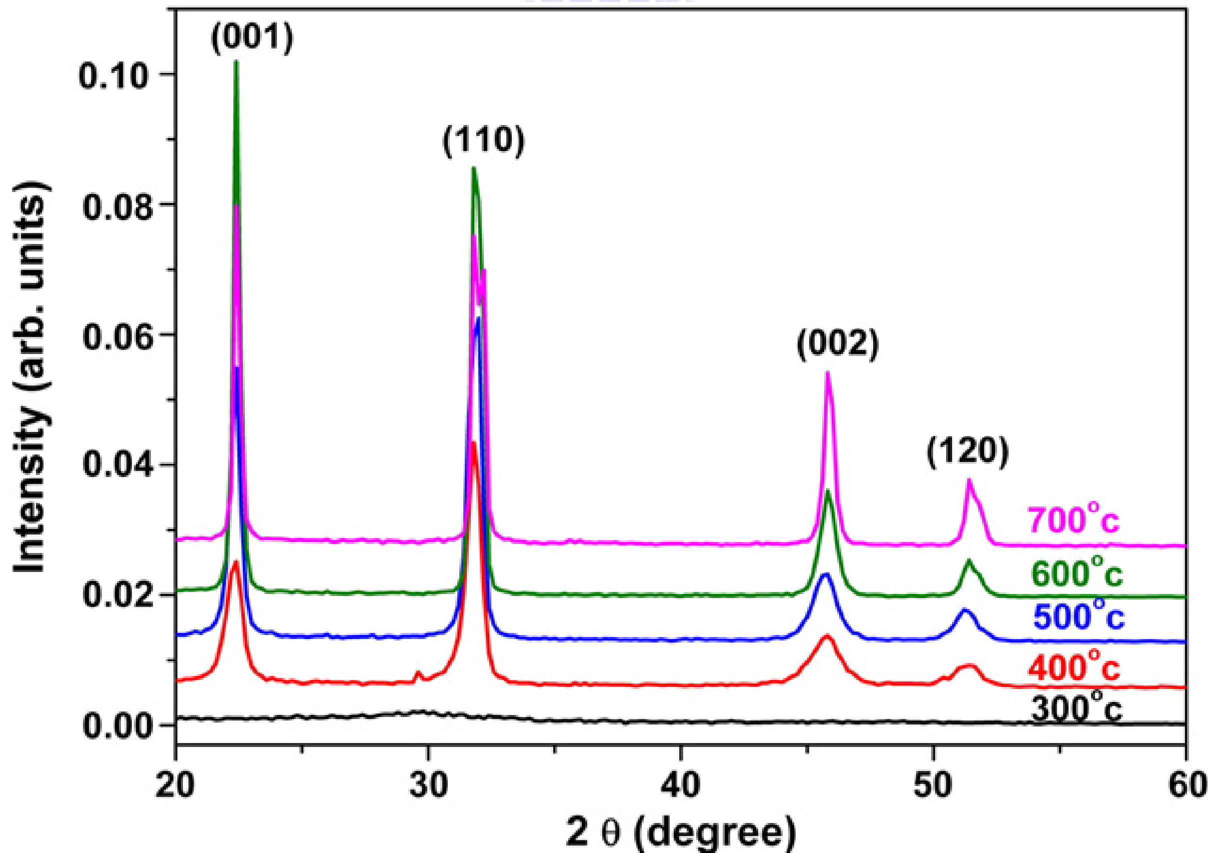

Figure 4.1.2 In-plane grazing-incidence XRD pattern of BFO films deposited on a Si substrate at various temperatures.

Figure 4.1.3 presents reflectivity curves of BFO films deposited on a LNO-coated Si substrate at various substrate temperatures with their best fitted results. For each curve, as the diffuse scattering was measured and subtracted, the data points represent only the specular component. At a small angle of incidence, the footprint of the beam is typically larger than the sample surface, and only part of the light becomes reflected; the increased intensity of reflection is thus due to the surface effect for which the angle of incidence is less than the critical angle of total reflection (θ_c).

To acquire the physical parameters of the films, we used the simulation of specular reflectivity on the recursive formalism of Parratt [103]. We fitted the reflectivity data with the $Bede_{REFS}$ Mercury code [104] to determine the physical parameters of the films, including roughness, thickness, and density. A four-layer model that was adopted consisted of a truncated silicon single-crystal substrate, a native silicon oxide, a layer of LNO bottom electrode, and the deposited BFO film on the top. An expanded view of the best-fitted curve (solid line) and the experimental data (open circles) of the BFO film deposited at 500 °C is shown in the inset of Figure 4.1.3; this fitted curve matches satisfactorily the experimental data. The best-fitted parameters are listed in Table 4.1.1. The reflectivity curve shows that the lower is the deposition temperature, the more clearly present are the Kiessig fringes, and hence the smoother is the surface. The fitted results show that the surface roughness increases with increasing deposition temperature. According to Table 4.1.1, the densities of the BFO and LNO layers were slightly less than their bulk values; this condition likely reflects an increased density of defects inevitably occurring during deposition at high temperature [123,124].

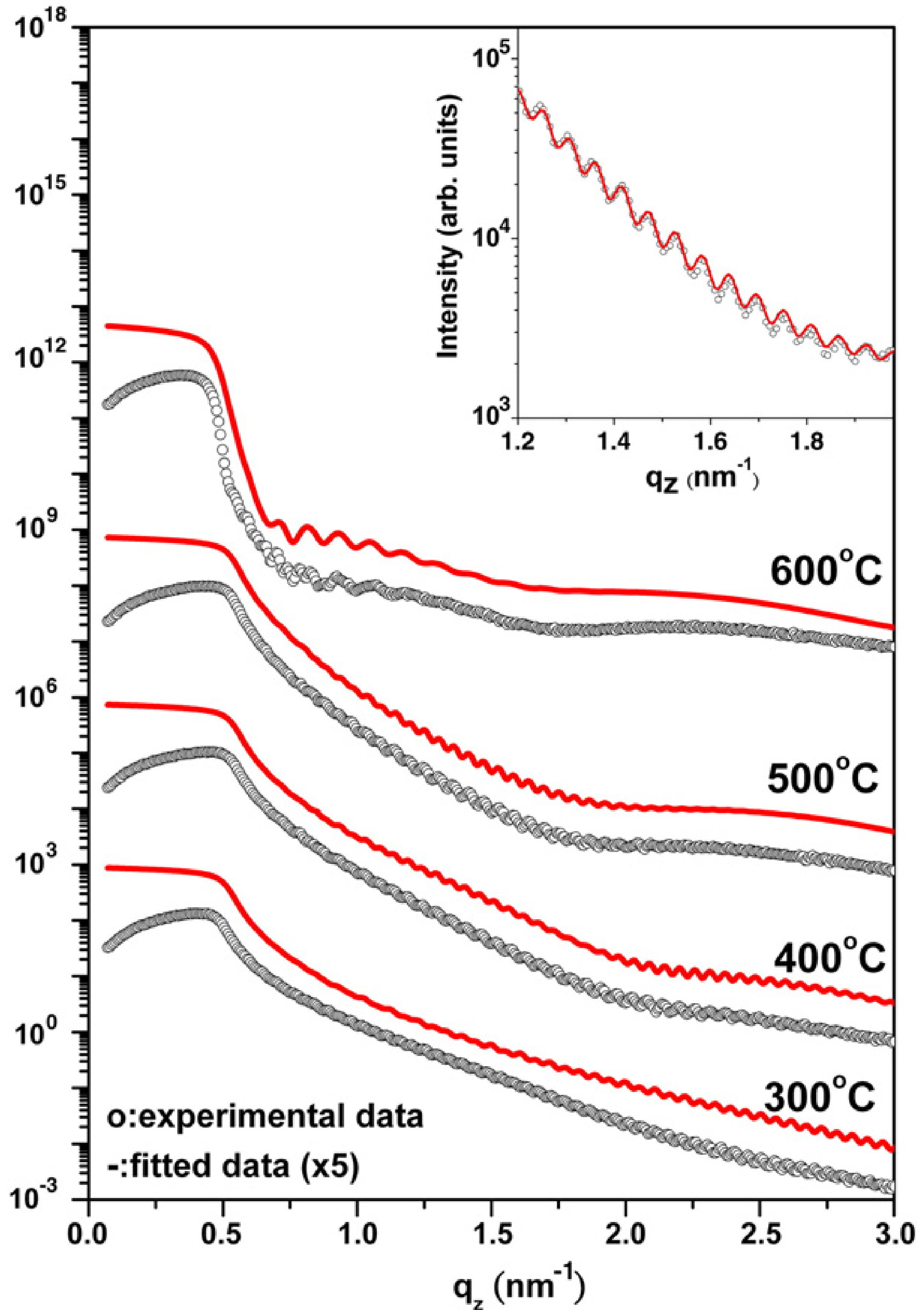

Figure 4.1.3 X-ray reflectivity curve (open circle) of BFO films deposited on a Si substrate at various temperatures and their best-fitted data (solid line) as a function of momentum transfer. The inset shows an expanded view of the best-fitted curve (solid line) and experimental data (open circles) of a BFO film deposited at 500 °C.

To confirm the X-ray reflectivity results, we examined the surface roughness of deposited films with an atomic-force microscope (AFM). From observations conducted in the contact mode on area of 1 μm × 1 μm, we calculated the root-mean-square (RMS) magnitude of surface roughness. The surface morphology of single-layer BFO thin films deposited at various substrate temperatures as examined with the AFM is shown in Figure 4.1.4. For comparison, the surface roughness evaluated from AFM images is listed in Table 4.1.1. The surface roughness of the superlattice films shows the same tendency of increasing surface roughness with increasing deposition temperature.

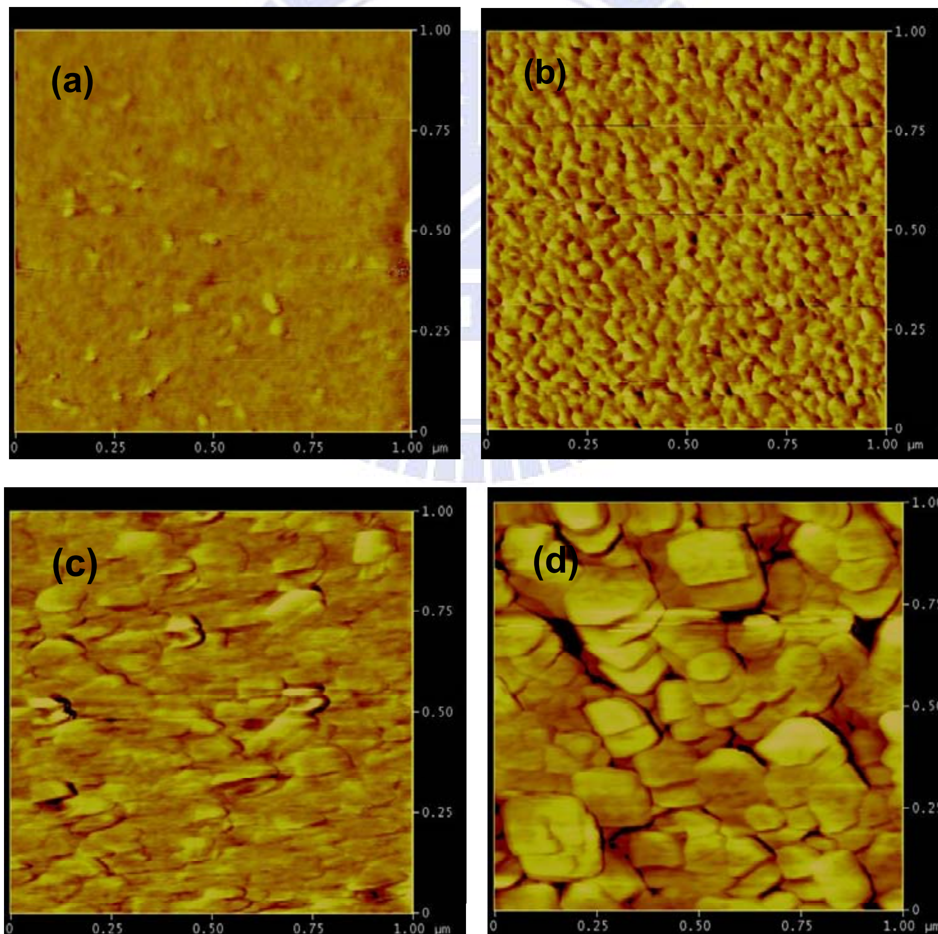

Figure 4.1.4 AFM images of single-layer BFO deposited on the LNO coated si substrate at substrate temperatures/°C: (a) 300, (b) 400, (c) 500 and (d) 600.

Table 4.1.1 Parameters from best-fitted results of reflectivity curves of BFO films deposited on the LNO-coated Si substrate at various temperatures. The surface roughness determined from AFM measurements is listed in the last column for comparison. The relative standard deviations of the fitted data are for thickness ≦2%, density ≦2%, and roughness ≦6%. The thickness of the Si substrate is set as infinite and the bulk density is 2.34 g cm^{-3}. The bulk density of BFO is 8.35 g cm^{-3} and that of LNO is 7.086 g cm^{-3}.

deposition temperature /°C	fitted thickness /nm		fitted density /g cm^{-3}		fitted roughness /nm		AFM /nm
	t_{LNO}	t_{BFO}	ρ_{LNO}	ρ_{BFO}	$\sigma_{BFO/LNO}$	$\sigma_{surface}$	$\sigma_{surface}$
300	**49.00**	**59.80**	**6.732**	**7.685**	**0.77**	**0.52**	**1.1**
400	**46.59**	**60.98**	**6.377**	**8.353**	**1.80**	**0.85**	**1.8**
500	**47.70**	**58.95**	**6.377**	**8.269**	**1.95**	**1.32**	**1.9**
600	**54.00**	**62.00**	**5.137**	**6.348**	**1.00**	**3.90**	**4.6**

The evaluated surface roughness shows the same tendency of increasing roughness with increasing temperature of deposition as that observed in the X-ray reflectivity measurement. The results obtained from these two methods agree satisfactorily.

Because specular reflectivity probes only the variation of laterally averaged electron density along the surface normal, it cannot distinguish an interface with a flat but smoothly varying density distribution from an abrupt but ragged one. To confirm the lateral roughness of the interfaces, we measured also the non-specular diffuse X-ray scattering [98, 125, 126]. The rocking curve of a film deposited at 600 °C taken at 2θ = 1.32°, displayed in Figure 4.1.5, is characterized with an intense central feature associated with the specular peak, as well as two diffuse scattering features on the shoulder (indicated by arrows in Figure 4.1.5), i.e., the so-called Yoneda peaks [19, 22]. The presence of these Yoneda peaks indicates a significant irregularity of the interface or surface of the films. The asymmetry of two Yoneda features is due to the decreasing illuminated area as θ increases.

In the case in which the films conform, i.e., the local maxima and minima of the overlayer surface or interface coincide with local maxima and minima of the underlying interface, the conformity of the roughness produces an oscillating profile of the diffuse scattering, similar to that observed in specular reflectivity. [99, 125] The variation of the diffuse scattering intensity of the film deposited at 600 °C is depicted with open circles in the inset of Figure 4.1.5. For comparison, the specular reflectivity of the same sample is plotted as a solid curve. The absence of any oscillation fringe in the diffuse scattering indicates that no conformal relation exists between the layer and the substrate in this sample. This loss of correlation might be resulted from the random-walk process in atomic

deposition that would smear the original roughness near the surface and hence become uncorrelated as the interface front moves away from the surface [127]. Moreover, the deposited films, even with a highly (001) texture, do not become an epitaxial layer; the growth rate of each grain is hence not exactly the same.

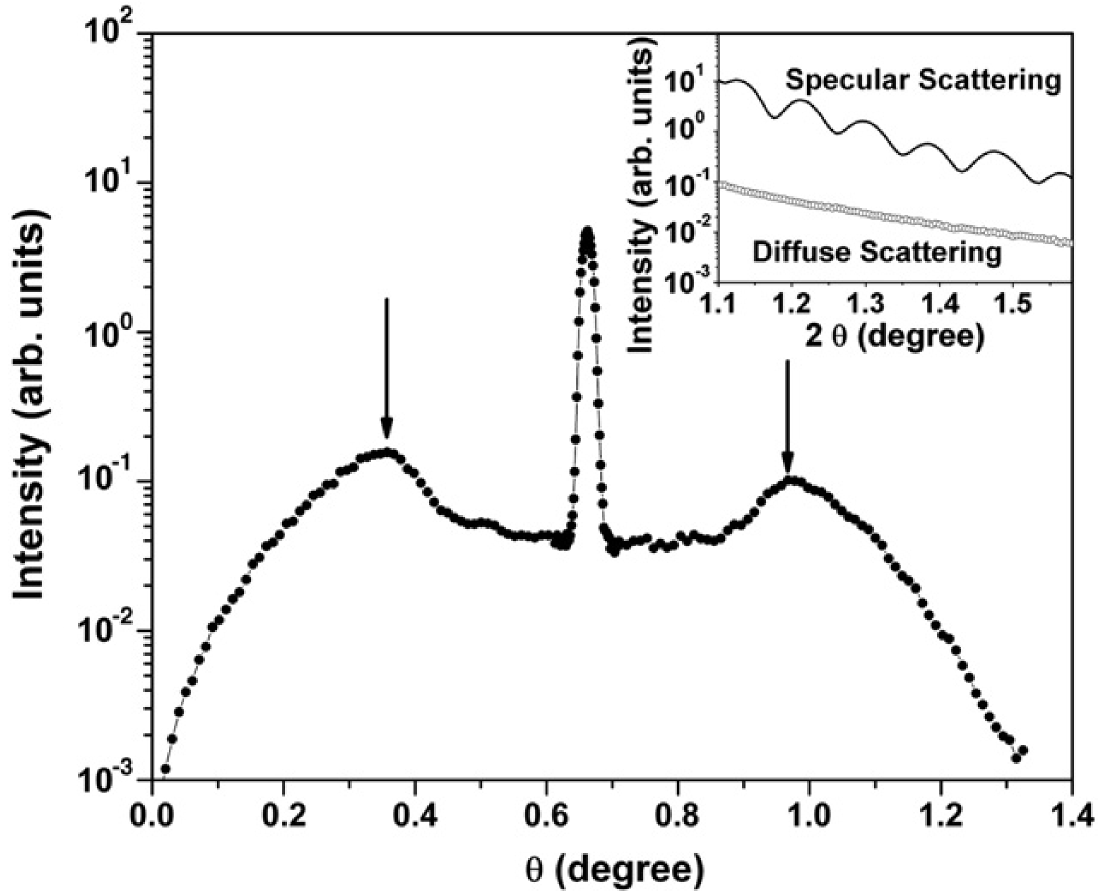

Figure 4.1.5 Rocking-curve measurement of the BFO film deposited at 500 °C. The arrows indicate two diffuse scattering peaks on the shoulder. The inset shows a comparison of intensity curves between specular and diffuse X-ray scattering.

4.1.2 Electrical properties of the BFO thin film

A layer of Pt was subsequently deposited on the BFO thin films through a shadow mask to form a Pt/BFO/LNO/Si stack at ~25 °C for tests of the ferroelectric properties. A hysteresis curve of polarization – electric field (*P–E*) was measured with a ferroelectric test system, at frequency 1 kHz and ~25 °C. Figure 4.1.6 shows *P–E* hysteresis loops of BFO thin films deposited on the LNO-coated Si substrate at various temperatures. The BFO film deposited at 500 °C possesses the largest remanent polarization (P_r). The greater is the remanent polarization and the more nearly square the loop of the *P–E* curve, the smaller is the full width at half maximum of the (002) rocking curve and the more preferable is orientation (001) of the crystal structure of a BFO film deposited at 500 °C.

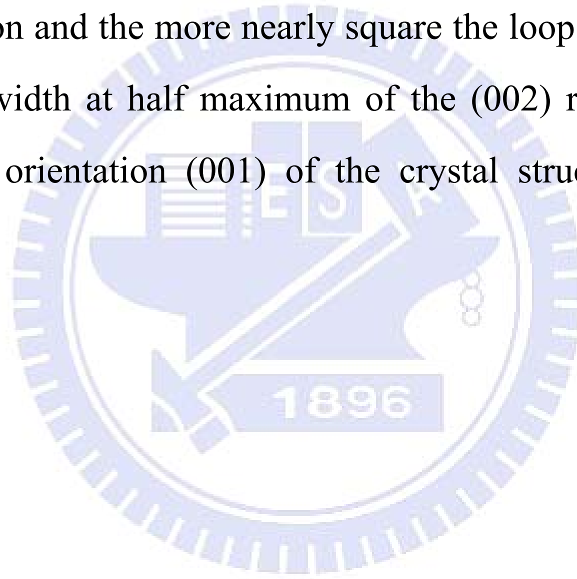

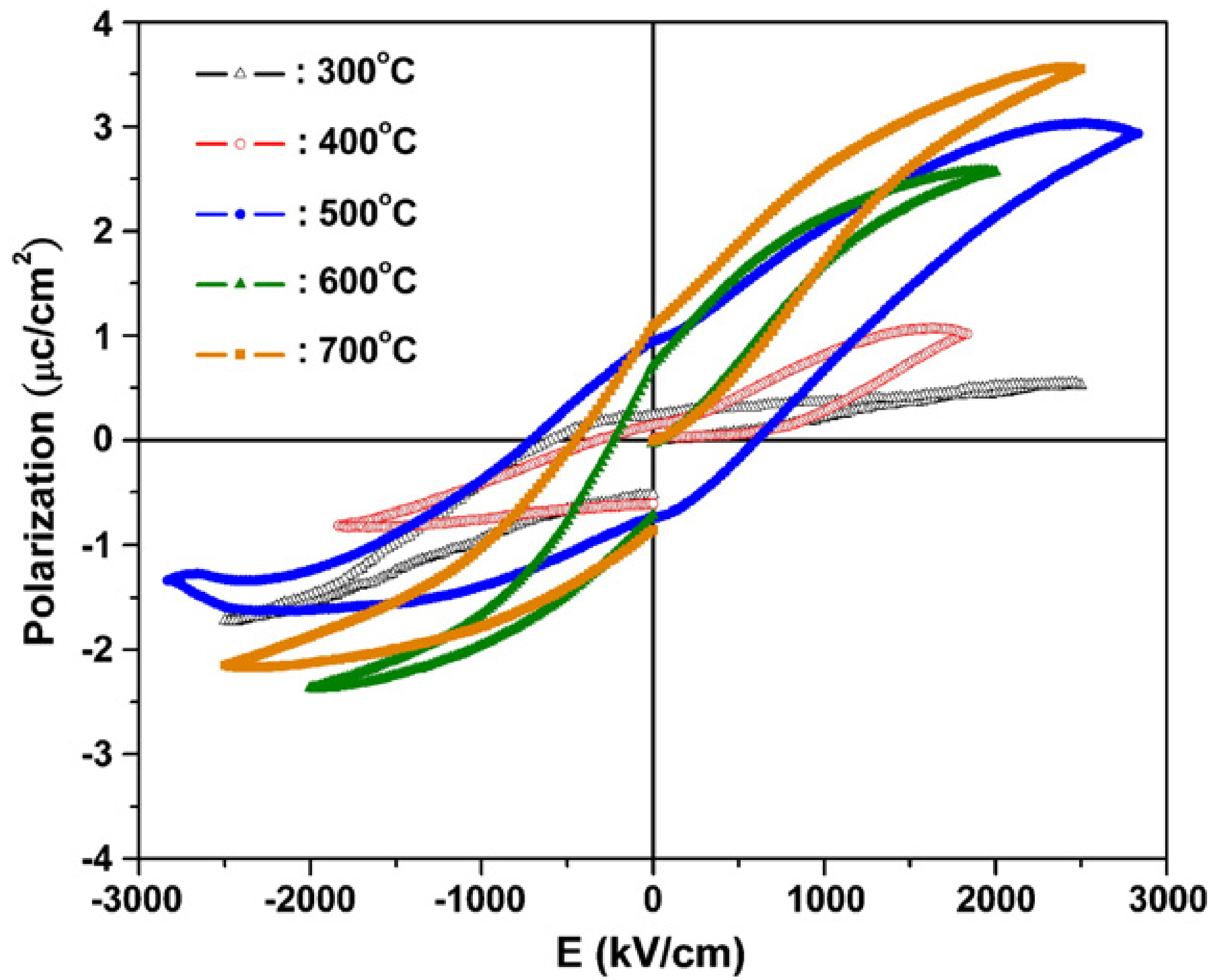

Figure 4.1.6 P–E hysteresis loops of BFO films (thickness 60 nm) deposited on the LNO-coated Si substrate at various temperatures.

Figure 4.1.7 shows the J-E curve of singe-layer BFO thin films deposited on Si substrate with LNO buffer layer at various deposition temperatures that indicates that there exist large leakage current densities for all deposition temperatures. This is a major problem of the BFO thin film; the large leakage current also had a strong interference on the ferroelectric properties. In order to get an intrinsic and large polarization value the leakage issue should be reduced.

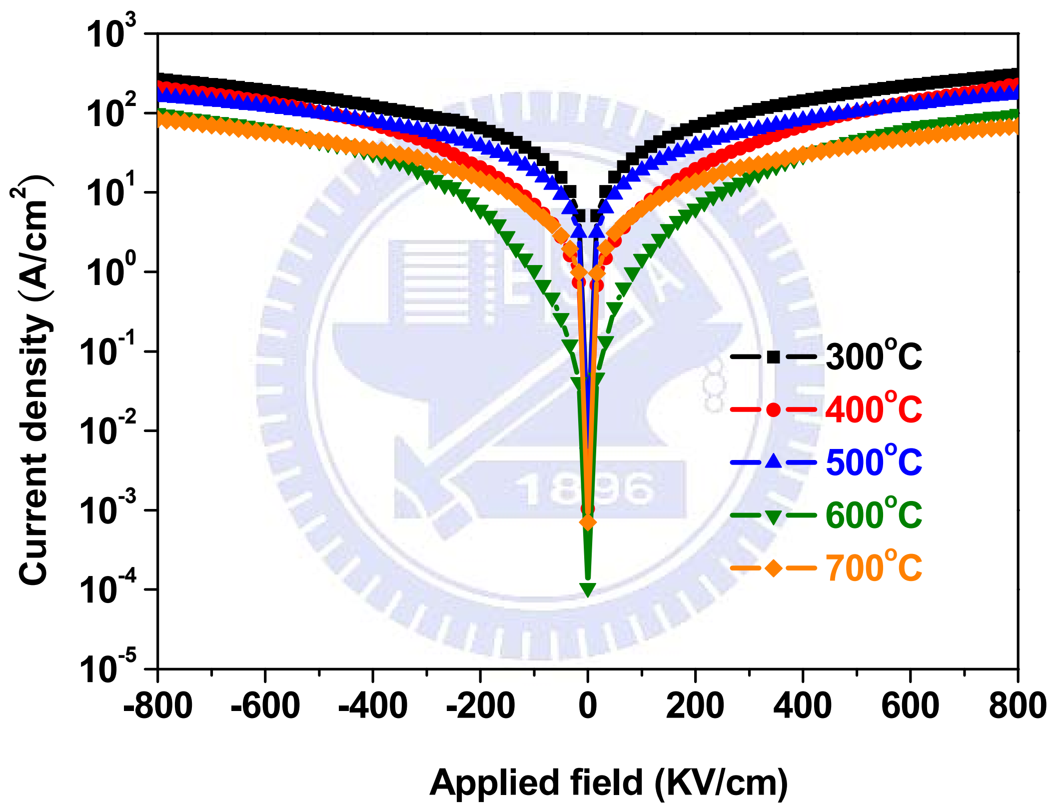

Figure 4.1.7 J-E curve of single-layer BFO thin films deposited at 300 – 700 °C.

4.2 Epitaxial growth and effect of strain on the BFO/LNO superlattice

The physical properties of the single-layer BFO thin film were studied in previous work. The highly (001)-oriented single-layer BFO thin film shows poor electrical properties and a large leakage current. To enhance the ferroelectric properties and to decrease the leakage current, we studied the effect of strain on the polarization of the BFO thin film at the same time that we fabricated the BFO/LNO superlattice thin film.

4.2.1 Structure of the BFO/LNO superlattice

The BFO/LNO superlattice was grown on a conductive Nb-doped single-crystal STO (001) substrate at temperatures in the range of 560 – 810 °C with a UHV double-gun RF magnetron-sputtering system. Figure 4.2.1 shows the radial scan along direction (00*L*) of the BFO/LNO superlattice thin films at various temperatures. Values of *H*, *K*, and *L* stated in this work are expressed in reciprocal lattice units referred to the STO lattice parameter, 0.3905 nm at 25 °C. The intense and sharp feature centered at L=2 is the STO Bragg reflection (002) from the substrate. Satellite peaks of several orders are clearly observed on both sides of the main peaks (marked with arrows in Figure 4.2.1) at all deposition temperatures. An expanded view of the radial scan of the BFO/LNO superlattice film deposited at 660 °C is shown in the inset of Figure 4.2.1. The main peaks and satellite peaks accompanied by clearly discernible Pendellösung fringes on both sides of the main peak indicate the high crystalline quality of the BFO/LNO artificial superlattice structure formed on the STO substrate with RF magnetron sputtering.

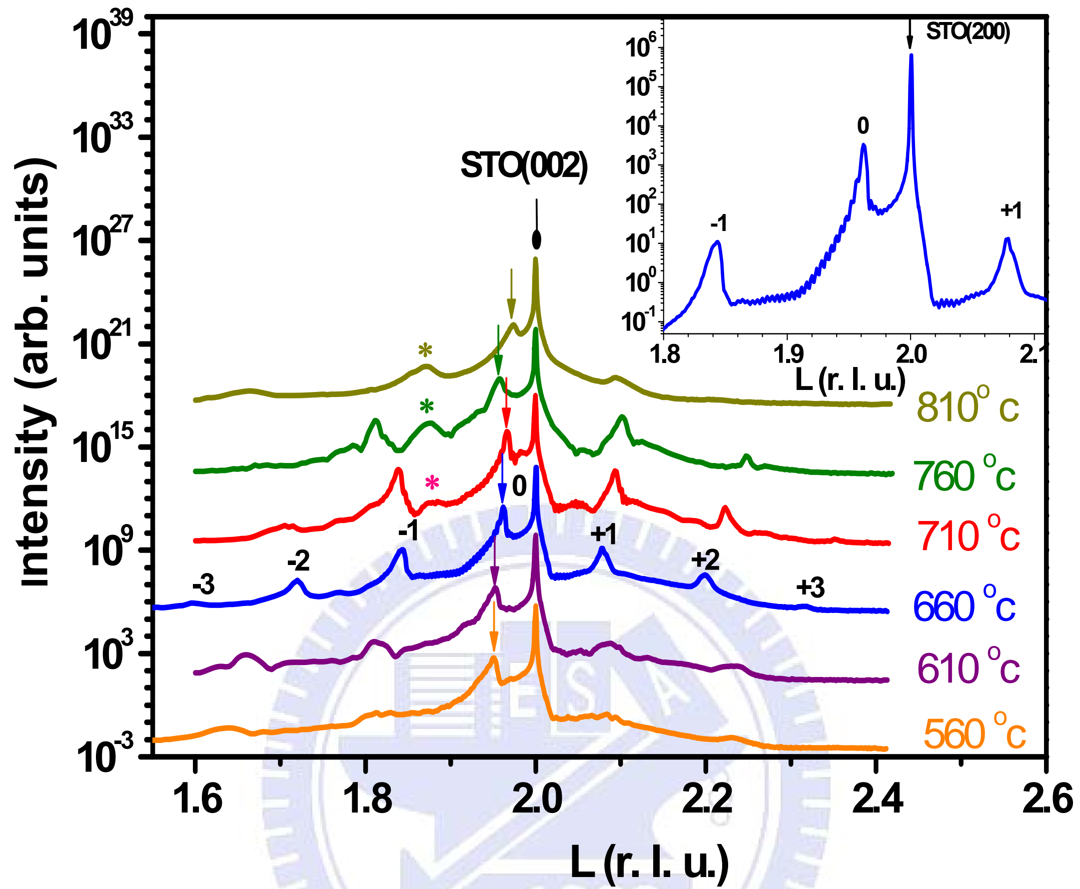

Figure 4.2.1 Intensity distribution of the (002) radial scan of the BFO/LNO superlattice film deposited at various substrate temperatures. The inset shows an expanded view of the superlattice film deposited at 660 °C.

The epitaxial nature of the BFO and LNO sublayers in the superlattices is demonstrated by the in-plane orientation (2 0 0) with respect to the major axes of the STO substrate. The distribution of the in-plane X-ray intensity of the radial scans from superlattice films with varied deposition temperature is shown in Figure 4.2.2; the scan was performed in the vicinity of the STO (2 0 0) Bragg peak. A broad feature coexists with a sharp Bragg peak, which originates from the substrate. This broad feature, indicated by arrows in Figure 4.2.2, is assigned to the Bragg peak of the deposited layer, which is confirmed by the variation of the relative intensity between the two signals as a function of angle of incidence. The *H*-value of the in-plane main peak (marked with arrows in Figure 4.2.2) decreases and approaches the STO substrate with increasing temperature of deposition in the range of 560–660 °C.

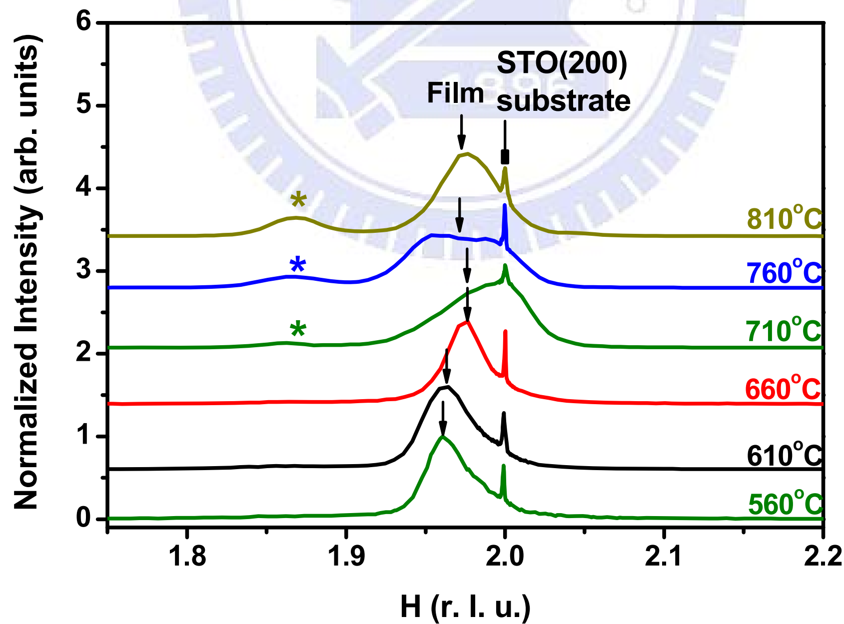

Figure 4.2.2 X-ray intensity of the radial scans along the (200) in-plane Bragg peak of BFO/LNO superlattice films deposited at varied substrate temperatures. An arrow marks the position of the superlattice main peak.

The azimuthal diffraction patterns of the BFO/LNO superlattice film, deposited at 660 °C, in the vicinity of a surface peak and the substrate Bragg peak clearly exhibiting a four-fold symmetry with the same orientation appear in Figure 4.2.3. These results constitute evidence for strong epitaxial growth of the deposited layer on the substrate. No other feature is observed in the intervals between the four peaks, indicating a perfect alignment of axes *a* and *b* of the BFO and LNO unit cells along those axes of the STO substrate. The measurement of the radial scan around the (111) Bragg peak provides further structural information about the off-normal orientation. The radial scan around the (111) Bragg peak for the BFO/LNO superlattice film deposited at 660 °C is shown in Figure 4.2.4; distinct satellite peaks on both sides of the main peak are clearly observed, indicating that not only a well defined epitaxial relation with the substrate has developed along the (111) plane but also a smooth surface and an interface were formed.

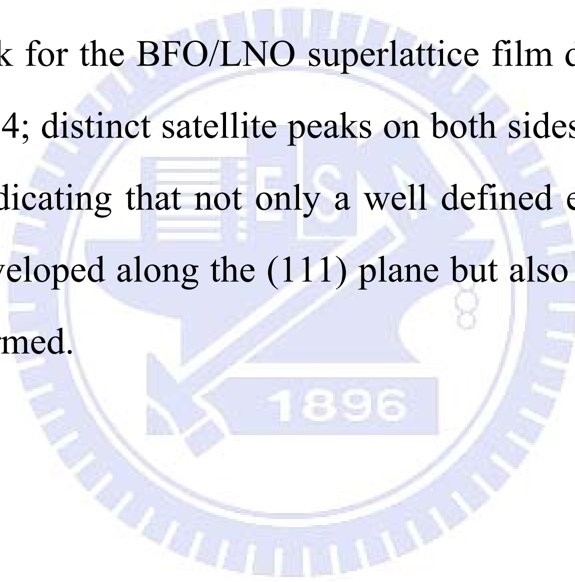

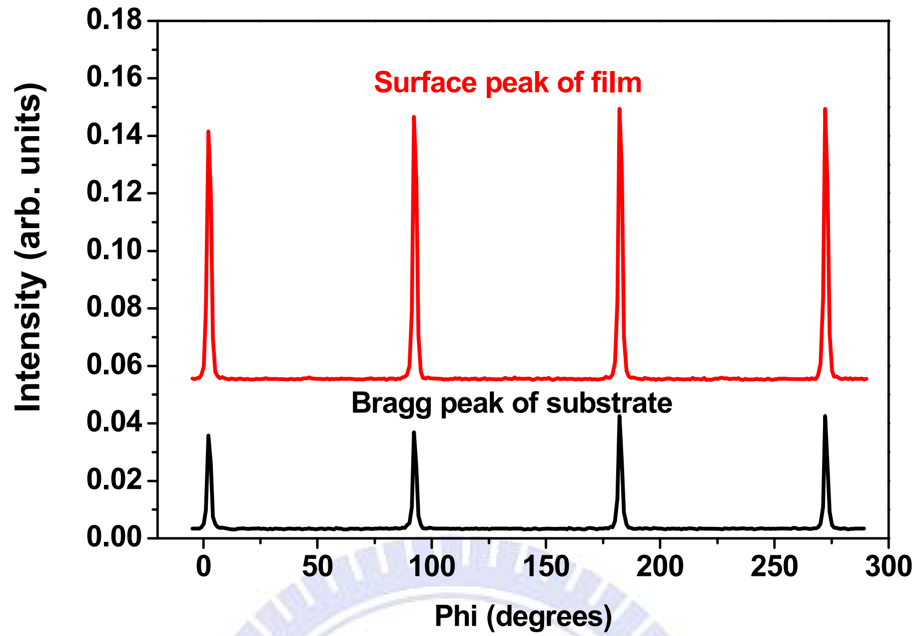

Figure 4.2.3 Azimuthally scan (Φ scan) of the surface peak and the substrate Bragg peak for a superlattice film deposited at 660 °C.

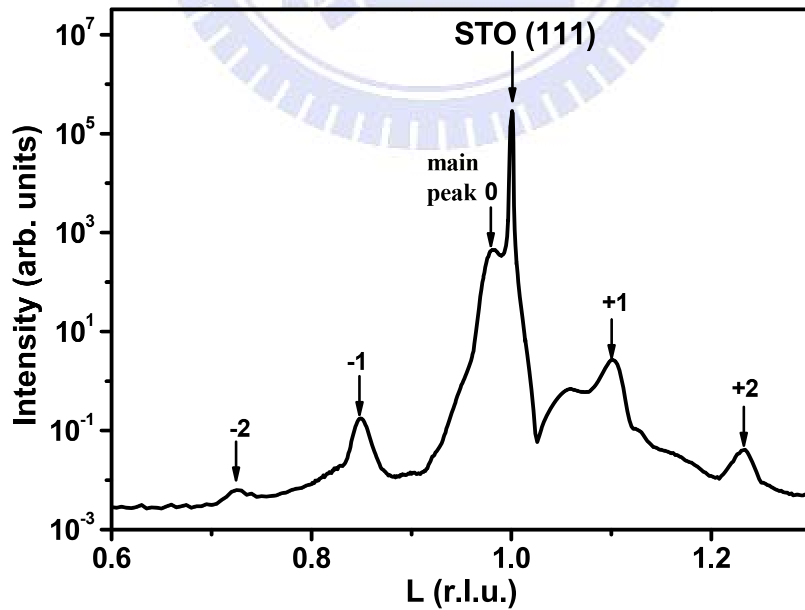

Figure 4.2.4 Intensity distribution of the (111) radial scan of the BFO/LNO superlattice film deposited at 660 °C.

To confirm these X-ray diffraction results of the structure layer by layer and the crystalline quality, we examined the superlattice films with a high-resolution transmission electron microscope (HRTEM) at selected cross sections. Figure 4.2.5 illustrates the HRTEM cross-sectional images of a superlattice film prepared at 660 °C. According to Figure 4.2.5(a), a cross-sectional HRTEM image on a large scale, the superlattice film clearly shows a well defined structure of BFO/LNO layer by layer with the STO substrate; the thickness of the sublayer agrees satisfactorily with the designed value. Figure 4.2.5(b), a HRTEM image, indicates a satisfactory epitaxial relation between the film, interface and substrate, consistent with the experimental results of X-ray scattering of the surface normal and the in-plane direction.

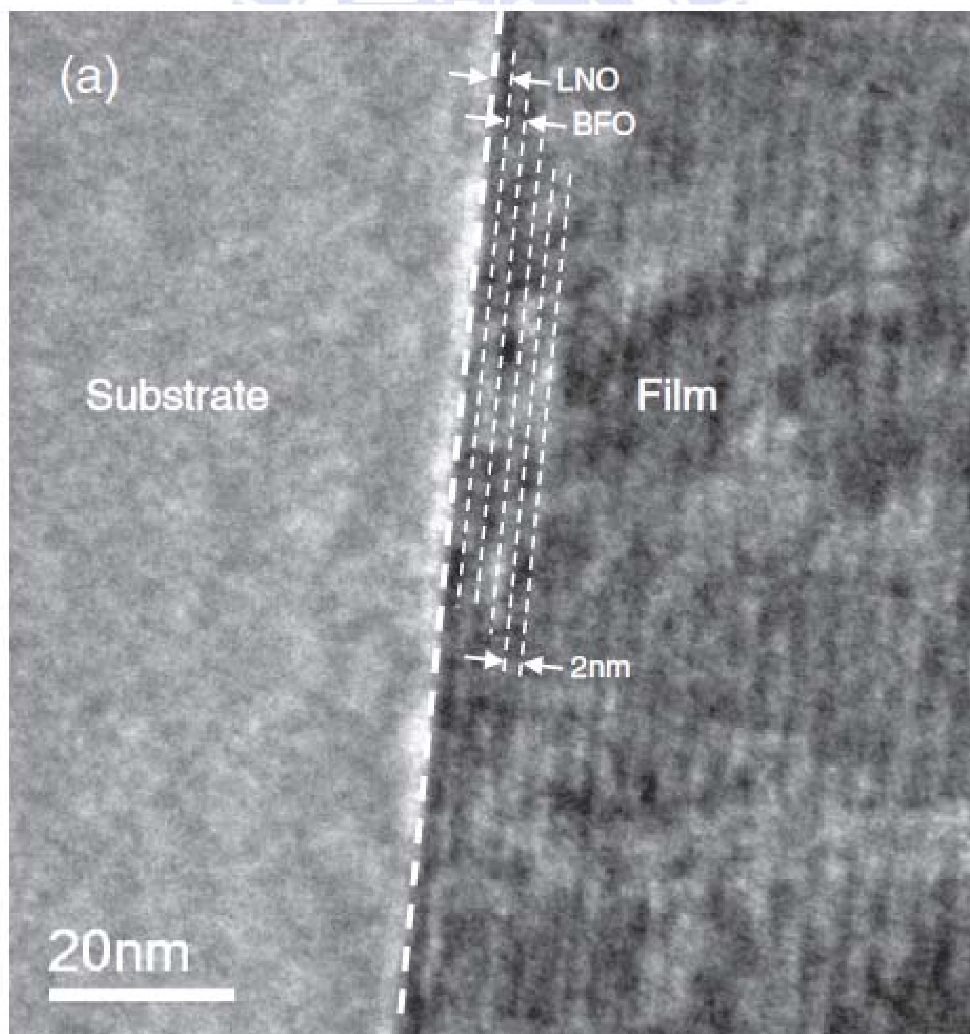

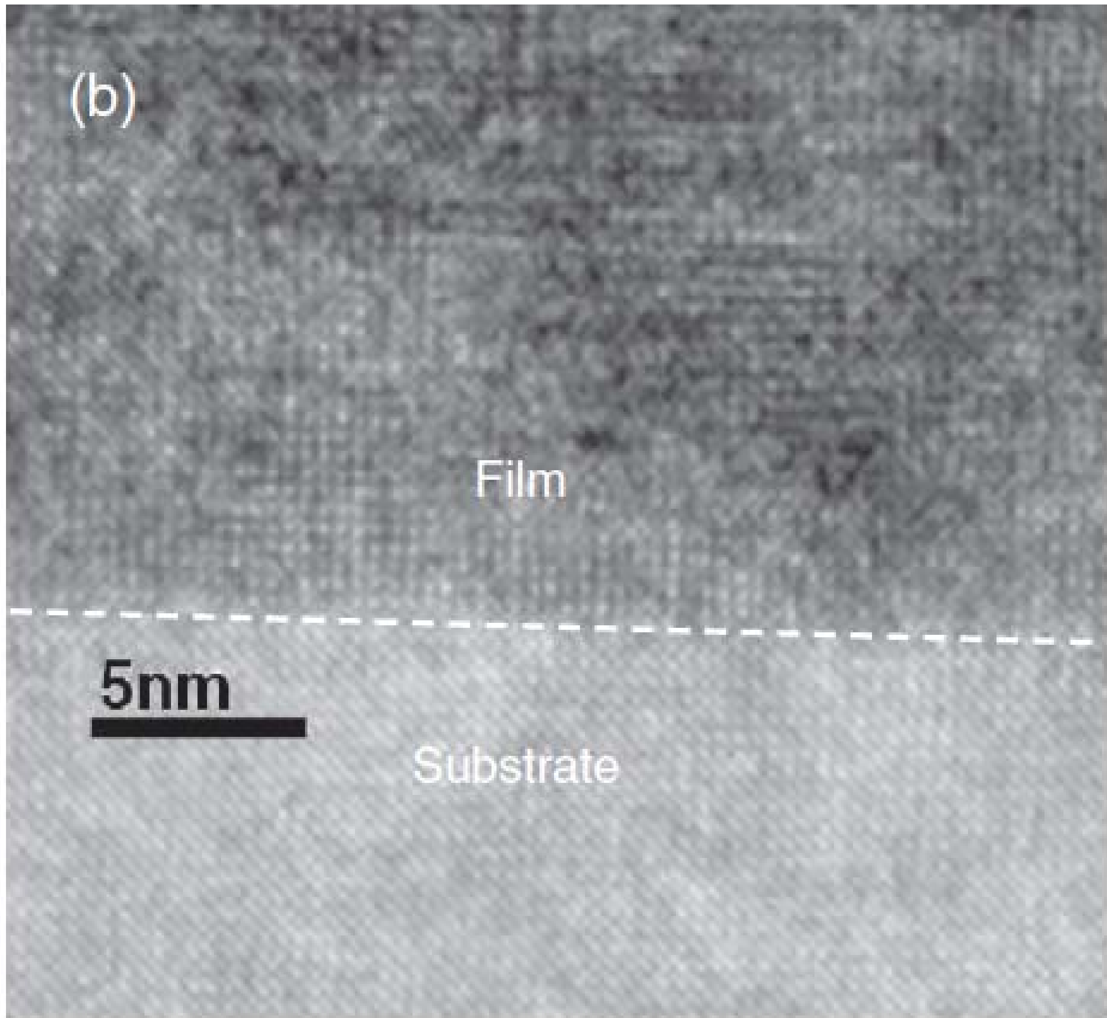

Figure 4.2.5 HRTEM cross-sectional images of the BFO/LNO superlattice on the (001) $SrTiO_3$ substrate deposited at 660 °C; (a) large scale image, and (b) image of the interface regions between individual layers and between film and substrate.

Figures 4.2.1 and 4.2.2 show an extra peak (marked *) located at ***L***=1.872 and ***H***=1.868 for superlattice thin films deposited with the substrate temperature greater than 710 °C, which we attribute to the formation of the NiO phase due to protracted deposition at high temperature. This NiO compound is readily formed during decomposition of the LNO film heated for a long time at a high temperature of deposition [128]. To confirm the formation of this NiO phase, we measured the DAFS pattern for film deposited at 710 °C. DAFS is the X-ray spectrometric technique that combines a sensitivity to long-range order of X-ray diffraction and a sensitivity to short-range order of X-ray-absorption fine structure [112]. Figure 4.2.6 shows the DAFS result of the Ni K-edge and La L1-edge for the (002) superlattice diffraction peak and the extra peak shown in Figure 4.2.1 (marked *) for film deposited at 710 °C. These results clearly show a strong Ni absorption signal at 8.345 keV with no La absorption signal on the extra diffraction peak, whereas both Ni and La absorption signals exist on the (002) superlattice diffraction peak. According to this evidence from DAFS, the extra peak indicates a NiO phase. The superlattice structure became gradually degraded through the formation of the NiO phase for a film deposited at temperature ≧710 °C, and was destroyed at 810 °C. The modulation length of the superlattice and the thickness of the LNO layer altered slightly because of the formation of the NiO phase. The main peak of the superlattice has therefore an unsystematic shift for film deposited at high temperature.

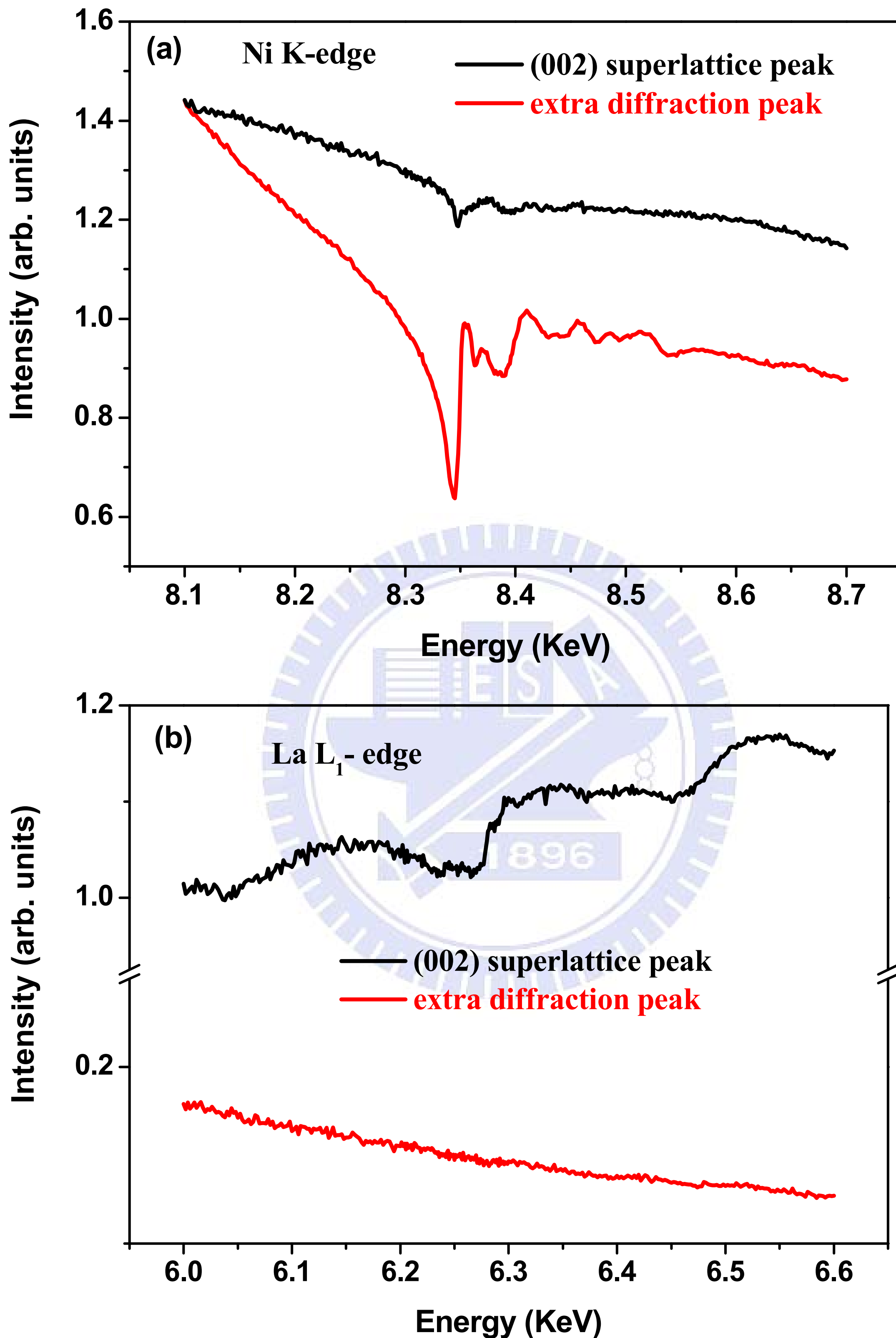

Figure 4.2.6 DAFS result of the (002) superlattice diffraction peak and the extra peak as shown in figure 4.2.1 (marked *) for film deposited at 710 °C (a) Ni K-edge, and (b) La L1-edge.

The BFO and LNO films are described as having a pseudo-cubic structure, with bulk lattice parameters 0.3962 nm for BFO and 0.3861 nm for LNO. In this superlattice system, the BFO sublayer is in a biaxially compressive state, whereas the LNO sublayer is in a biaxially tensile state. These heteroepitaxial sublayers are hence characterized by either being strongly strained or containing many misfitted dislocations with a modulation length larger than a critical value. The critical thickness for the misfitted dislocations is estimated according to a model proposed by Matthews and Blakeslee [129] as

$$h_c = \frac{b}{4\pi f(1+\upsilon)}\left[\ln\left(\frac{h_c}{b}\right)+1\right],$$

in which h_c is the critical thickness, b is the magnitude of the Burgers vector of the dislocations, ν is the Poisson ratio, and f is the misfit between the least strained BFO/LNO bilayer and the STO substrate. The calculated critical thickness of the BFO/LNO superlattice was ~15 nm. The designed modulation length of the prepared superlattices (t_{BFO} + t_{LNO}= 4 nm) is within the theoretically estimated length. The total thickness of films, about 120 nm, was much greater than the critical value of the thickness as BFO/LNO superlattice films; this condition is one factor that leds to strain release. Both the sublayer and the total thickness were factors that contribute to the results of the partial strain effect in the superlattice structure.

The in-plane lattice parameter of BFO is determined directly from a crystal-truncation-rod (200) radial scan [130, 131]. Although the out-of-plane lattice parameter of the BFO layer is directly indeterminated from the (0 0 2) radial scan spectra shown in Figure 4.2.1, we evaluated the parameter through the elastic relation involving the strain normal to the interface in the cubic structure [132, 133]. The in-plane compressive strain of the BFO layer is defined

as $(\boldsymbol{a}_{BFO}-\boldsymbol{a}_{bulk\text{-}BFO})/\boldsymbol{a}_{bulk\text{-}BFO}$, in which $\boldsymbol{a}_{BFO}$ is the lattice parameter of the strained BFO layer that is obtained from the measured inplane lattice parameter of the superlattice and $\boldsymbol{a}_{bulk\text{-}BFO}$ is the bulk lattice parameter of unstrained BFO. Based on this derived lattice parameter, the evaluated in-plane and out-of-plane strains of BFO layers are shown in Figure 4.2.7. Deposition at a higher temperature results also in a clearly larger in-plane compressive strain of the BFO sublayers in the superlattice for films deposited at 560 – 660 °C. An in-plane lattice parameter 0.3905 nm is necessary for the fully strained pseudomorphic growth of BFO/LNO superlattices on the STO substrate. The lattice mismatch between BFO-LNO bilayer is ~2.5 % of the in-plane lattice parameter. A fully strained pseudomorphic growth of each layer thus does not occur in the superlattice during deposition, even though the thickness of individual BFO and LNO layers is less than the critical thickness [130, 134]. The BFO/LNO superlattice films reveal a partial strain relaxation, and a not fully strained state for all deposition temperatures, as shown in Figure 4.2.7.

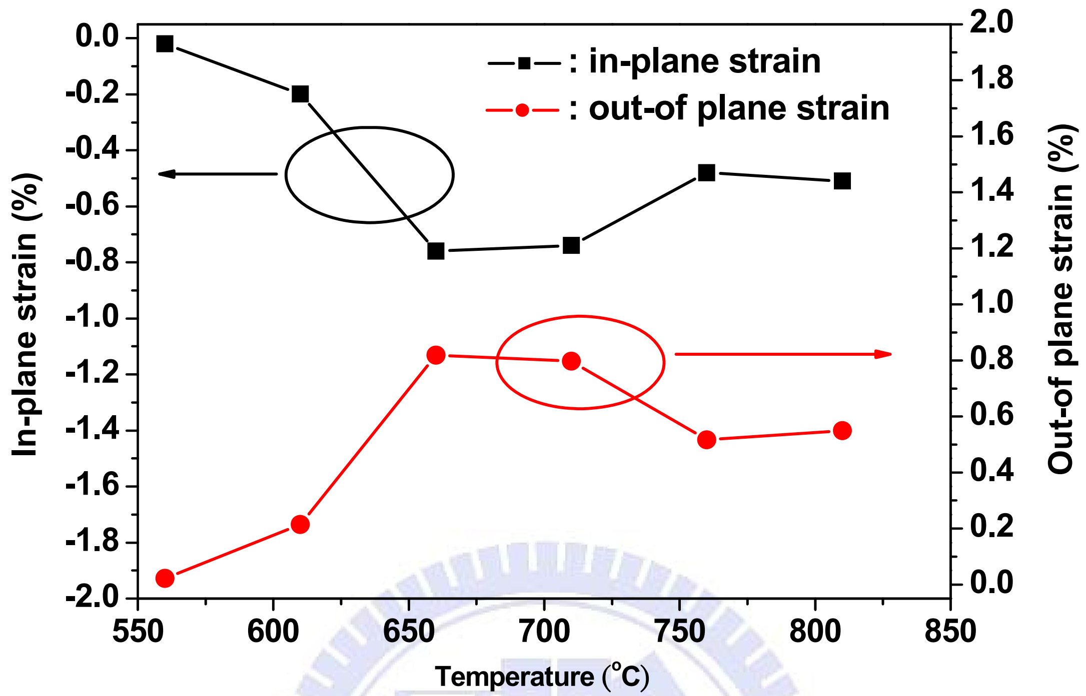

Figure 4.2.7 In-plane compressive strain and out-of plane tensile strain of the BFO layer as a function of deposition temperature.

Figure 4.2.8 shows the full width at half maximum (FWHM) of these in-plane rocking curves of BFO/LNO superlattice films deposited at various temperatures. The FWHM of the films increased greatly for the deposition temperature above 710 °C. The narrower is the FWHM, the better is the crystalline quality. The best crystal quality of the superlattice was shown at deposition temperature 660 °C, which can be the most suitable condition for growth of a BFO/LNO superlattice.

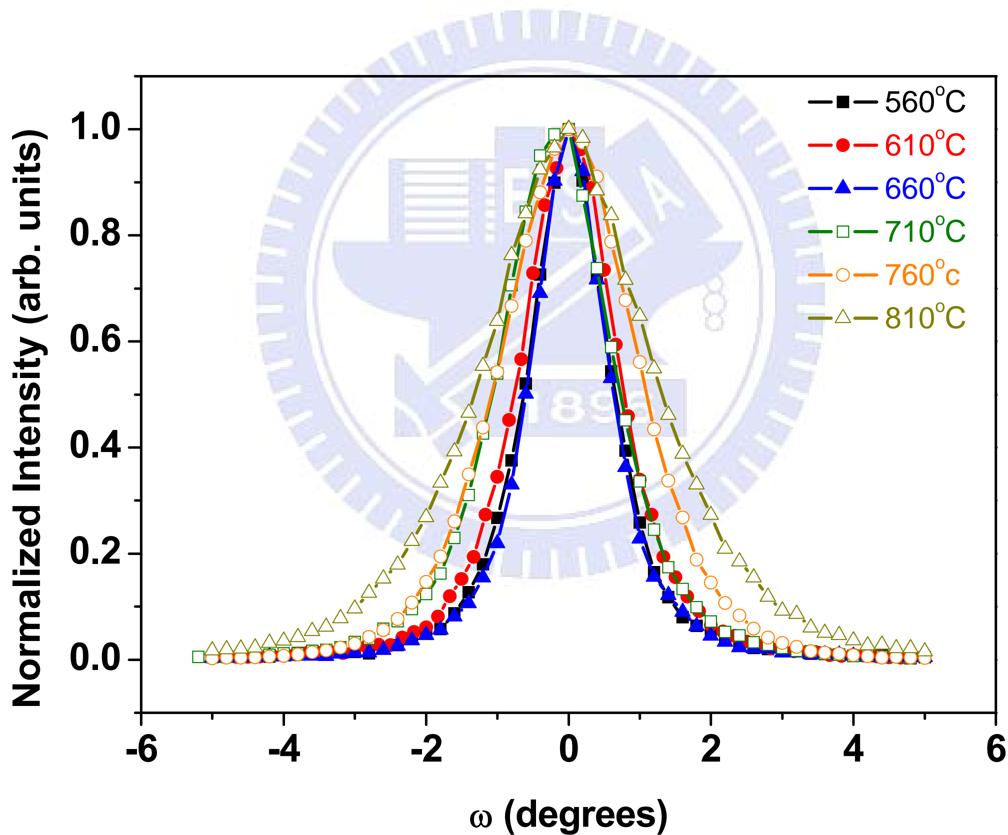

Figure 4.2.8 Rocking curves of the in-plane (200) main peak of BFO/LNO superlattice films deposited at various temperatures.

Figure 4.2.9 presents reflectivity curves of BFO/LNO superlattice films deposited at various substrate temperatures, and their best-fitted results. The presence of clear oscillations indicates that both the surface and the interface correlate well with each other and are smooth enough to produce the oscillations. Both the superlattice peaks and the Kiessig oscillations, which are well pronounced, reveal the presence of a well ordered layer structure of a superlattice, providing evidence for the vertically periodic modulation of the composition. To evaluate the physical parameters of the superlattice, we used a simulation of the specular reflectivity on the recursive formalism of Parratt [103]. We fitted the reflectivity data according to Ref. 104 [104] to determine the physical parameters of the superlattice, including roughness, thickness, and density. This program calculates the reflectivity of the material using the dynamic Fresnel equations for multilayer reflectivity, taking into account the absorption, instrumental resolution, interface roughness and abruptness, and the sample curvature.

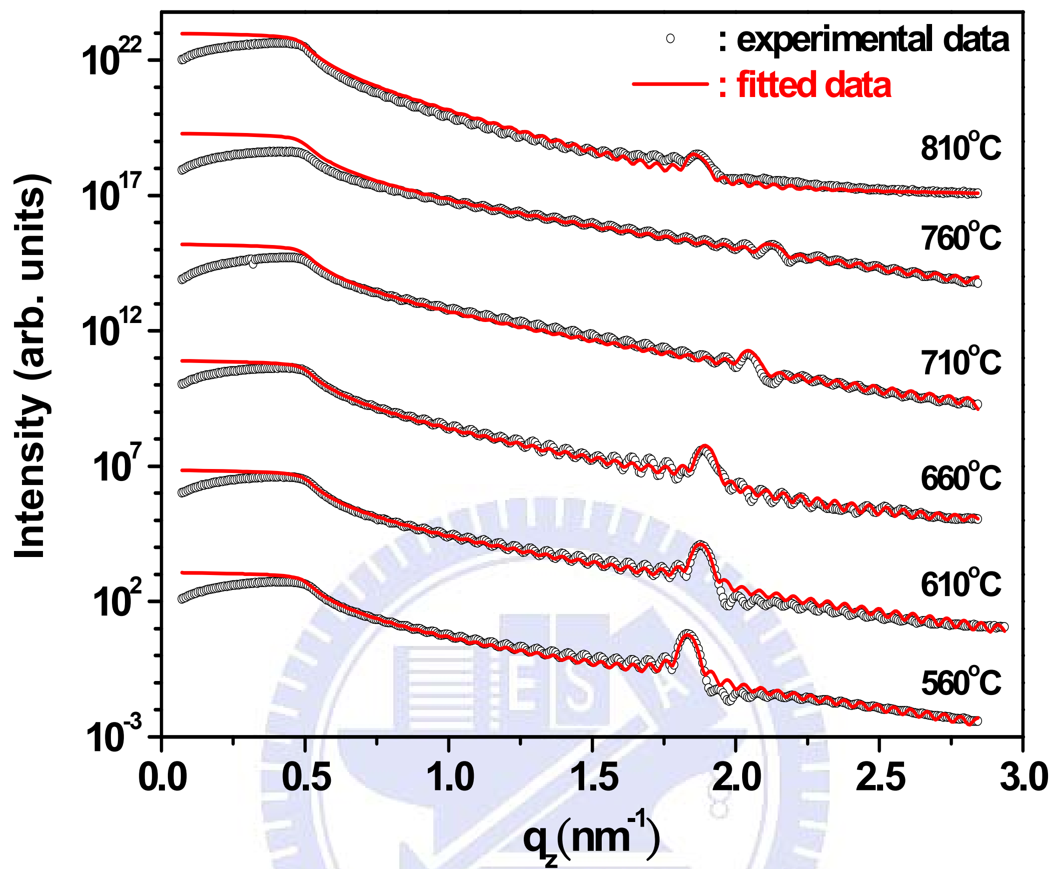

Figure 4.2.9 Reflectivity curves of BFO/LNO superlattice films deposited at various substrate temperatures and their best-fit results (solid line) as a function of momentum transfer.

Table 4.2.1 shows the best-fitted results of the physical parameters of each thin-film layer, which indicate that the density of the BFO sublayer was less than the bulk value and decreases with increasing temperature, whereas for the LNO sublayer the density was slightly less than the bulk value. A Bi atom escapes readily from the thin film at the high deposition temperature [135]. The density of BFO was much less than the bulk density; this condition likely reflects an increased density of defects that inevitably occur during the deposition at high temperature. We found also that the thickness of the sublayer decreased with increasing substrate temperature, except the film deposited at 810 °C, indicating a growth rate inversely proportional to temperature. The thickness of the LNO sublayer decreased with increasing deposition temperature; as the kinetic energy increases with increasing temperature, the effect of re-sputtering was much more obvious, leading to the decreased thickness of the sublayer.

At a high deposition temperature many vacancies are produced through the escape of Bi; the density of BFO decreased with increasing temperature. The fitted result shows not only that the surface and interface roughness increased with increasing deposition temperature but also that the interface roughness increased much for deposition at substrate temperature greater than 760 °C. The reflectivity curve also that the lower is the deposition temperature, the more clearly present are the superlattice peaks and the Kiessig fringes. Hence, the lower is the deposition temperature, the smoother is the surface and the less rough is the interface, except film deposited at ≧710 °C.

Table 4.2.1 Parameters obtained from best-fit results of reflectivity curves of BFO/LNO superlattice films deposited on the Nb-doped STO substrate with varied deposition temperature. The surface roughness determined from AFM measurements is listed in the last column for comparison. The relative standard deviations of the fitted data are for thickness ≦2.5%, density ≦3% and roughness ≦6%. The thickness of the $SrTiO_3$ substrate is set as infinite and the bulk density is 5.118 g cm^{-3}. The bulk density of BFO is 8.366 g cm^{-3}, and that of LNO is 7.086 g cm^{-3}.

deposition temperature / °C	fitted thickness / nm		fitted density / g-cm^{-3}		fitted roughness / nm			AFM / nm
	t_{LNO}	t_{BFO}	ρ_{LNO}	ρ_{BFO}	$\sigma_{LNO/sub}$	$\sigma_{interface}$	$\sigma_{surface}$	$\sigma_{surface}$
560	1.57	2.00	6.59	7.69	0.40	0.41	0.61	1.86
610	1.48	1.99	6.73	7.61	0.40	0.46	0.70	2.15
660	1.43	1.98	6.80	7.53	0.40	0.49	0.82	2.16
710	1.15	1.99	6.80	7.28	0.40	0.60	0.75	0.50
760	1.23	1.80	6.67	7.11	0.39	1.18	0.62	0.26
810	1.60	1.89	6.45	7.19	0.39	1.21	1.20	3.95

To confirm the X-ray reflectivity results of the surface roughness, we examined the surface roughness of the superlattice films using AFM. From observations conducted in a contact mode on area 1 μm × 1 μm, we calculated the root-mean-square (RMS) magnitude of surface roughness. The surface morphology of BFO/LNO superlattice films deposited at various substrate temperatures, as examined with the AFM, is shown in Figure 4.2.10. The AFM images show that the film surface is free of cracks, but exhibits surface/film features of three types—island-like for film deposited at ≦660 °C, nearly structureless or featureless for 710 – 760 °C, and platelet-like for 810 °C. For comparison, the surface roughness evaluated from AFM images is listed in Table 4.2.1. The surface roughness of the superlattice films shows the same tendency of increasing surface roughness with increasing deposition temperature for films deposited up to 660 °C. The results show a tendency consistent with the XRR fitted results.

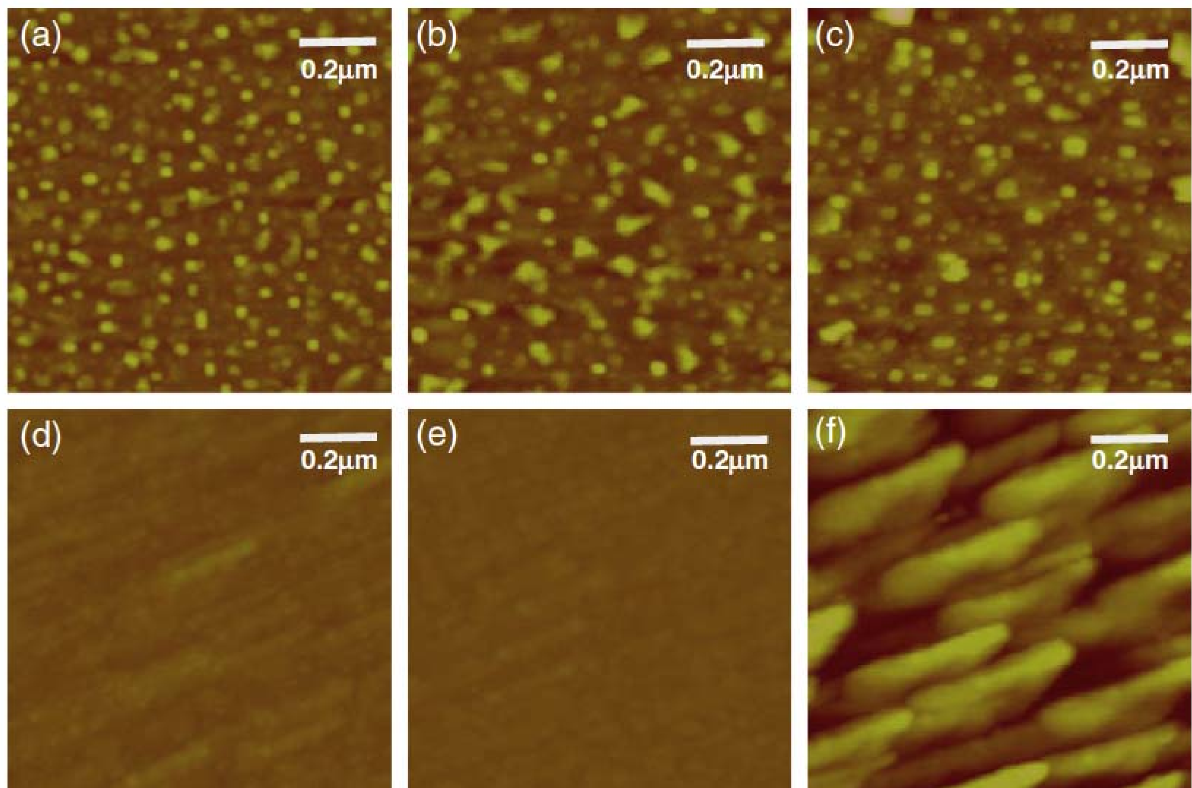

Figure 4.2.10 AFM images of BFO/LNO superlattice films deposited at substrate temperatures/°C: (a) 560, (b) 610, (c) 660, (d) 710, (e) 760, and (f) 810.

4.2.2 Electrical properties of the BFO/LNO superlattice

Figure 4.2.11 shows the polarization–electric field (*P-E*) hysteresis loop of the BFO/LNO superlattice deposited at various substrate temperatures. Hysteresis loops with the largest remanent polarizations (2 P_r) near 160 μC cm^{-2} were observed for superlattice films deposited at 660 °C, although the exact P_r value was difficult to determine because there still existed a large component of leakage current, even with an epitaxial thin film of high quality. In a ferroelectric or conductive superlattice system, i.e., BFO/LNO superlattice, the intervening metallic layer increases the leakage current. The remanent polarization increased with increasing deposition temperature for films deposited up to 660 °C, and then decreased with further increasing temperature. As illustrated in Figure 4.2.7, the BFO sublayers in the superlattices exhibit an increased compressive strain, or a larger lattice distortion, that much elongates the unit cells along the electric field in the superlattice structure with increasing deposition temperature in the range of 560–660 °C. This result clearly reveals that an effective manipulation of strain in BFO sublayers in a superlattice structure with alternating insertion of LNO sublayers can greatly enhance the ferroelectric properties of the BFO sublayers. The fitted result of the X-ray reflectivity curve shows that the interfacial roughness of superlattice films deposited above 760 °C is much larger than at other temperatures. Although these superlattice films have greater tensile stress along the ***c***-axis, they have also narrower effective BFO layers. The greatly decreased remanent polarization of films deposited above 760 °C might be attributed to the formation of the NiO phase and the poor interface structure in the superlattice system. The value of remanent polarization (2 P_r) of the effective BFO layer, 2 P_r ~160 μC cm^{-2}, obtained from Figure 4.2.8 is twice as large as that, 2 P_r ~70 μC cm^{-2}, for the

single layer BFO film of thickness 60 nm prepared under the same sputtering conditions at 660 °C.

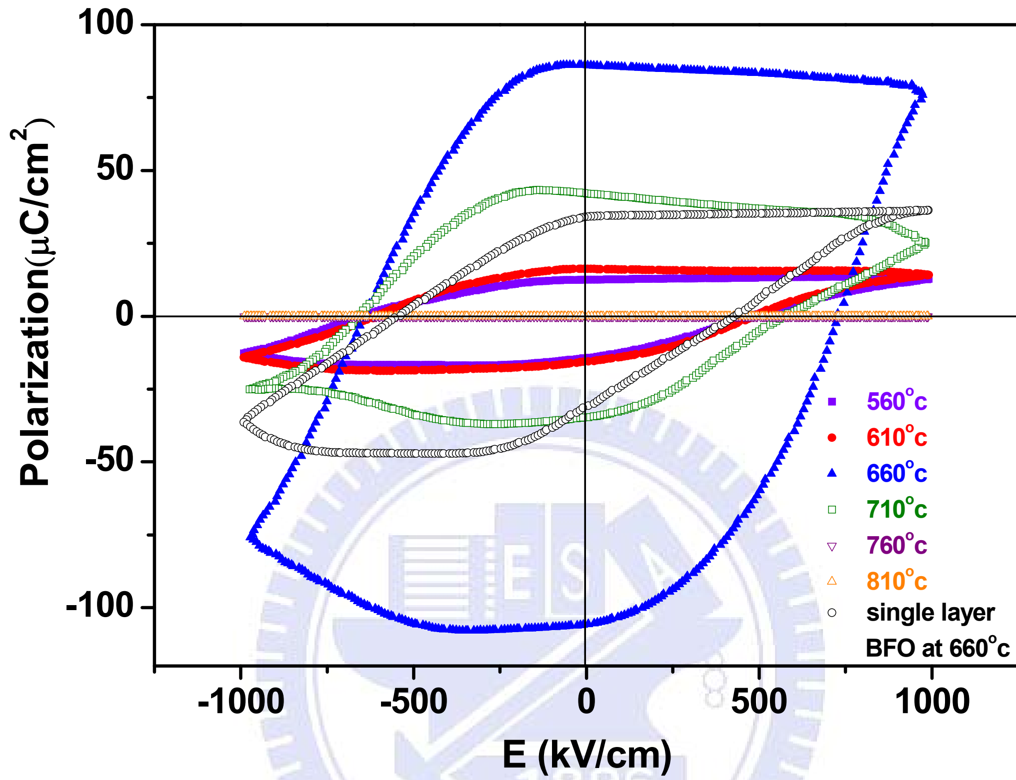

Figure 4.2.11 P-E hysteresis loops of BFO/LNO superlattice deposited at various substrate temperatures.

Figure 4.2.12 shows the *J-E* curve of BFO/LNO superlattice films with various deposition temperature, which indicates large leakage current densities in this superlattice system for all deposition temperatures, relative to a single BFO layer film of thickness 180 nm [25] or another BFO/STO superlattice system with the BFO layers of total thickness 200 nm prepared with the PLD technique [136]. In the BFO/LNO superlattice system, a metallic layer between leads increases the leakage current. These leakage current densities greatly increased for film deposited at ≧710 °C, which seems consistent with the tendency of the crystalline quality of the films and the formation of NiO phase.

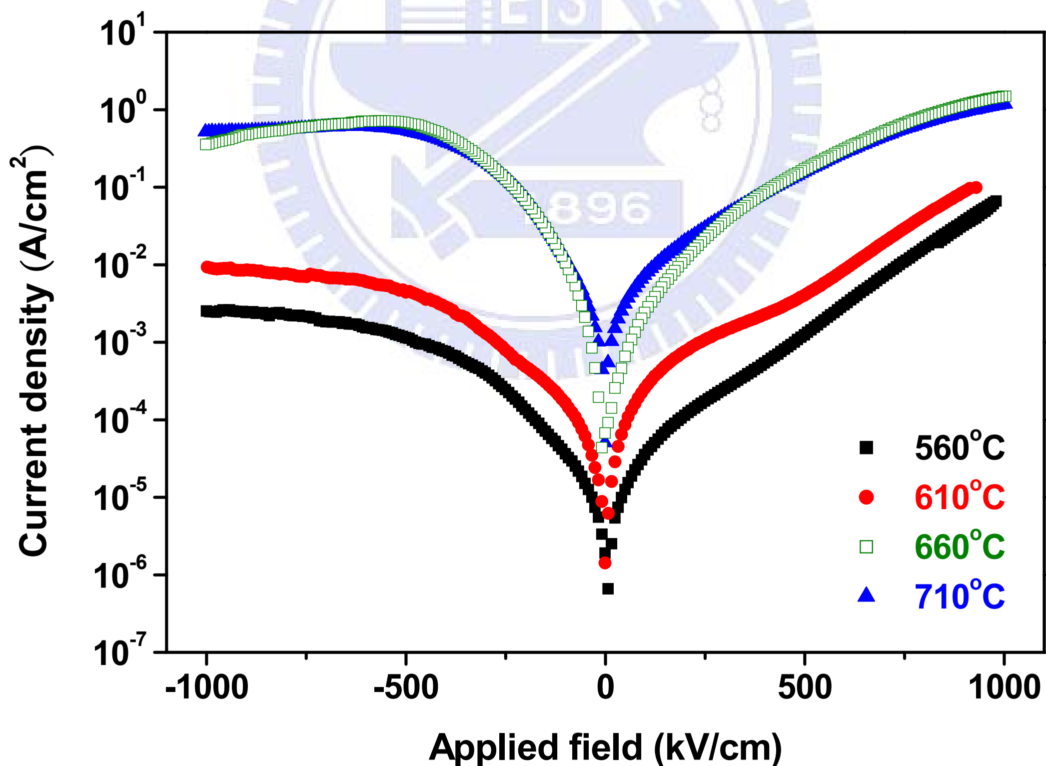

Figure 4.2.12 J-E curve of BFO/LNO superlattice films deposited at 560 – 710 °C.

4.3 Sublayer thickness and leakage effect of the BFO/LNO superlattice

The growth condition of the BFO/LNO superlattice with satisfactory crystal structure and ferroelectric properties was optimized in previous work. The sublayer thickness is an important issue of the superlattice structure, and the leakage property is a dominant problem of the hysteresis loop; those issues were studied in this work.

4.3.1 Crystal structure of the BFO/LNO superlattice with varied sublayer thickness

Figure 4.3.1, obtained from an eight-circle X-ray diffractometer and a high-resolution synchrotron source with a radial scan along direction (00***L***) of the BFO/LNO superlattice films, shows the crystalline quality of the superlattice structure. The intense and sharp peak centered at ***L***=2 is the STO (002) Bragg reflection from the substrate. The main peak (marked with arrows in Figure 4.3.1) and well defined satellite peaks on both sides of the main peaks indicate the great crystalline quality of the BFO/LNO artificial superlattice structure formed with RF-magnetron sputtering. Expanded views of the fitted curve (solid line), using both symmetric and exponential composition profiles and experimental data (open circles) of BFO/LNO superlattice films with sublayers of thicknesses 3.6 and 8.5 nm, in the inset of Figure 4.3.1 indicate the position of the reflection of the satellite peak (marked with an arrow). Overall, both assumptions yielded satisfactory agreement with the experimental data; some discrepancy of the background intensity near the substrate peak in the composition modulation shape is indicated by the satellite intensities. The superlattice exhibits satellite peaks that allowed us to deduce the super-period of the superlattice ($\boldsymbol{\Lambda}_{WAXRD}$) according to the formula [137]

$$\Lambda_{WAXRD} = \frac{\lambda}{2(\sin\theta_n - \sin\theta_{n-1})},$$

in which λ is the X-ray wavelength and θ_n and θ_{n-1} are the angular positions of two successive satellite peaks.

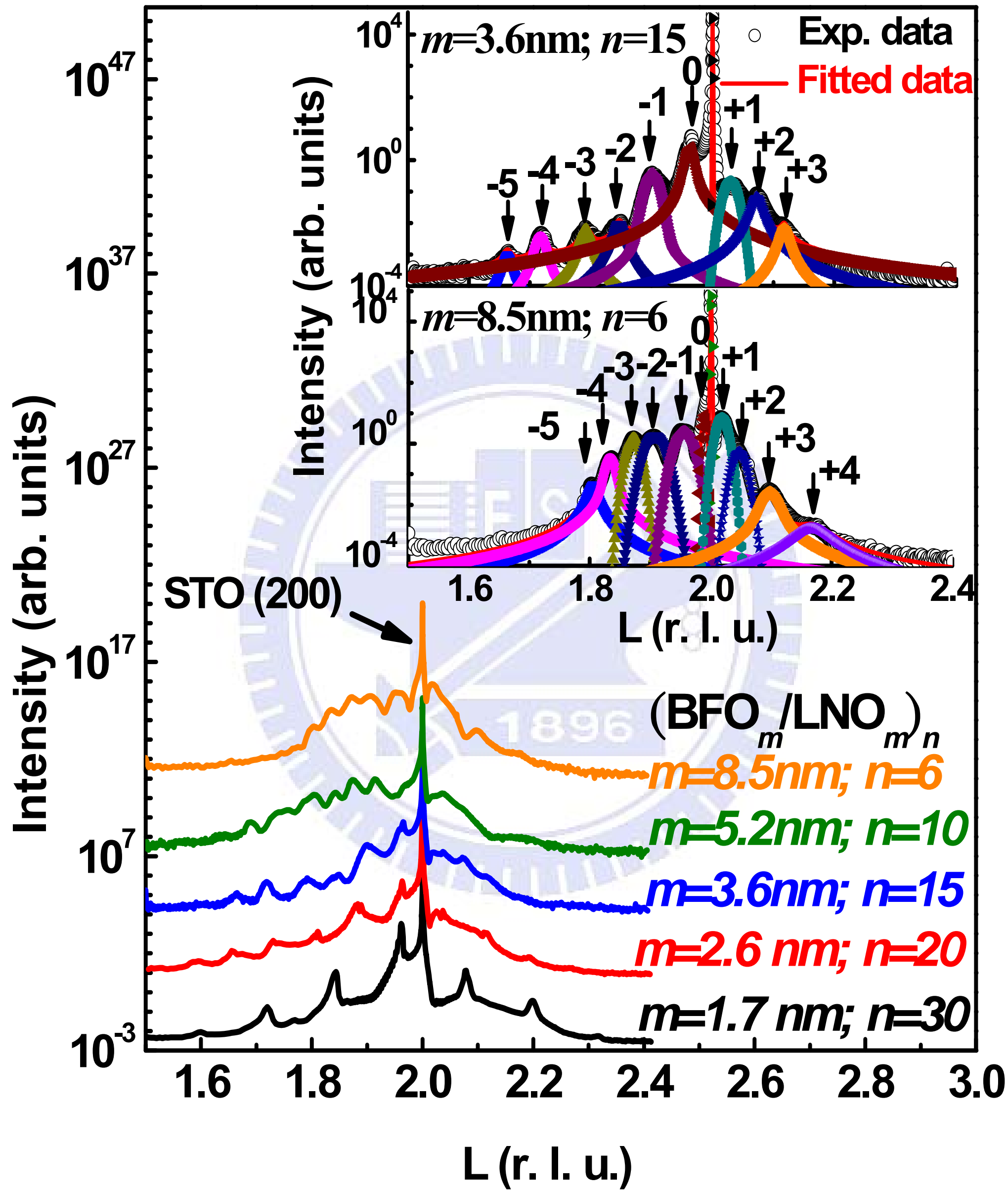

Figure 4.3.1 Intensity distribution of the (002) radial scan for the BFO/LNO superlattice with varied thickness of sublayer and periods. The inset shows the best fits (solid line) for the experimental XRD patterns for BFO/LNO superlattices at thicknesses 3.6 and 8.5 nm.

The period of the superlattice films obtained from the oscillations of the (002) radial scan shown in Table 4.3.1 agrees with the measurement result of the X-ray reflectivity

Table 4.3.1 Thickness parameters of the BFO/LNO superlattice obtained from the results of X-ray diffraction, X-ray reflectivity and SIMS.

Nominal sample	**Λ_{WAXRD} / nm**		**Fitted thickness by X-ray reflectivity / nm**			**Total thickness (SIMS) / nm**
	Modulation length $t_{BFO}+t_{LNO}$	**Total thickness**	**t_{BFO}**	**t_{LNO}**	**Total thickness**	
$(B_{1.7}/L_{1.7})_{30}$ / STO	**3.40 ± 0.17**	**102.0**	**1.70 ± 0.04**	**1.75 ± 0.04**	**103.5**	
$(B_{2.6}/L_{2.6})_{20}$ / STO	**5.40 ± 0.27**	**108.0**	**2.60 ± 0.06**	**2.60 ± 0.06**	**104.0**	
$(B_{3.6}/L_{3.6})_{15}$ / STO	**7.20 ± 0.36**	**108.0**	**3.08 ± 0.07**	**4.00 ± 0.10**	**106.2**	
$(B_{5.2}/L_{5.2})_{10}$ / STO	**10.40 ± 0.52**	**104.0**	**5.30 ± 0.13**	**5.30 ± 0.13**	**106.0**	**104.0 ± 1**
$(B_{8.5}/L_{8.5})_{6}$ / STO	**17.50 ± 0.88**	**105.0**	**8.70 ± 0.21**	**8.70 ± 0.21**	**104.4**	**105.0 ± 1**

To verify the vertically periodic modulation obtained from the X-ray measurements, we examined the vertical composition profile of the BFO/LNO superlattices with SIMS. A SIMS depth profile of the $(BFO_{8.5}/LNO_{8.5})_6$ superlattice is shown in Figure 4.3.2. The variations in the signals of Bi, Fe, La, Ni, Sr, Ti and O are consistent with the designed period of six cycles of a BFO/LNO superlattice. The total thickness obtained from the SIMS is consistent with the calculated from the (002) radial scan and the X-ray reflectivity curve shown in Table 4.3.1.

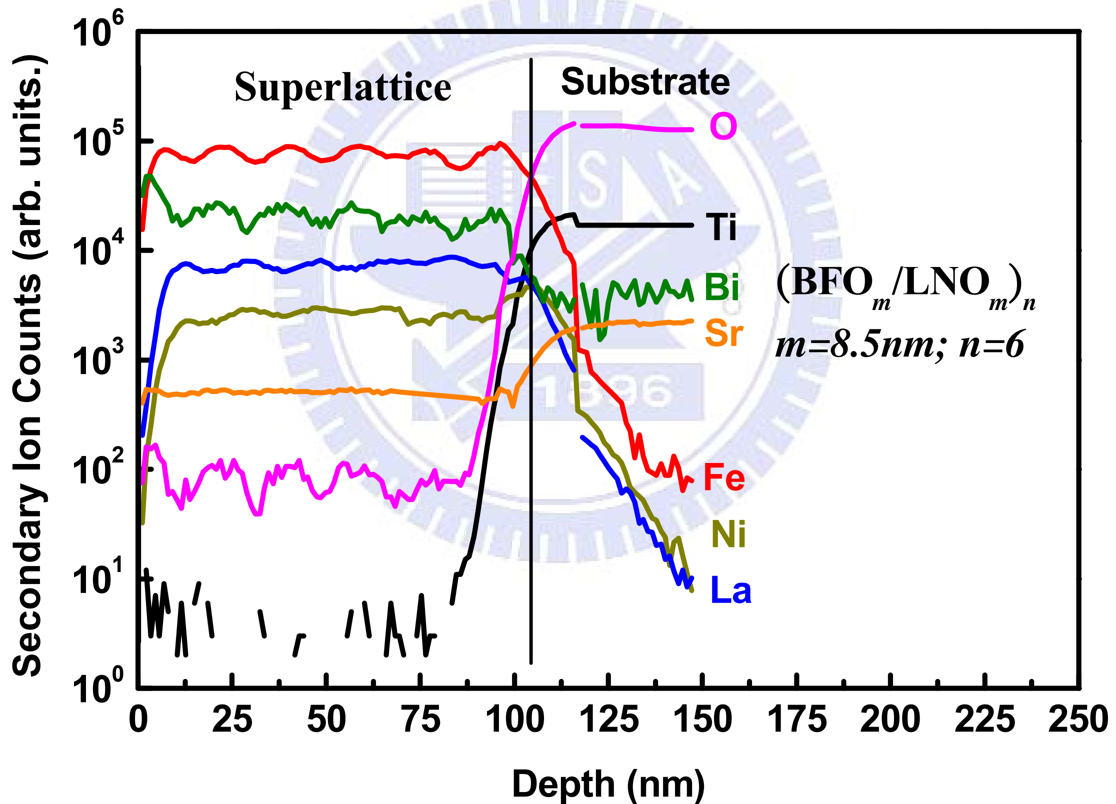

Figure 4.3.2 SIMS depth profile of the $(BFO_{8.5}/LNO_{8.5})_6$ superlattice film.

The epitaxial relation between the BFO and LNO layers in the superlattice was examined according to the orientation in plane with respect to the major axes of the STO (001) substrate. The distribution of the X-ray intensity of an in-plane radial scan of the BFO/LNO superlattice film is shown in Figure 4.3.3. The Bragg peak of the superlattice is shifted to a smaller *H* index and broadens rapidly with increasing thickness of the sublayer. The azimuthal diffraction patterns of the $(BFO_{1.7}/LNO_{1.7})_{30}$ superlattice in the vicinity of a surface peak and the substrate Bragg peak that clearly exhibits a four-fold symmetry with the same orientation appear in the inset of Figure 4.3.3. These results constitute evidence for strong epitaxial growth of the deposited layer on the substrate. No other signal is observed in the intervals between the four peaks, indicating a perfect alignment of *a* and *b* of the BFO and LNO unit cells along those of the STO substrate.

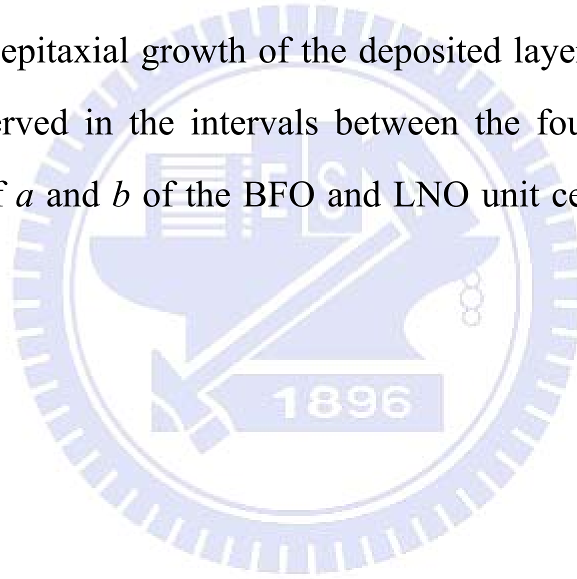

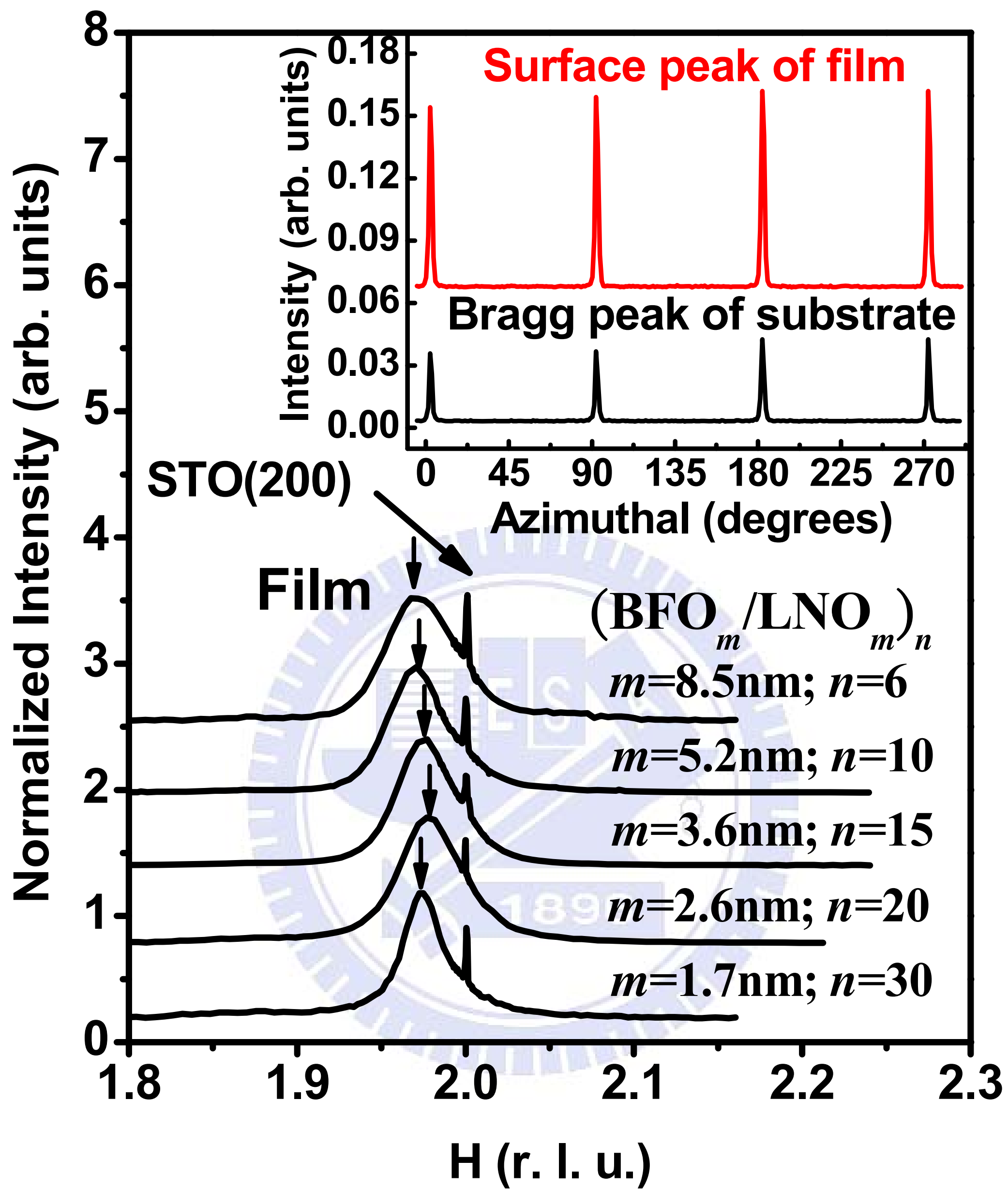

Figure 4.3.3 X-ray intensity of radial scans along the (200) in-plane Bragg line of BFO/LNO superlattice films deposited for various periods. An arrow marks the position of the superlattice main peak. The inset shows the azimuthal scan (Φ scan) of the surface peak and the substrate Bragg peak for the $(BFO_{1.7}/LNO_{1.7})_{30}$ superlattice film.

The lattice parameters of BFO and LNO are 0.3962 and 0.3861 nm, respectively. The BFO sublayer is in a biaxially compressive state whereas the LNO sublayer is in a biaxially tensile state in the superlattice system. The critical thickness for misfit dislocations, estimated according to a model proposed by Matthews and Blakeslee [129], of the BFO/LNO superlattice was ~15 nm. The designed modulation length ($\boldsymbol{t}_{BFO}+\boldsymbol{t}_{LNO}$) of the superlattices was from 3.4 nm to 17 nm. The lattice parameter of BFO in plane was determined directly from the (2 0 0) reflection [130, 131]. The compressive strain in plane is defined as ($\boldsymbol{a}_{BFO}-\boldsymbol{a}_{bulk-BFO}$)/$\boldsymbol{a}_{bulk-BFO}$, in which $\boldsymbol{a}_{BFO}$ is the lattice parameter of the strained BFO layer observed from the radial scan in plane of the superlattice and $\boldsymbol{a}_{bulk\text{-}BFO}$ is the lattice parameter of bulk BFO free of strain. Based on this derived lattice parameter, the strains evaluated in plane and out of plane of BFO layers are related with [138]

$$\varepsilon_{\perp} = -\frac{2\upsilon}{1-\upsilon}\varepsilon_{//},$$

in which ν is Poisson's ratio, $\boldsymbol{\varepsilon}_{\perp}$ is the strain for out-of-plane and $\varepsilon_{//}$ is the strain for in-plane, shown in Figure 4.3.4 (a). The thinner is the sublayer; the larger is the in-plane compressive strain of the BFO sublayers.

4.3.2 Electrical properties of the BFO/LNO superlattice with various sublayer thicknesses

Figure 4.3.4 (b) shows the *J–E* curve of BFO/LNO superlattice films with sublayers of various thicknesses, which indicates large leakage current densities in this superlattice system for all periods; the leakage current increases with increasing thickness of the sublayers. In an insulating or conductive superlattice system, i.e., the BFO/LNO superlattice, there is a metallic layer in between, which increases the leakage current. An asymmetric feature of *J–E* curves might be due to varied Schottky barrier heights of the top and bottom electrodes or the varied extent of interface defects on both sides [139, 140], which seem consistent with the tendency of the crystalline quality of the superlattice. The clearer diffraction peaks and satellite lines, the narrower diffraction in plane and the smaller mosaic structure of the film decrease the probability of leakage from the top electrode to the bottom electrode.

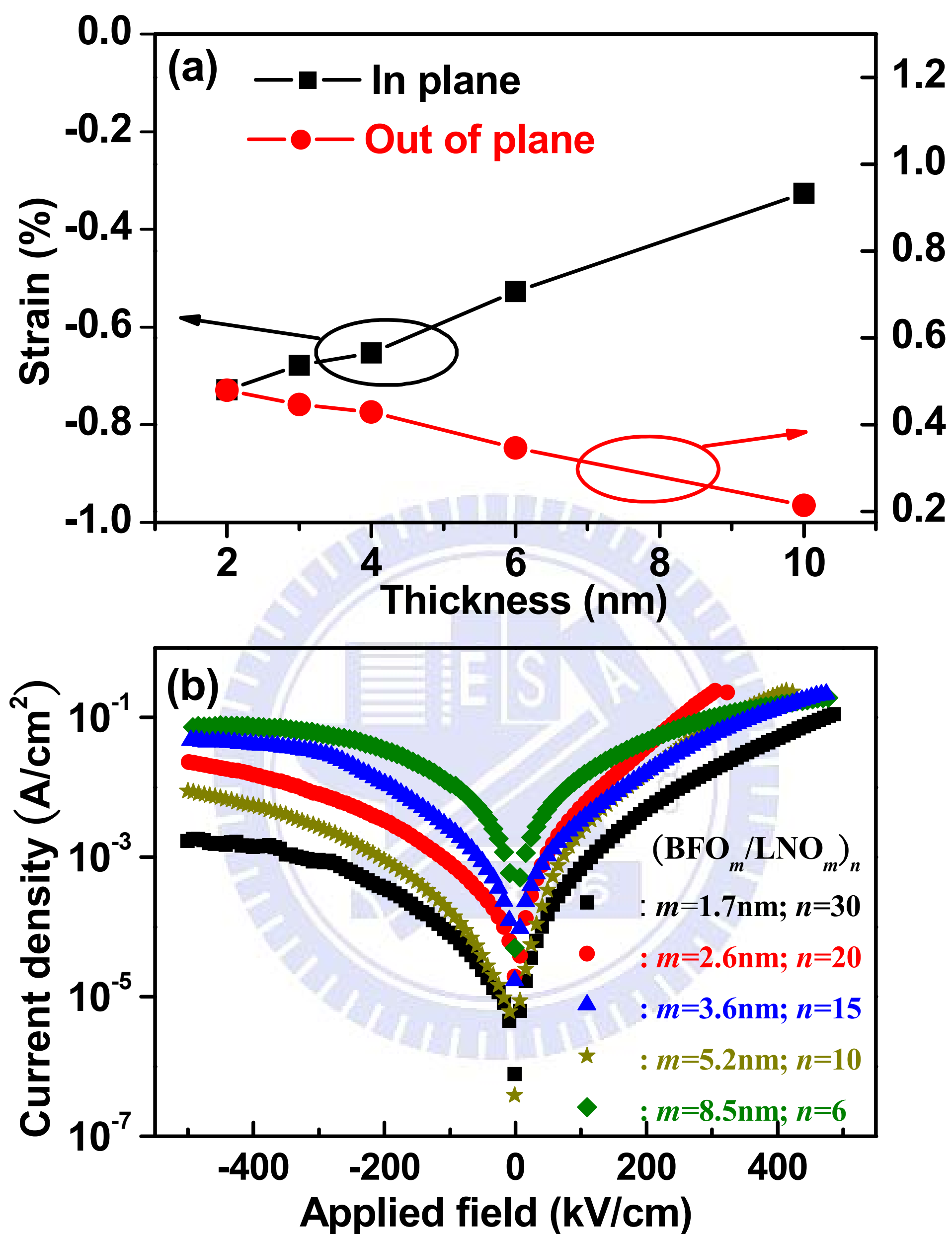

Figure 4.3.4 Strain dependent and J–E curve of BFO/LNO superlattice films with varied sublayer thickness (a) in-plane strain and out-of-plan strain, and (b) the **J–E** curve.

The ferroelectric properties of the BFO/LNO superlattice at thicknesses 1.7, 3.6 and 8.5 nm, and single-layer BFO film (thickness 60 nm), of the hysteresis loop of the polarization–electric field (*P*–*E*) are shown in Figure 4.3.5. *P*–*E* hysteresis loops of BFO/LNO measured with probing frequencies 0.5 – 5 kHz at 25 °C show that both remanent polarization P_r and coercive field E_C depend strongly on frequency. Hysteresis loops, with the largest remanent polarization (2 P_r) of 160 μC cm^{-2}, were observed for $(BFO_{8.5}/LNO_{8.5})_6$ measured at 5 kHz. In the loops measured under 1 kHz, the contribution from the leakage is distinctly observable, as a result of which both the rounded shape and the remanent polarization increase; at frequency 2 kHz or greater, the contribution from the leakage was eliminated, and well saturated loops were observed. Despite the small dc leakage, the *P*–*E* loop was dominated by other effects of the extrinsic space charge, which might be due to the presence of charged interface or defects or misfit dislocations formed through strain relaxation at the interface [141]. The poor ferroelectric nature of the BFO film can hence be attributed to the presence of mobile charge carriers (generated electrons and oxygen vacancies) at large concentrations [142].

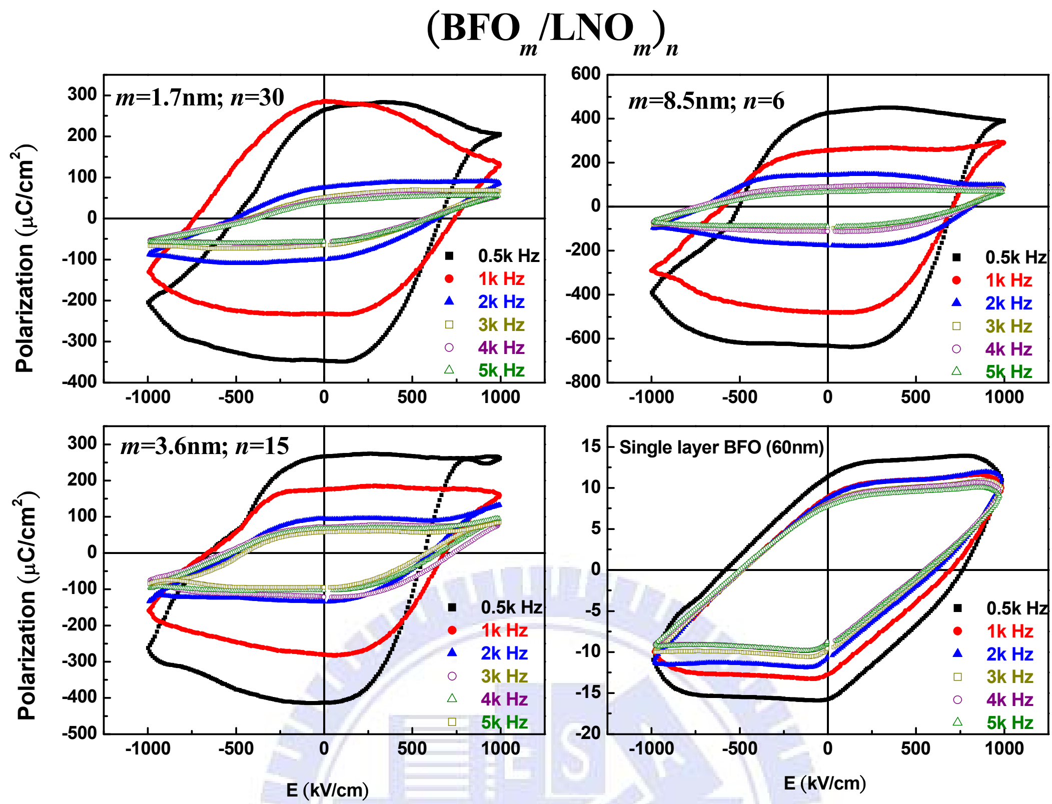

Figure 4.3.5 P–E hysteresis loops of a BFO/LNO superlattice at thicknesses 1.7, 3.6 and 8.5 nm of sublayers and single-layer BFO thin film (thickness 60 nm).

Figure 4.3.6 (a) displays the variation with frequency of the polarization value ($2P_r$); at small probing frequencies; these mobile free charges contribute to the total polarization. The leakage is attributed to the presence of oxygen vacancies, which increase the amount of free carriers, leading to a degradation of the ferroelectric properties [142]. The effect of the leakage current was much decreased on increasing the frequency of measurement; the polarization approached a saturation value at all sublayer thicknesses as shown in the Figure. From the result of polarization, an effective strain manipulation of BFO sublayers in the superlattice structure by LNO sublayers can enhance the ferroelectric properties of the BFO sublayers. The interface was an issue of the ferroelectric property: the thinner is the sublayer, the greater is the extent of the interface in the superlattice; imperfections at the interface, such as the formation of undesirable phases or electronic trapping states, seriously degrade the performance of the ferroelectric property [143]. For the same total thickness, the superlattice films of smaller sublayer thickness have more periods, and more interfaces result in a decreased effective thickness. The superlattice films that have a thicker sublayer with diminished interface region therefore exhibited a larger remanent polarization. The value of remanent polarization ($2P_r$) of the BFO layer, $2P_r \sim 160$ μC cm^{-2}, obtained from Figure 4.3.6 (a) is eight times that, $2P_r \sim 20$ μC cm^{-2}, for the single-layer BFO thin film (60 nm) prepared under the same sputtering conditions at 660 °C and measured at 5 kHz. To confirm the polarization of the superlattice, we performed a PUPD test with pulse width 0.25 ms and delay time of 1000 ms. This pulsed measurement demonstrates that the measured polarization switching is an intrinsic property of the superlattice, and separate from the leakage property [4]. The results of the PUPD test are shown in Figure 4.3.6(b); the remanent polarization obtained from the PUPD test was

smaller than that from the hysteresis loops but shows a tendency the same as with the result of the *P–E* loop, and likewise with the strain effect and the periods of the superlattice.

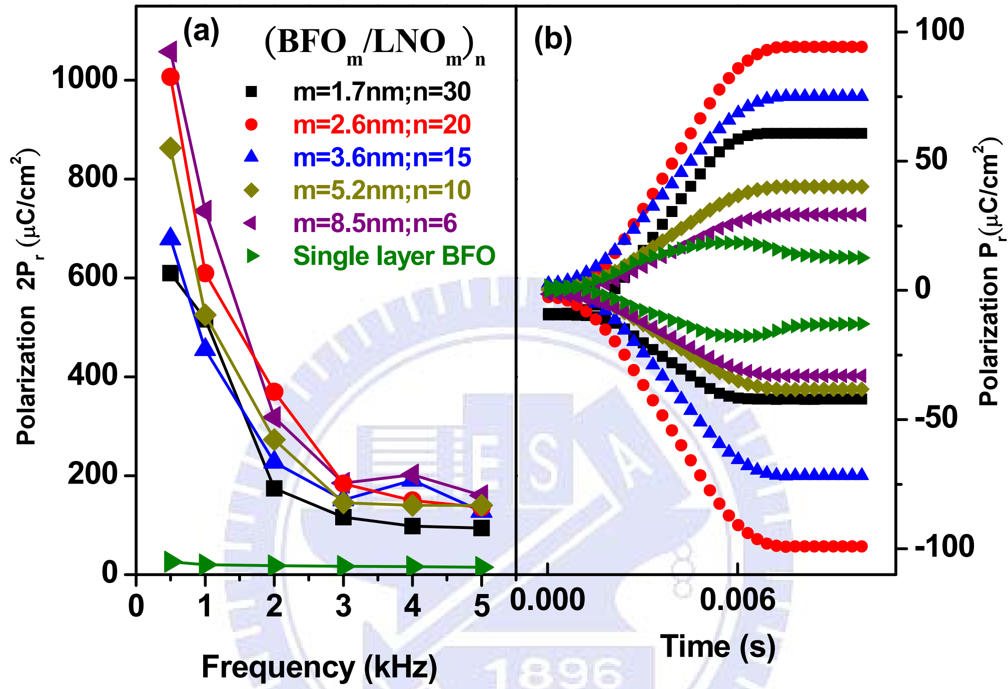

Figure 4.3.6 Polarization measurements for all sublayer thicknesses and single-layer BFO (a) polarization value (2**P**r) at varied frequencies from **P–E** hysteresis loops, and (b) the remanent polarization obtained from the PUPD test.

4.4 Growth of ultra-thin undoubted BFO films by atomic layer deposition.

The epitaxial BFO thin film grown with RF-sputtering show great ferroelectric properties, but the large leakage current still existed in the BFO thin film, which is a major concern.

4.4.1 Crystal structure and composition of ultra-thin BFO films.

Highly (001)-oriented BFO ultra-thin films with total thickness less than 10 nm were deposited on Si (001) substrates with ALD and a LNO buffer layer. The deposition rate of BFO thin films was determined by XRR as a function of growth temperature shown in Figure 4.4.1. The rate of BFO increases with substrate temperate, attaining a maximum value at 500 ^{o}C and decreasing again on further increased temperature. The phase of BFO is classified as a rhombohedral distorted simple perovskite structure belonging to space group R3c at 295 K; the unit cell of perovskite type has a pseudo-cubic lattice parameter a = 0.396 nm [144, 145]. For ALD growth in practice, a water precursor enters a chamber to form a hydroxyl group in the same plane. From a point of view along direction (111) of BFO, there are four oxygen atom planes to form a unit cell, and the ion or bismuth atoms fill in between two oxygen atom planes. The direction of growth of BFO along the surface is (001) because of the substrate effect. The theoretical rate of deposition of one unit cell would be a quarter of the lattice parameter (0.099 nm per cycle), which was near our experimental result, 0.087 nm per cycle at 500 ^{o}C. The growth window of a BFO thin film with an ALD system is from 490 ^{o}C to 520 ^{o}C.

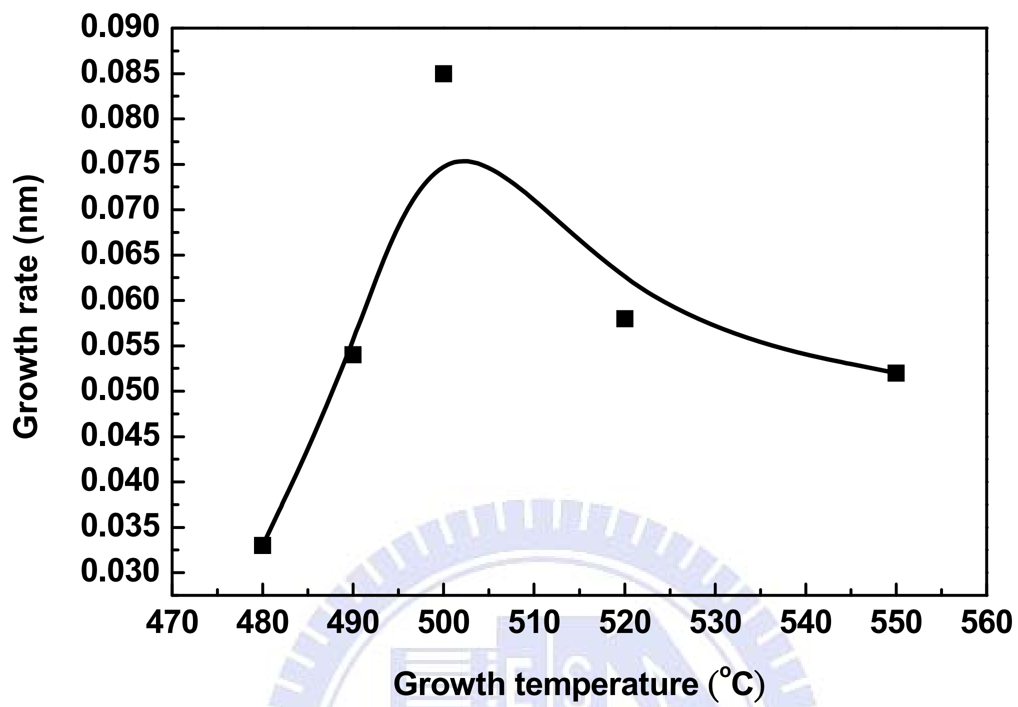

Figure 4.4.1 ALD growth rate as a function of substrate temperature for BFO thin films deposited on the LNO-coated Si substrate.

Figure 4.4.2 shows the XRD patterns measured from the radial scan (θ-2θ scan) alone the surface normal of Si (001) at various growth temperatures of BFO. At a first glance, the peak position of the reflection of BFO (001) is near that of LNO (001), but the integrated intensity of that reflection increased and shifted to a smaller angle with deposition temperature increasing from 480 ^{o}C to 500 ^{o}C, and shows a BFO phase with a preferred orientation along (001). The secondary phase obtained at 490 - 520 ^{o}C is contributed from a reflection of $BiFeO_3$ (111); this is a minor phase of the thin film. The integrated intensity ratio of the reflections for BFO (111)/(001)(111) is just 0.04 %, which means that the properties of the thin film were contributed mostly from the BFO (001) domains. When the temperature was increased to 520 ^{o}C, the Bi_2O_3 (111) reflection appeared and was accompanied with a decreased intensity of BFO (001). The reason is that a higher deposition temperature might cause the decomposition or degradation of the least stable precursor, cyclohexadiene iron tricarbonyl, so that it becomes no longer reactive with hydroxyl for the formation of BFO. Furthermore, a lower temperature cannot provide sufficient energy to grow a BFO crystal of high quality. With higher or lower temperatures of deposition, the intensity of the diffraction signal decreased rapidly; the results signify an optimum temperature for growth, with the nearest growth rate of BFO at 500 ^{o}C.

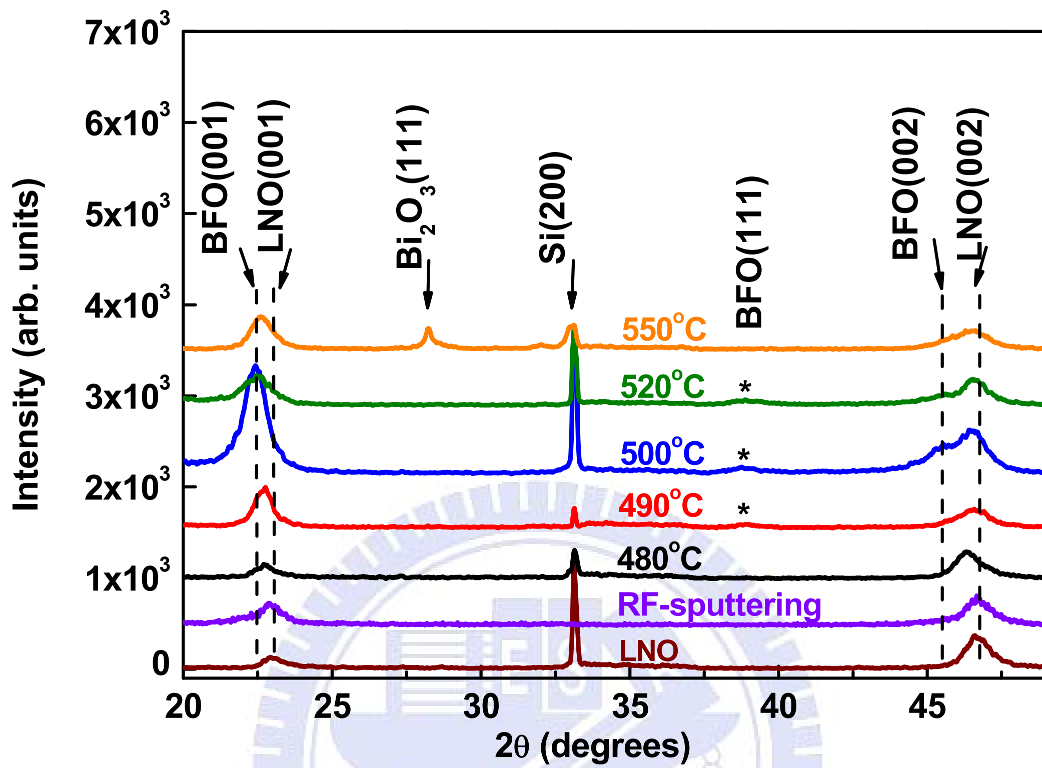

Figure 4.4.2 Surface normal radial XRD spectra of BFO thin film deposited at various substrate temperatures.

In general, X-ray scattering yields information only about long-range order of the atomic structure, but measurements of X-ray absorption fine structure (XAFS) provide chemical information about the short range. DAFS combines all capabilities of XRD and XAFS within a single technique; it provides advantages of information about short-range order about the set or subset of long-range ordered atoms selected by the diffraction condition [111]. DAFS is chemically specific and valence-specific, and is sensitive to the positions of neighboring atoms; atoms can be separated on measuring the DAFS intensities of Bragg peaks with varied contributions of diffraction structure factors. DAFS provides the same structural and spectral sensitivities as X-ray-absorption near-edge structure: valence, empty orbital, and bonding information for the resonant atoms [112, 113]. To deduce the valence of Fe and Bi elements, we present the DAFS results of BFO thin film deposited at 500 ^{o}C and made on the BFO (001) diffraction peak as shown in Figure 4.4.3. The theoretical values of the absorption edge for Fe and Bi atoms were located at 7.112 keV (K-edge) and 13.419 keV (L_3-edge), respectively. The experimental results show strong absorption signals of both Fe and Bi at the maximum peak energies, 7.115 keV and 13.422 keV, respectively. This shift is due to Fe and Bi elements being trivalent ions forming ionic bonds with each other and oxygen ions in BFO, and causing the absorption edge to shift 3.0 eV from the atomic state. As the signals are selected from the BFO ordering peak, the shift phenomenon is strong evidence to indicate that the stoichiometry and the bonding are precise and accurate inside the crystal BFO grain.

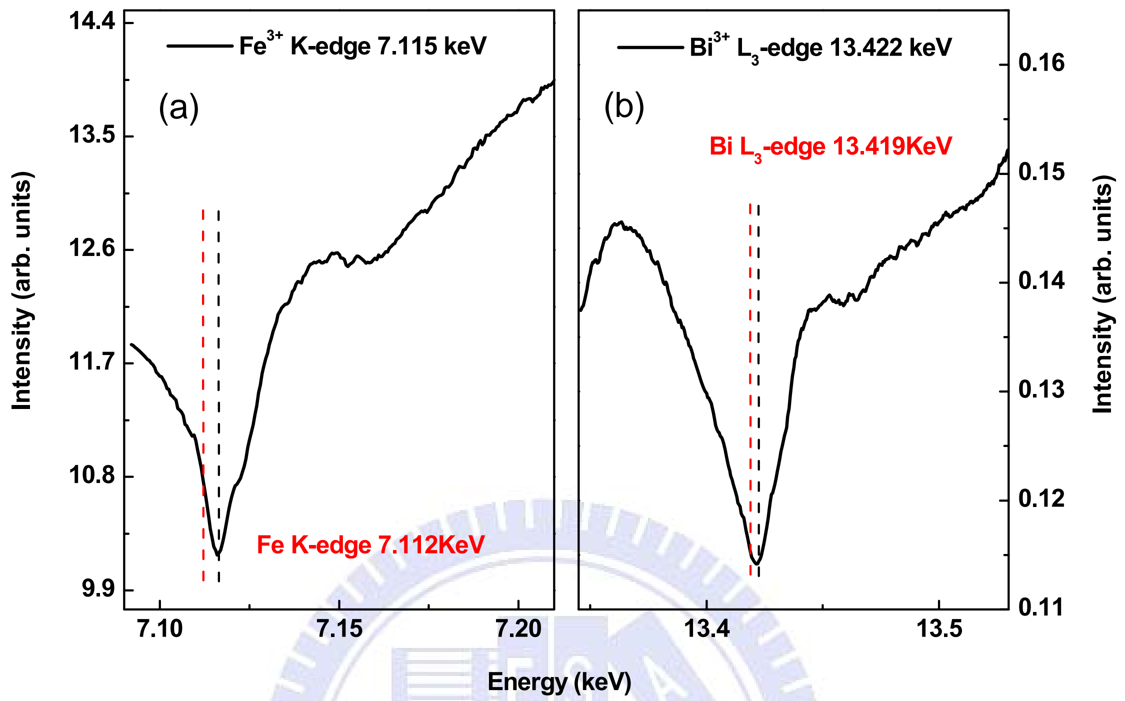

Figure 4.4.3 DAFS results of BFO thin film deposited at 500 °C (a) Fe^{3+} K-edge, and (b) Bi^{3+} L_3-edge.

In order to further understand the composition of the entire BFO thin film, we utilized X-ray photoelectron spectra (XPS) to identify the global stoichiometry of BFO deposited with ALD and RF sputtering; the results are displayed in Figure 4.4.4; Figure 4.4.4(a)-(c) pertain to ALD and Figure 4.4.4(d)-(f) to RF sputtering. The fits of XPS were analyzed with software (XPSPEAK 4.1). The background was subtracted with a linear method and Gaussian-Lorentzian distributions were used to fit the peaks. The atomic fraction of each element of the $BiFeO_3$ films was calculated from the integrated intensity of the peaks and divided by the relative sensitivity factors -- Bi-4f 9.14, Fe-2p 2.957, and O-1s 0.71. The integrated intensity of Bi-4f, Fe-2p and O-1s peaks were calculated to obtain the content of Bi, Fe and O with this equation,

$$C_i = \frac{I_i}{I_{Bi} + I_{Fe} + I_O} \times 100\ \%$$

in which i denotes Bi, Fe or O; C_i is the content of element i in the thin film. Table 4.4.1 shows the calculated atomic fractions for both ALD and RF-sputtered specimens.

The stoichiometry of the BFO thin film from the ALD is much nearer the theoretical value than that from RF-sputtering; with ALD it is much easier to control the atomic fraction of elements because of the advantage of the self-limiting surface reaction. Once a strong ionic bond between cation and anion was formed, it became stable while under the decomposition temperature (proportional to the melting temperature of compounds). Although the Fe atoms are missing about 5 % in the BFO thin film grown by ALD because of insufficient reaction energy, there is only a $BiFeO_3$ phase present according to the XRD result.

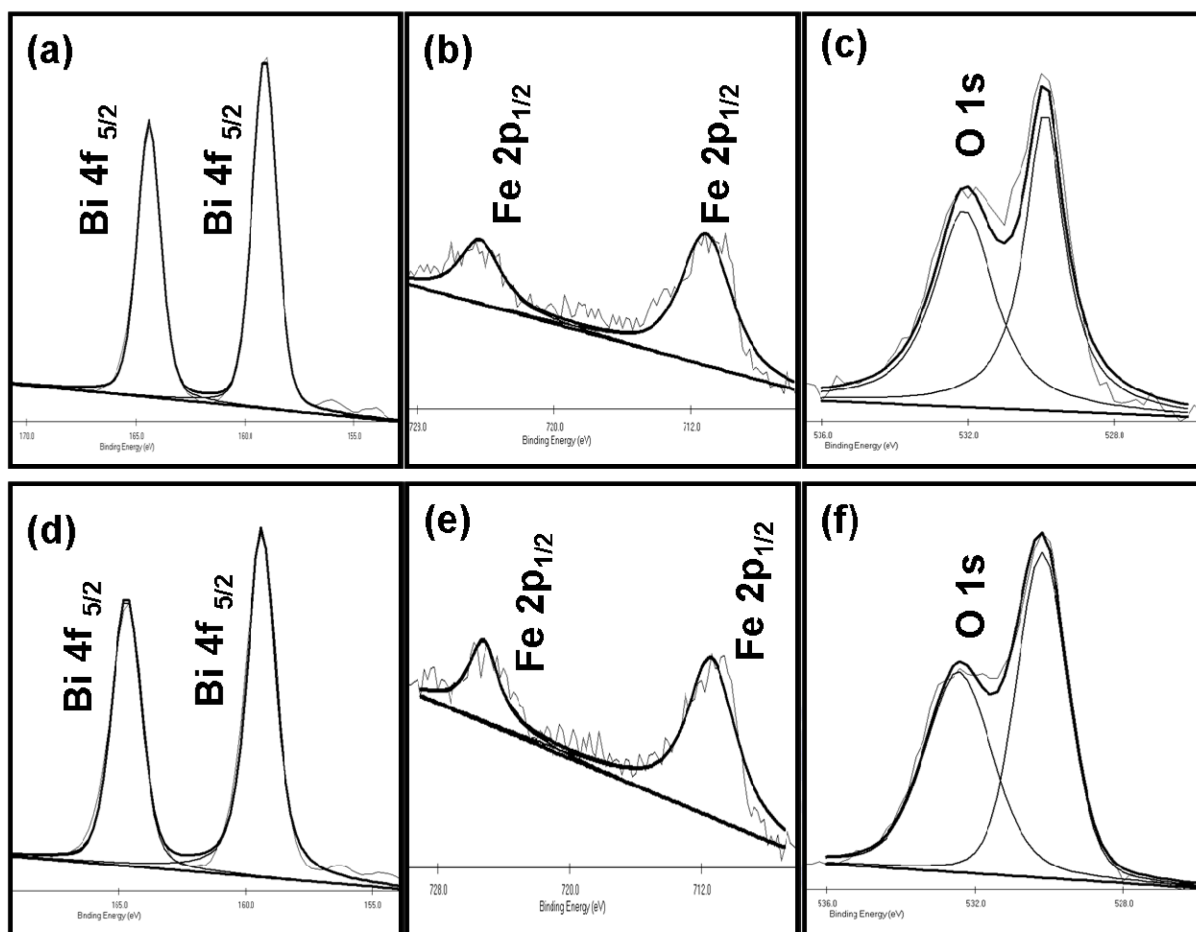

Figure 4.4.4 XPS spectra of BFO thin film by (a)-(c) ALD (d)-(f) RF-sputtering.

Table 4.4.1 Parameters obtained from best-fit results of XPS spectra of BFO thin films deposited on the LNO-coated Si substrate by (a) ALD and (b) RF-sputtering.

	Bi (atom%)	Fe (atom%)	O (atom%)
(a) ALD	24 ± 3	15 ± 3	61 ± 3
(b) RF-sputtering	26 ± 3	5 ± 3	69 ± 3
Theoretical value	20	20	60

4.4.2 Leakage property of the ultra-thin BFO films.

To verify the doubt from XPS, we measured the leakage using a ferroelectric test system (TF Analyzer 2000 FE-Module). Figure 4.4.5 shows logarithmic plots of the leakage current density *J* as a function of applied *E* field [146]. These results clearly show that the leakage currents of all BFO films grown with ALD ware formed in one group with a value (~10^{-4} A/cm^2 with 10 nm) as small as the results from the epitaxial BFO film of thickness 200 nm grown by PLD [147]. The leakage property has improved in recent years, down to 10^{-6} A cm^{-2} for the epitaxial BFO film of thickness up to 450 nm [148]. Furthermore, on comparison of the BFO thin film grown with ALD to that film from RF-sputtering of the same thickness, the leakage current is 0.001 times that of the BFO thin film grown with RF-sputtering. From this point of view, the BFO thin films grown by ALD are suitable for industrial applications, in combination with other advantages of ALD.

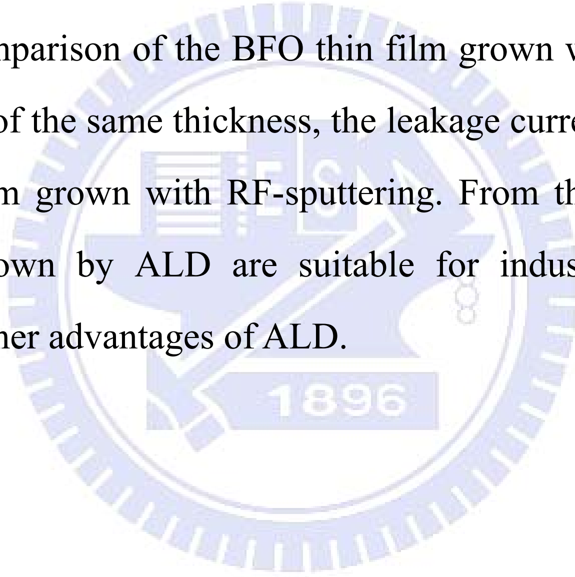

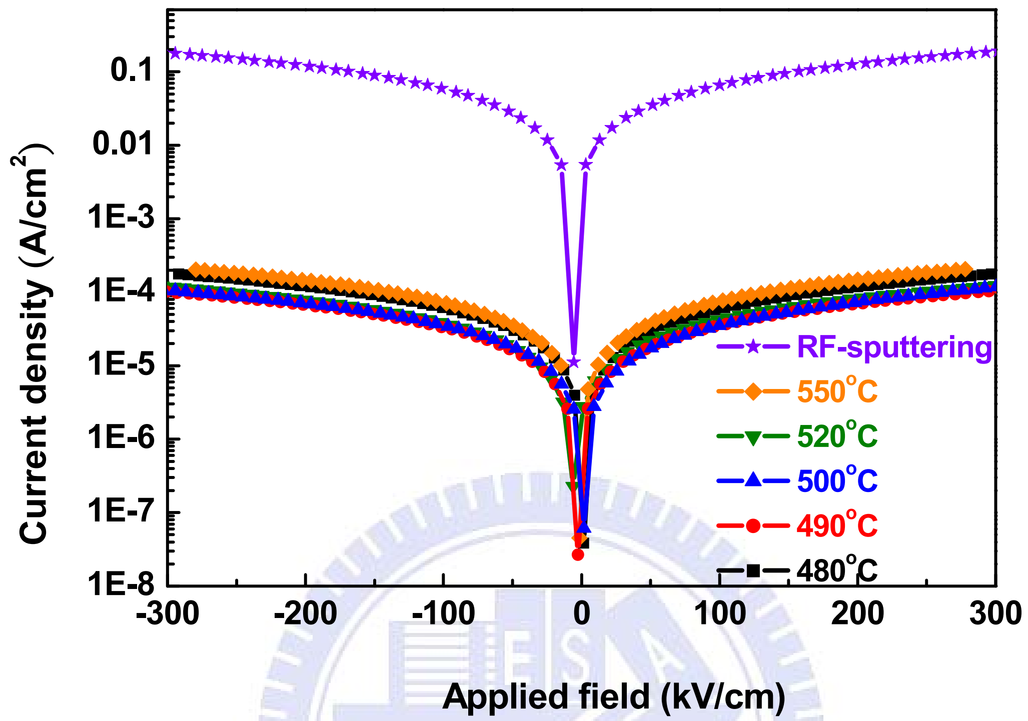

Figure 4.4.5 J-E curves of the BFO thin films with different substrate temperatures.

4.4.3 Cross-sectional image and surface morphology of ultra-thin BFO films

The ALD method exhibits also a highly conformal growth for a thin-film system. To deduce the interfacial joint of perovskite materials, we recorded images of both ALD and RF systems with a HRTEM. Figure 4.4.6 (a) shows HRTEM cross-sectional images of an ALD system; we observed that the BFO thin film fully covered the LNO and maintained the morphology of the LNO surface; the thickness was uniform, but the BFO surface at the top was rough. This condition is also a key advantage for ALD mentioned above. Figure 4.4.6 (b) shows the cross-sectional image of BFO thin film grown by RF- sputtering; the surface was less rough than for the BFO thin film grown with the ALD system. The thickness of the BFO from RF-sputtering was also clearly inhomogeneous; some parts of the film were much less thick than the desired value, as little as only ~ 3 nm.

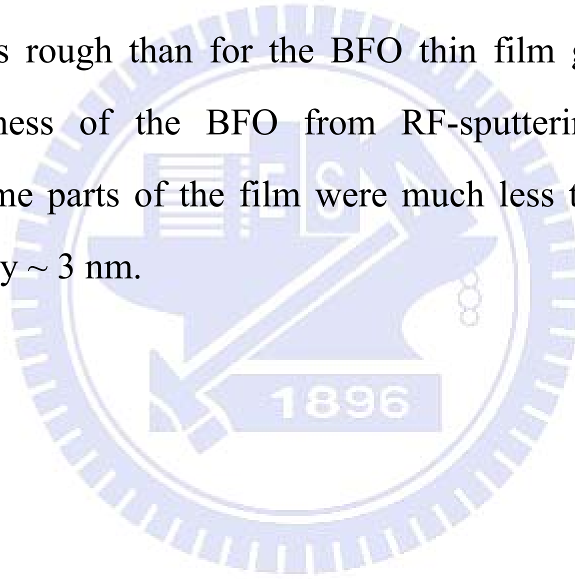

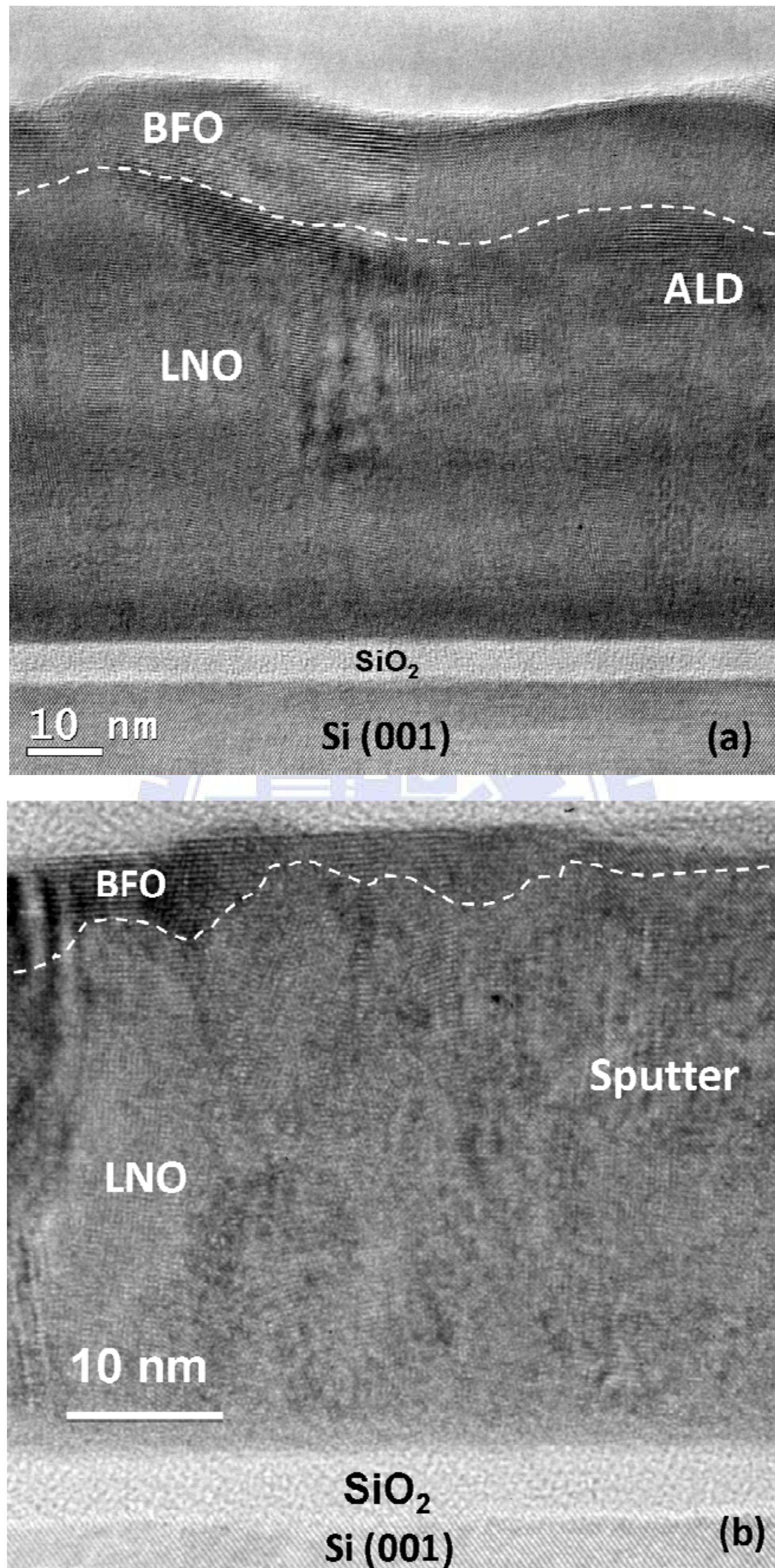

Figure 4.4.6 Cross-section view of HRTEM for BFO thin films grown on LNO buffer layer by (a) ALD (b) RF-sputtering.

To examine the surface roughness, we employed an AFM. The surface morphology of the BFO thin films deposited by ALD and RF-sputtering as examined with the AFM is shown in Figure 4.4.7. The calculated root-mean-square surface roughness of BFO is 1.27 nm for ALD and 0.63 nm for RF-sputtering; the surface roughness of ALD system is thus twice that of the RF-sputtered sample. The results obtained by TEM analysis indicate a relation between the film thickness and the surface morphology. The thin region of the BFO film deposited with RF-sputtering also contributed to the measured leakage current, which is due to quantum tunneling. In general, the electron waveform propagates in materials with a length about 10~20 nm and has a greater probability to tunnel through a barrier of length less than that of the waveform. The leakage current increases with the electron tunneling through the thin area, and the electrons easily leak from the short path of the thin film [149], which was another reason for the great difference of the leakage current between the ALD and RF systems.

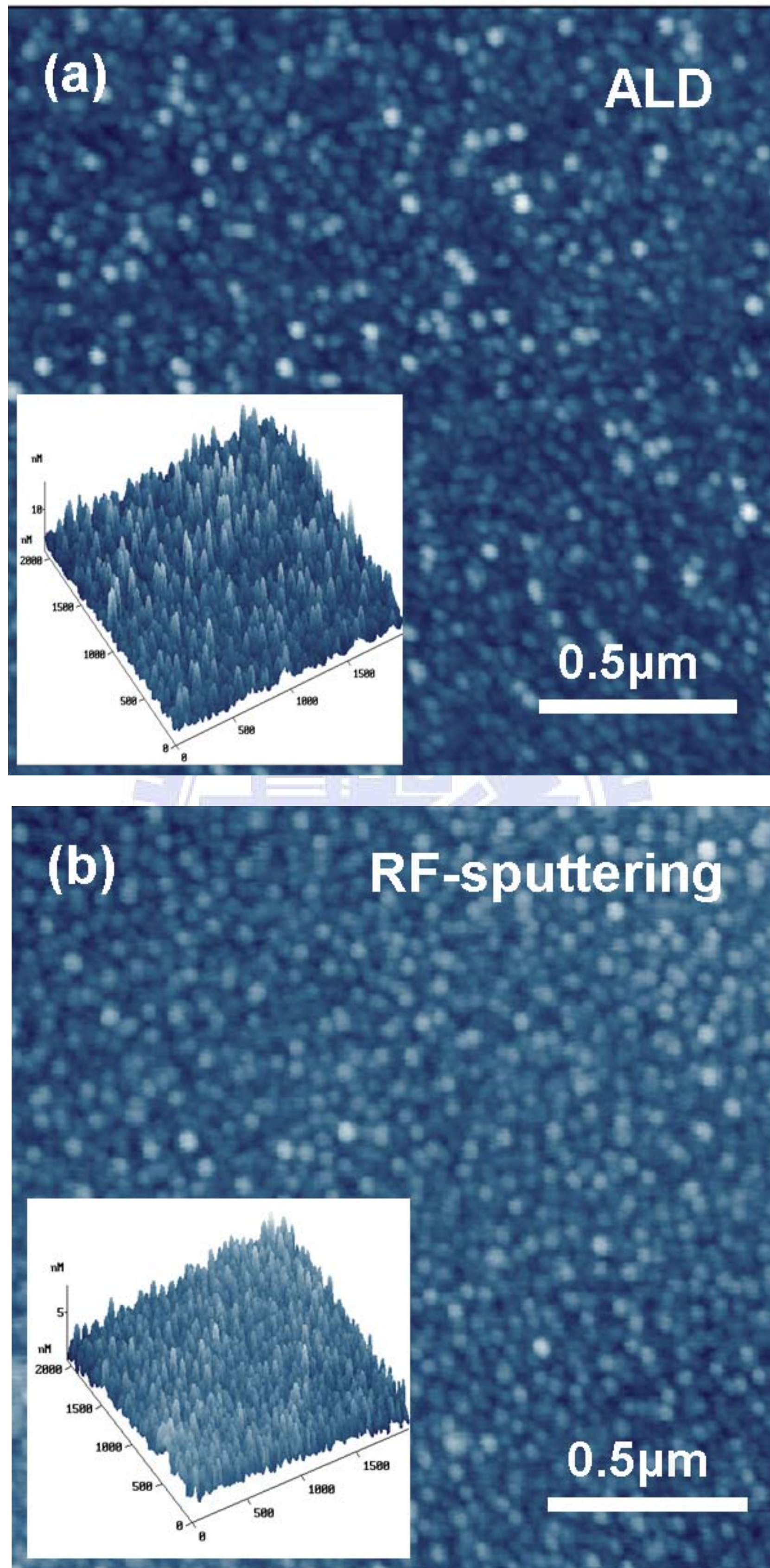

Figure 4.4.7 AFM images of BFO thin films grown by (a) ALD and (b) RF-sputtering.

4.4.4 Ferroelectric property of ultra-thin BFO films.

Ferroelectric properties were characterized using polarization hysteresis; the *P*-*E* hysteresis loop of BFO thin films was measured at 5 V and 5 kHz to reduce the effect of the leakage [150]. To decrease the abundant concentration of the H^+ state remaining in BFO thin films after the ALD processes [151], annealing at a low temperature was applied to the BFO thin film for 2 h at 250 ^{o}C. Figure 4.4.8 shows the results for the ferroelectric property of BFO thin films, from measurements of the hysteresis loop at 295 K; the largest remanent polarization $2P_r$ near 2 μC cm^{-2} was observed from the BFO thin film deposited at 500 ^{o}C. The satisfactory behavior of the polarization was like our previous result with BFO thin films of thickness about 60 nm fabricated with RF-sputtering, but just one sixth the thickness from ALD [96]. The polarization decreased rapidly because of the crystal quality, and a foreign phase appeared in BFO on deposition at lower or higher temperatures. For comparison, the hysteresis loop of a BFO thin film of thickness 10 nm grown with RF-sputtering was also employed and is shown in Figure 4.4.8; it is difficult to obtain a saturated P-E loop and the polarization shows nearly no ferroelectric property because of the large leakage current.

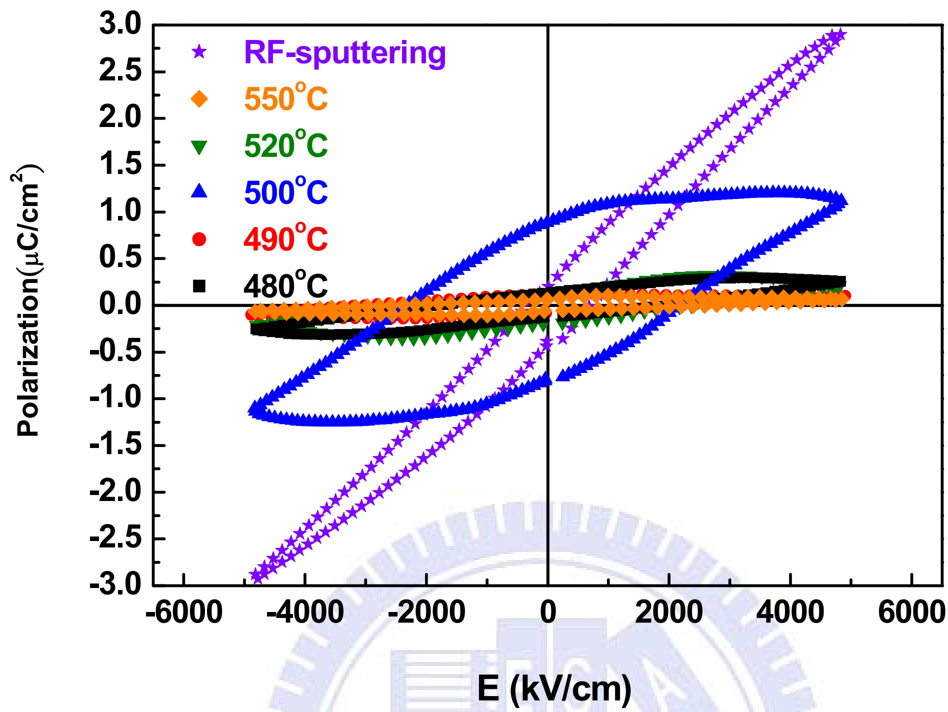

Figure 4.4.8 P-E hysteresis loops of BFO thin film deposited in the range of substrate temperature 480-550 °C.

Although the leakage plays an important role in the polarization measurement, the leakage behavior affected only the saturation feature of the *P-E* loop because of the capacitance effect, not the value of polarization. In this case, we could obtain an intrinsic polarization at a condition of smaller leakage. The polarization is dominated by the crystalline quality, which is contributed from a large displacement of the central atom in the unit cell. In this work, the crystal structure has a large variation of substrate temperature, shown in Figure 4.4.9. The crystalline quality increased with growth temperature increasing to 500 ^{o}C, and decreasing again for a temperature in excess of the optimal condition. Moreover, the leakage current density shows a trend opposite to that of crystalline quality from XRD at various substrate temperatures.

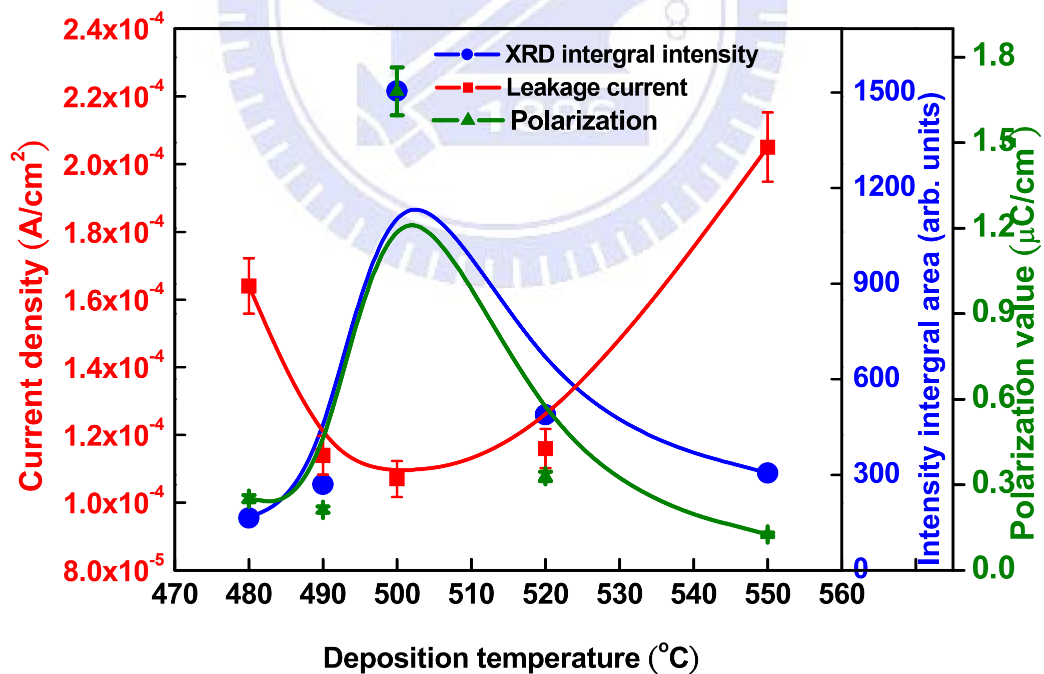

Figure 4.4.9 The relationship among crystal structure, leakage current, and polarization at various deposition temperatures of ALD.

To consider a relation between thickness and polarization, we assembled a series of experimental data for BFO (001) with thickness as a function of polarization normalized with thickness, shown in Figure 4.4.10. Besides ALD, all results from PLD [2, 12, 147], CVD [4], sol-gel [152], and RF-sputtering [8, 153, 154] can yield a statistical linear regression curve with a point of intersection about 30 nm. From the literatures, authors also mentioned that it becomes difficult to quantity the ferroelectric or piezoelectric properties in a capacitor geometry below 50 nm because of a progressively larger contribution from leakage [155]. This report is the first credible remanent polarization for a thickness less than 30 nm and a satisfactory leakage parameter for FeRAM application at the state of art. As FeRAM has a cell structure similar to that of dynamic random-access memory (DRAM) in a contemporary design, the growth of BFO must still face the same problem as current DRAM devices. The DRAM capacitor technology is now more seriously challenged because of the accelerated scaling of cell size. For stacked capacitor or vertical transistor technology, as the dimension decreases to 20 nm, the most difficult situation is insufficient space for the deposition of the dielectric layers and the electrode. In this case, the aspect ratio between the cap and device typically exceeds 1:50, which is a large barrier for PVD and CVD processes. ALD is a suitable technique to deposit a dielectric film and an electrode into a deep trench with improving process performance such as step coverage and throughput, but, as the trench narrows to 13 nm, the industry needs ALD growth for multi-component films such as (Ba,Sr)TiO_3 (BST) or $SrRuO_3$, while maintaining the stoichiometry and step coverage using precursors with poor reactivity (poor growth rate). BFO currently gains much attention as a new candidate material for FRAM, but it also requires a higher switching voltage, which means that the

film needs to be thinner, or possibly doped to accommodate operation at a low voltage. The minimum switching charge value Q_{sw}, (assumed to be 30 μC/cm^2), then yields the desired area of the capacitor. If this area is larger than the projected capacitor size, a 3D capacitor should be adopted to solve this problem [156].

ALD grown BFO thin films show a great capability to fulfill the requirements of stoichiometry and a large rate of growth (0.087 nm per cycle) to yield the throughput for FRAM. Furthermore, we reveal that the thickness of BFO could be as little as less than 10 nm to improve the switching voltage in a FRAM application and still retain satisfactory leakage properties. Although the polarization was not great enough for a desired FRAM now, at least two ways to improve this problem are shown: fabrication of a 3D capacitor through the advantage of ALD, and growth of the BFO from the (001) to the (111) direction to improve the polarization through easy-axis operation.

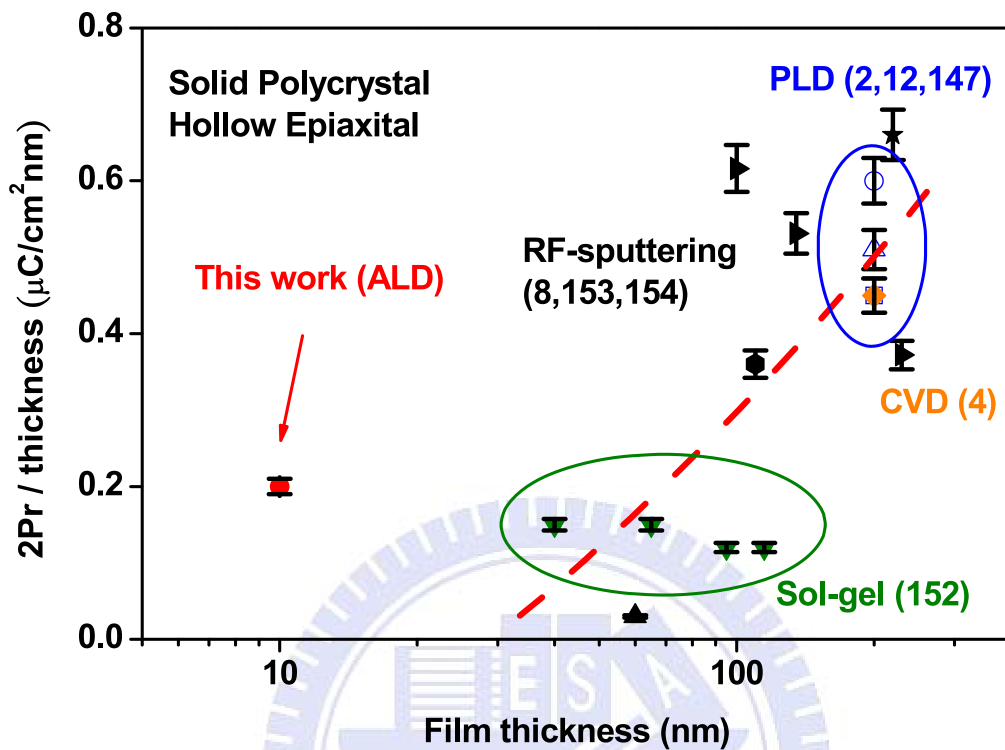

Figure 4.4.10 Normalized polarization as a function of film thickness grown by RF-sputtering, PLD, CVD, Sol-gel, and ALD this work.

Chapter 5

Conclusions

To investigate the structure and ferroelectric properties of BFO thin films, we have grown highly (001)-oriented single-layer BFO films on the LNO-coated Si substrate in temperature range of 400 – 600 °C with HV RF-sputtering With X-ray reflectivity and diffraction we characterized the structure of the buried interface and the surface morphology. The result fitted from X-ray reflectivity curves shows that the density of the BFO film is slightly less than that of the bulk values. The measurement of the hysteresis loops shows that the largest remanent polarization (P_r) occurs at deposition temperature 500 °C. These measurements of hysteresis loops show that the ferroelectric properties of BFO films are highly correlated with the degree of preferred orientation between the substrate and the film.

To improve the ferroelectric properties with the crystal quality, a BFO/ LNO superlattice was fabricated on the Nb-doped STO substrate in the temperature range of 560 – 810 °C with a UHV RF-sputtering system. For measurements of X-ray reflectivity and diffraction, we characterized the structure of the buried interface and the surface morphology. HRTEM images indicate a well defined layer structure of BFO/LNO on the STO substrate and a strong epitaxial relation among film, interface and substrate. DAFS measurements confirmed the formation of a NiO phase for a film deposited at and above 710 °C. The superlattice structure became gradually degraded through the formation of the NiO phase for a film deposited at a temperature ≧710 °C, and was severely destroyed at 810 °C. The largest remanent polarization of a BFO/LNO superlattice occurred at deposition temperature 660

°C. These measurements of hysteresis loops show that the ferroelectric properties of BFO/LNO superlattice films are strongly correlated with lattice strain, interface roughness, and crystalline quality of the films.

With optimized grown condition of the BFO/LNO superlattice, we fabricated the BFO/LNO superlattice with varied sublayer thicknesses and periods to study the effect of strain on the electrical properties. We studied also the effect of leakage current on the polarization. We characterized the structure of the interface and the surface morphology from measuring the X-ray reflectivity and diffraction. An intrinsic remanent polarization of the superlattices was observed at sublayer thicknesses in the range of 1.7–8.5 nm at 5 kHz. The periods and thicknesses of the superlattices confirmed with XRD and XRR are consistent with the results of SIMS. The rounded shape of the hysteresis loop at frequency ≦2 kHz resulted from a large dc leakage and extrinsic interface effects.

In the latter work, we clearly demonstrated a new capability to achieve a uniform fabrication of a large area, and showed a satisfactory performance of BFO materials to create a new application in the electroceramic field. In summary, highly oriented BFO thin films of thickness 10 nm were deposited on a LNO-coated Si (001) substrate with ALD. The BFO thin films show purely a single phase and satisfactory crystalline quality at optimum temperature 500 ^{o}C. Both DAFS and XPS results show strong evidence of comparatively fine stoichiometry of BFO thin film from ALD. The HRTEM cross-sectional view shows a conformal and uniform deposition on the top of LNO buffer layer. The leakage current density of BFO grown with ALD showed a correct performance as epitaxial films compared with previous reports, which is due to the conformal

growth properties of ALD and free of pinholes. The excellent leakage also yielded a credible remanent polarization, approximately $2P_r$ = 2.0 μC cm^{-2} obtained from BFO thin film at 500 ^oC. This remanent polarization shows a strong correlation with the growth rate; the greatest crystalline quality appeared for a growth rate near the theoretical value at an appropriate temperature. The complete mixed ternary BFO growth with ALD at an appropriate rate showed a layer-by-layer growth of O-Fe-Bi atoms reflecting a satisfactory stoichiometry and valence bonding. This advantage benefits the IC fabrication using an in-situ monitor of film thickness such as a quartz-crystal microbalance sensor.

Reference

[1]N. A. Hill, "Why Are There so Few Magnetic Ferroelectrics?" J. Phys. Chem. B **104**, 6694-6709. (2000)

[2]J. Wang, J. B. Neaton, H. Zheng, V. Nagarajan, S. B. Ogale, B. Liu, D. Viehland, V. Vaithyanathan, D. G. Schlom, U. V. Waghmare, N. A. Spaldin, K. M. Rabe, M. Wuttig, and R. Ramesh, "Epitaxial $BiFeO_3$ Multiferroic Thin Film Heterostructures" Science **299**, 1719-1722. (2003)

[3] W. Eerenstein, N. D. Mathur, and J. F. Scott, "Multiferroic and magnetoelectric materials" Nature (London) **442**, 759-765. (2006)

[4] S. Y. Yang, F. Zavaliche, L. Mohaddes-Ardabili, V. Vaithyanathan, D. G. Schlom, Y. J. Lee, Y. H. Chu, M. P. Cruz, Q. Zhan, T. Zhao, and R. Ramesh, "Metalorganic chemical vapor deposition of lead-free ferroelectric $BiFeO_3$ films for memory applications" Appl. Phys. Lett. **87**, 102903-1-102903-3. (2005)

[5] T. Kimura, T. Goto, H. Shintani, K. Ishizaka, T. Arima, and Y. Tokura, "Magnetic control of ferroelectric polarization" Nature (London) **426**, 55-58. (2003)

[6]Y. H. Lee, J. M. Wu, and C. H. Lai, "Influence of La doping in multiferroic properties of $BiFeO_3$ thin films" Appl. Phys. Lett. **88**, 042903-1-042903-3. (2006)

[7]S. K. Singh, and H. Ishiwara, "Doping Effect of Rare-Earth Ions on Electrical Properties of $BiFeO_3$ Thin Films Fabricated by Chemical Solution Deposition" Jpn. J. Appl. Phys. **45**, 3194-3197. (2006)

[8]C. C. Lee, J. M. Wu, and C. P. Hsiung, "Highly (110)- and (111)-oriented $BiFeO_3$ films on $BaPbO_3$ electrode with Ru or Pt/Ru barrier layers" Appl.

Phys. Lett. **90**, 182909-1-182909-3. (2007)

[9] G. A. Smolenskii, V. M. Yudin, E. S. Sher, and Y. E. Stolypin, “Antiferromagnetic properties of some Perovskites” Sov. Phys. JETP **16**, 622-624. (1963)

[10] P. Fischer, M. Polomska, I. Sosnowska, and M. Szymanski, “Temperature dependence of the crystal and magnetic structures of $BiFeO_3$” J. Phys. C **13**, 1931-1940. (1980)

[11] M. Dawber, K. M. Rabe, and J. F. Scott, “Physics of thin-film ferroelectric oxides” Rev. Mod. Phys. **77**, 1083-1130. (2005)

[12] J. Wang, H. Zheng, Z. Ma, S. Prasertchoung, M. Wuttig, R. Droopad, J. Yu, K. Eisenbeiser, and R. Ramesh, “Epitaxial $BiFeO_3$ thin films on Si” Appl. Phys. Lett. **85**, 2574-2576. (2004)

[13] J. Thery, C. Dubourdieu, T. Baron, C. Ternon, H. Roussel, and F. Pierre, “MOCVD of $BiFeO_3$ Thin Films on $SrTiO_3$” Chem. Vap. Deposition **13**, 232-238. (2007)

[14] Y. Tasaki, T. Kanoko, M. Kabeya, N. Chifu, and S. Yoshizawa, “Evaluation of Metalorganic Precursors for Preparing $BiFeO_3$ Thin Films by Liquid Delivery Chemical Vapor Deposition” Integr. Ferroelectr. **81**, 281-288. (2006)

[15] J. C. Jiang, X. Q. Pan, W. Tian, C. D. Theis, and D. G. Schlom, “Abrupt $PbTiO_3$ /$SrTiO_3$ superlattices grown by reactive molecular beam epitaxy” Appl. Phys. Lett. **74**, 2851-2853. (1999)

[16] M. Lippmaa, N. Nakagawa, M. Kawasaki, S. Ohashi, and H. Koinuma, “Growth mode mapping of $SrTiO_3$ epitaxy” Appl. Phys. Lett. **76**, 2439-2441. (2000)

[17] S. O. Park, C.S. Huang, H. Cho, C. S. Kang, H. Kang, S. I. Lee, and M. Y.

Lee, "Fabrication and Electrical Characterization of Pt/(Ba,Sr)TiO_3/Pt Capacitors for Ultralarge-Scale Integrated Dynamic Random Access Memory Applications" Jpn. J. Appl. Phys. **35**, 1548-1552. (1996)

[18] Y. C. Liang, and Y. C. Liang, "Effects of substrate temperature on the physical properties of strained $BaTiO_3$/$LaNiO_3$ artificial superlattices" J. Cryst. Growth **285**, 345-351. (2005)

[19] M. Matsuoka, K. Hoshino, and K. Ono, "Low-temperature epitaxial growth of $BaTiO_3$ films by radio-frequency-mode electron cyclotron resonance sputtering" J. Appl. Phys. **76**, 1768-1775. (1994)

[20] R. R. Das, D. M. Kim, S. H. Back, C. B. Eom, F. Zavaliche, S. Y. Yang, R. Ramesh, Y. B. Chen, X. Q. Pan, X. Ke, M. S. Rzchowski, and S. K. Streiffer, "Synthesis and ferroelectric properties of epitaxial $BiFeO_3$ thin films grown by sputtering" Appl. Phys. Lett. **88**, 242904-1-242904-3. (2006)

[21] C. M. Wu, and T. B. Wu, "Effects of $LaNiO_3$ Conductive Buffer Layer on The Structural and Electrical Characteristics of $Ba_{0.4}Sr_{0.6}TiO_3$ Thin Films Prepared by RF Magnetron Sputtering" Jpn. J. Appl. Phys. **36**, 1164-1168. (1997)

[22] C. C. Yang, M. S. Chen, T. J. Hong, C. M. Wu, J. M. Wu, and T. B. Wu, "Preparation of (100)-oriented metallic $LaNiO_3$ thin films on Si substrates by radio frequency magnetron sputtering for the growth of textured $Pb(Zr_{0.53}Ti_{0.47})O_3$" Appl. Phys. Lett. **66**, 2643-2645. (1995)

[23] M. J. Shyu, T. J. Hong, and T. B. Wu, "Highly (100)-Oriented Thin Films of Sol-Gel Derived $Pb[(Mg_{1/3}Nb_{2/3})_{0.675}Ti_{0.325}]O_3$ Prepared on Textured $LaNiO_3$ Electrode" Jpn. J. Appl. Phys. **34**, 3647-3653. (1995)

[24] M. J. Shyu, T. J. Hong, and T. B. Wu, "Properties of highly (100)-oriented thin films of sol-gel derived $Pb[(Mg_{1/3}Nb_{2/3})_xTi_{1-x}]O_3$ on (100)-textured $LaNiO_3$ electrode" Mater. Lett. **23**, 221-226. (1995)

[25] H. J. Liu, K. Yao, P. Yang, Y. H. Du, Q. He, Y. L. Gu, X. L. Li, S. H. Wang, X. T. Zhou, and J. Wang, "Thickness-dependent twinning evolution and ferroelectric behavior of epitaxial $BiFeO_3$ (001) thin films" Phys. Rev. B **82**, 064108-1-064108-6. (2010)

[26] R. Ranjith, B. Kundys, and W. Prellier, "Periodicity dependence of the ferroelectric properties in $BiFeO_3$ /$SrTiO_3$ multiferroic superlattices" Appl. Phys. Lett. **91**, 222904-1-222904-3. (2007)

[27] M. S. Chen, T. B. Wu, and J. M. Wu, "Effect of textured $LaNiO_3$ electrode on the fatigue improvement of $Pb(Zr_{0.53}Ti_{0.47})O_3$ thin films" Appl. Phys. Lett. **68**, 1430-1432. (1996)

[28] C. Guerrero, F. Sanchez, C. Ferrater, J. Roldan, M. V. Garcia, and M. Varela, "Pulsed laser deposition of epitaxial $PbZr_xTi_{1-x}O_3$ ferroelectric capacitors with $LaNiO_3$ and $SrRuO_3$ electrodes" Appl. Surf. Sci. **168**, 219-222. (2000)

[29] P. Chen, S. Y. Xu, W. Z. Zhou, C. K. Ong, and D. F. Cui, "In situ reflection high-energy electron diffraction observation of epitaxial $LaNiO_3$ thin films" J. Appl. Phys. **85**, 3000-3002. (1995)

[30] H. Y. Lee, H. J. Liu, Y. C. Liang, K. F. Wu, and C. H. Lee, "Structural and dielectric properties of sputter-deposited $Ba_{0.48}Sr_{0.52}TiO_3$/$LaNiO_3$ artificial superlattice films" J. Electrochem. Soc. **156 (8)**, G114-G119. (2009)

[31] C. S. Ku, H. Y. Lee, J. M. Huang, and C. M. Lin, "Epitaxial growth of m-plane ZnO thin films on (1010) sapphire substrate by atomic layer deposition with interrupted flow" Cryst. Growth Des. **10**, 1460-1463.

(2010)

[32] O. S. Kwon, S. W. Lee, J. H. Han, and C. S. Hwang, "Atomic Layer Deposition and Electrical Properties of $SrTiO_3$ Thin Films Grown Using $Sr(C_{11}H_{19}O_2)_2$, $Ti(O_i\text{-}C_3H_7)_4$, and H_2O Dielectric Science and Materials:" J. Electrochem. Soc. **154**, G127-G133. (2007)

[33] G. W. Hwang, W. D. Kim, Y. S. Min, Y. J. Cho, and C. S. Hwang, "Characteristics of Amorphous $Bi_2Ti_2O_7$ Thin Films Grown by Atomic Layer Deposition for Memory Capacitor Applications Dielectric Science and Materials" J. Electrochem. Soc. **153**, F20-F26. (2006)

[34] S. W. Lee, O. S. Kwon, J. H. Han, and C. S. Hwang, "Enhanced electrical properties of $SrTiO_3$ thin films grown by atomic layer deposition at high temperature for dynamic random access memory applications" Appl. Phys. Lett. **92**, 222903-1-222903-3. (2008)

[35] J. W. Elam, Z. A. Sechrist, and S. M. George, "ZnO/Al_2O_3 nanolaminates fabricated by atomic layer deposition: growth and surface roughness measurements" Thin Solid Films **414**, 43-55. (2002)

[36] C. S. Ku, H. Y. Lee, J. M. Huang, and C. M. Lin, "Epitaxial growth of ZnO films at extremely low temperature by atomic layer deposition with interrupted flow" Mater. Chem. and Phys. **120**, 236-239. (2010)

[37] G. A. Smolenski, and I. E. Chupis, "Ferroelectromagnets" Sov. Phys. Usp. **25**, 475-493. (1982)

[38] H. Schmid, "Multi-ferroic magnetoelectrics" Ferroelectrics **162**, 317-338. (1994)

[39] M. Bibes, and A. Barthélémy, "Multiferroics: Towards a magnetoelectric memory" Nature Materials **7**, 425-426. (2008)

[40] W. F. Brown, Jr., R. M. Hornreich, and S. Shtrikman, "Upper Bound on the

Magnetoelectric Susceptibility" Phys. Rev. **168**, 574-577. (1968)

[41] M. Gajek, M. Bibes, S. Fusil, K. Bouzehouane, J. Fontcuberta, A. Barthélémy, and A. Fert " Multiferroic tunnel junctions" Preprint at (http://arxiv.org/ cond-mat/0606444). (2006)

[42] H. Schmid, "On a magnetoelectric classification of materials" Int. J. Magn. **4**, 337-361. (1973)

[43] E. Ascher, H. Rieder, H. Schmid, and H. J. Sto¨ssel, "Some Properties of Ferromagnetoelectric Nickel-Iodine Boracite, $Ni_3B_7O_{13}I$" J. Appl. Phys. **37**, 1404-1405. (1966)

[44] M. E. Lines, and A. M. Glass, "Principles and Applications of Ferroelectrics and Related Materials" (Oxford: Clarendon), (1979)

[45] T. Mitsui, I. Tatsuzaki, and E. Nakamura, "An Introduction to the Physics of Ferroelectrics" (London: Gordon and Breach), (1976)

[46] F. Joan, and G. Shirane, "Ferroelectric Crystals"402 S. Oxford/London/New York/Paris. Pergamon Press. Preis geb. 84 s. net), (1962)

[47] D. Damjanovic, "Ferroelectric, dielectric and piezoelectric properties of ferroelectric thin films and ceramics" Rep. Prog. Phys. **61**, 1267-1324. (1998)

[48] C. B. Sawyer, and C. H. Tower, "Rochelle Salt as a Dielectric" Phys. Rev. **35**, 269-273. (1930)

[49] J. M. Moreau, C. Michel, R. Gerson, and W. J. James, "Ferroelectric $BiFeO_3$ X-ray and neutron diffraction study" J. Phys. Chem. Solids **32**, 1315-1320. (1971)

[50] C. Blaauw, and F. van der Woude, "Magnetic and structural properties of $BiFeO_3$," J. Phys. C: Solid State Phys. **6**, 1422-1431. (1973)

[51] F. Kubel, and H. Schmid, “Structure of a ferroelectric and ferroelastic monodomain crystal of the perovskite $BiFeO_3$” Acta Cryst. B **46**, 698-702. (1990)

[52] J. D. Bucci, B. K. Robertson, and W. J. James, “The precision determination of the lattice parameters and the coefficients of thermal expansion of $BiFeO_3$” J. Appl. Cryst. **5**, 187-191. (1972)

[53] J. R. Chen, W. L. Wang, J.-B. Li, and G. H. Rao, “X-ray diffraction analysis and specific heat capacity of $(Bi_{1-x}La_x)FeO_3$ perovskites” J. Alloys Compd. **459**, 66-70. (2008)

[54] A. Palewicz, R. Przeniosło, I. Sosnowska, and A. W. Hewat, “Atomic displacements in $BiFeO_3$ as a function of temperature: neutron diffraction study” Acta Cryst. **63**, 537-544. (2007)

[55] J. R. Teague, R. Gerson, and W. J. James, “Dielectric hysteresis in single crystal $BiFeO_3$” Solid State Commun. **8**, 1073-1074. (1970)

[56] P. Fischer, and M. Polomska, “Temperature dependence of the crystal and magnetic structures of $BiFeO_3$” J. Phys. C: Solid State **13**, 1931-1940. (1980)

[57] G. Smolenskii, V. Isupov, A. Agranovskaya, and N. Krainik, “New ferroelectrics of complex composition” Sov. Phys. Solid State **2**, 2651-2654. (1961)

[58] S. V. Kiselev, R. P. Ozerov, and G. S. Zhdanov, “Detection of magnetic arrangement in $BiFeO_3$ ferroelectric by means of neutron diffraction study” Dokl. Akad. Nauk SSSR **145**, 1255-1258. (1962)

[59] A. M. Kadomtseva1 , Y. F. Popov , A. P. Pyatakov, G. P.Vorob’ev, A. K. Zvezdin, and D. Viehland, “Phase transitions in multiferroic $BiFeO_3$ crystals, thin-layers, and ceramics: enduring potential for a single phase,

room-temperature magnetoelectric 'holy grail'" Phase Transitions: A Multinational Journal **79**, 1019-1042. (2006)

[60] D. Lebeugle, D. Colson, A. Forget, M. Viret, P. Bonville, J. F. Marucco, and S. Fusil, "Room-temperature coexistence of large electric polarization and magnetic order in $BiFeO_3$ single crystals" Phys. Rev. B **76**, 024116-1-024116-8. (2007)

[61] D. Lebeugle, "Groupement de Recherche sur les Nouveaux Etats Electroniques de la Matiere: GdR NEEM"; Gif sur Yvette, November (2006)

[62] R. P. S. M. Lobo, R. L. Moreira, D. Lebeugle, and D. Colson, "Infrared phonon dynamics of a multiferroic $BiFeO_3$ single crystal" Phys. Rev. B **76**, 172105-1-172105-4. (2007)

[63] M. Cazayous, D. Malka, D. Lebeugle, and D. Colson, "Electric field effect on $BiFeO_3$ single crystal investigated by Raman spectroscopy" Appl. Phys. Lett. **91**, 071910-1-71910-3. (2007)

[64] D. Lebeugle, D. Colson, A. Forget, and M. Viret "Very large spontaneous electric polarization in $BiFeO_3$ single crystals at room temperature and its evolution under cycling fields" Appl. Phys. Lett. **91**, 022907-1-022907-3. (2007)

[65] V. V. Shvartsman, W. Kleemann, R. Haumont, and J. Kreisel, "Large bulk polarization and regular domain structure in ceramic$BiFeO_3$" Appl. Phys. Lett. **90**, 172115-1-172115-3. (2007)

[66] P. Ravindran, R. Vidya, A. Kjekshus, H. Fjellvag, and O. Eriksson, "Theoretical investigation of magnetoelectric behavior in $BiFeO_3$" Phys. Rev. B **74**, 224412-1-224412-18. (2006)

[67] C. Ederer, and N. A. Spaldin, "Effect of Epitaxial Strain on the

Spontaneous Polarization of Thin Film Ferroelectrics" Phys. Rev. Lett. **95**, 257601-1-257601-4. (2005)

[68] D. Bao, N. Mizutani, X. Yao, and L. Zhang, "Structural, dielectric, and ferroelectric properties of compositionally graded (Pb,La)TiO_3 thin films with conductive $LaNiO_3$ bottom electrodes" Appl. Phys. Lett. **77**, 1041-1043. (2000)

[69] K. R. Nikolaev, A. Bhattacharya, P. A. Kraus, V. A. Vas'ko, W. K. Cooley, and A. M. Goldman, "Indications of antiferromagnetic interlayer coupling in $La_{2/3}$ $Ba_{1/3}$ MnO_3 /$LaNiO_3$ multilayers" Appl. Phys. Lett. **75**, 118-120. (1999)

[70] J. Z. Sun, W. J. Gallagher, P. R. Duncombe, L. Krusin-Elbaum, R. A. Altman, A. Gupta, Y. Lu, G. Q. Gong, and G. Xiao, "Observation of large low-field magnetoresistance in trilayer perpendicular transport devices made using doped manganate perovskites" Appl. Phys. Lett. **69**, 3266-3268. (1996)

[71] D. C. Worledge, and T. H. Geballe, "Magnetoresistive double spin filter tunnel junction" J. Appl. Phys. **88**, 5277-5279. (2000)

[72] K. M. Satyalakshmi, R. M. Mallya, K. V. Ramanathan, X. D. Wu, B. Brainard, D. C. Gautier, N. Y. Vasanthacharya, and M. S. Hegde, "Epitaxial metallic $LaNiO_3$ thin films grown by pulsed laser deposition" Appl. Phys. Lett. **62**, 1233-1235. (1993)

[73] A. Yu. Dobin, K. R. Nikolaev, I. N. Krivorotov, R. M. Wentzcovitch, E. Dan Dahlberg, and A. M. Goldman1 "Electronic and crystal structure of fully strained $LaNiO_3$ films" Phys. Rev B **68**, 113408-1-113408-4. (2003)

[74] J. Javier, and G. Philippe, "Critical thickness for ferroelectricity in

perovskite ultrathin films" Nature **422**, 506-509. (2003)

[75] H. Lü, S. Dai, Z. Chen, L. Yan, Y. Zhou, and G. Yang. "Colossal magnetoresistive p-n junctions of perovskite oxide $La_{0.9}Sr_{0.1}MnO_3/SrNb_{0.01}Ti_{0.99}O_3$" Chin. Sci. Bull. **48**, 1328-1330. (2003)

[76] M. Kubo, Y. Oumi, R. Miura, A. Stirling, A. Miyamoto, M. Kawasaki, M. Yoshimoto, and H. Koinuma, "Atomic control of layer-by-layer epitaxial growth on $SrTiO_3$(001): Molecular-dynamics simulations" Phys Rev B **56**, 13535-13542. (1997)

[77] T. Tomio, H. Miki, H. Tabata, T. Kawai, and S. Kawai, "Control of electrical conductivity in laser deposited $SrTiO_3$ thin films with Nb doping" J. Appl. Phys **76**, 5886-5890. (1994)

[78] K. Fukushima, and S. Shibagaki, "Nb doped $SrTiO_3$ thin films deposited by pulsed laser ablation" Thin Solid Films **315**, 238-243. (1998)

[79] F. Gervais, J. L. Servoin, A. Baratoff, J. G. Bednorz, and G. Binnig, "Temperature dependence of plasmons in Nb-doped $SrTiO_3$" Phys. Rev. B **47**, 8187-8194. (1993)

[80] J. F. Schooley, W. R. Hosler, E. Ambler, J. H. Becker, M. L. Cohen, and C. S. Koonce, "Dependence of the Superconducting Transition Temperature on Carrier Concentration in Semiconducting $SrTiO_3$" Phys. Rev. Lett. **14**, 305-307. (1965)

[81] T. Zhao, H. Lu, F. Chen, S. Dai, G. Yang, and Z. Chen, "Highly conductive Nb doped $SrTiO_3$ epitaxial thin films grown by laser molecular beam epitaxy" J. Cryst. Growth **212**, 451-455. (2000)

[82] G. L. Yuan, J. M. Liu, K. B. Kishi, H. L. W Chan, C. L Choy, and Z. G Liu. "Possible mechanism for tunneling magnetoresistance in $La_{0.9}Ba_{0.1}MnO_3$ / Nb-doped $SrTiO_3$ p^+–n junctions" Solid State Commun. **131**, 383-387.

(2004)

[83] T. Muramatsu, Y. Muraoka, T. Yamauchi, J. Yamaura, and Z. Hiroi, "Photocarrier injection to perovskite manganites" J. Magn. Magn. Mater **272-276**, e787-e788. (2004)

[84] H. B. LÜ, S. Y. Dai, Z. H. Chen, L. f. Liu, H. Z. Guo, W. F. Xiang, Y. Y. Fei, M. He, Y. L. Zhou, and G. Z. Yang, "Colossal Magnetoresistive p-n Junctions of Te-Doped $LaMnO_3$/Nb-doped $SrTiO_3$" Chin. Phys. Lett. **20**, 137-140. (2003)

[85] H. Tabata, H. Tanaka, and T. Kawai, "Formation of artificial $BaTiO_3/SrTiO_3$ superlattices using pulsed laser deposition and their dielectric properties" Appl. Phys. Lett. **65**, 1970-1972. (1994)

[86] H. B. Lu, G. Z. Yang, Z. H. Chen, S. Y. Dai, Y. L. Zhou, K. J. Jin, B. L. Cheng, M. He, L. F. Liu, H. Z. Guo, Y. Y. Fei, W. F. Xiang, and L. Yan, "Positive colossal magnetoresistance in a multilayer p–n heterostructure of Sr-doped and Nb-doped" Appl. Phys. Lett. **84**, 5007-5009. (2004)

[87] O. Nakagawaraa, T. Shimutaa, T. Makinoa, S. Araia, H. Tabatab, and T. Kawaib, "Dependence of dielectric and ferroelectric behaviors on growth orientation in epitaxial $BaTiO_3/SrTiO_3$ superlattices" Vacuum, **66**, 397-401. (2002)

[88] C. Mitra, P. Raychaudhuri, G. Köbernik, K. Dörr, K. H. Müller, L. Schultz, and R. Pinto, "p–n diode with hole- and electron-doped lanthanum manganites" Appl. Phys. Lett. **79**, 2408-2410. (2001)

[89] D. M. Newns, J. A. Misewich, C. C. Tsuei, A Gupta, B. A. Scott, and A. Schrott, "Mott transition field effect transistor" Appl. Phys. Lett. **73**, 780-782. (1998)

[90] T. Shimizu, and H. Okushi, "Intrinsic electrical properties of Au/$SrTiO_3$

Schottky junctions" J. Appl. Lett. **85**, 7244-7251. (1999)

[91] H. Tanaka, J. Zhang, and T. Kawai, "Giant electric field modulation of double exchange ferromagnetism at room temperature in the Perovskite manganite/titanate p-n junction" Phys. Rev. Lett. **88**, 0272041-0272044. (2002)

[92] H. B. Lu, S. Y. Dai, Z. H. Chen, Y. L. Zhou, B. L. Cheng, K. J. Jin, L. F. Liu, G. Z. Yang, and X. L. Ma, "High sensitivity of positive magnetoresistance in low magnetic field in perovskite oxide p-n junctions" Appl. Phys. Lett. **86**, 32502-1-32502-3. (2005)

[93] M. O' Keeffe, "Materials science: Edge effects" Nature, **419**, 28-29. (2002)

[94] G. Z. Liu, C. Wang, C. C. Wang, J. Qiu, M. He, J. Xing, K. J. Jin, H. B. Lu, and G. Z. Yang, "Effects of interfacial polarization on the dielectric properties of $BiFeO_3$ thin film capacitors" Appl. Phys. Lett. **92**, 122903-1-122903-3. (2008)

[95] P. F. Garcia, R. S. McLean, and M. H. Reilly, "High-performance ZnO thin-film transistors on gate dielectrics grown by atomic layer deposition" Appl. Phys. Lett. **88**, 123509-1-123509-3. (2006)

[96] Y. T. Liu, S. Y. Chen, and H. Y. Lee, "Characteristics of Highly Orientated $BiFeO_3$Thin Films on a $LaNiO_3$-coated Si Substrate by RF Sputtering ", Thin Solid Films **518**, 7412-7415. (2010)

[97] Y. Wang, Y. Lin, and C. W. Nan, "Thickness dependent size effect of $BiFeO_3$ films grown on $LaNiO_3$-buffered Si substrates" J. Appl. Phys. **104**, 123912-1-123912-4. (2008)

[98] S. K. Sinha, E. B. Sirota, S. Garoff, and H. B. Stanley, "X-ray and neutron scattering from rough surfaces" Phys. Rev. B **38**, 2297-2311. (1988)

[99] M. Alvisi, A. Rizzo, L. Tapfer, and L. Vasanelli, "X-ray reflectivity analysis

of thin TiN and TiO_xN_y films deposited by dual-ion-beam sputtering on (100)Si substrates" Thin Solid Films **298**, 130-134. (1997)

[100] T. V. C. Rao, and M. K. Sanyal, "The effect of growth defects on the X-ray reflectivity of multilayer systems" Appl. Surf. Sci. **74**, 315-321. (1994)

[101] A. Logothetidis, S. Stergioudis, and G. Patsalas, "Oxidation and structural changes in fcc TiNx thin films studied with X-ray reflectivity" Surf. Coat. Technol. **100**, 295-299. (1998)

[102] J. D. Shindler, and R. M. Suter, "Moderate resolution x-ray reflectivity" Rev. Sci. Instrum. **63**, 5343-5347. (1992)

[103] L. G. Parratt, "Surface Studies of Solids by Total Reflection of X-Rays" Phys. Rev. **95**, 359-369. (1954)

[104] D. K. Bowen, and B. K. Tanner, "Characterization of engineering surfaces by grazing-incidence X-ray reflectivity" Nanotechnology **1993**, *4*, 175-182.

[105] 徐嘉鴻, "Introduction to synchrotron radiation sources" 國家同步輻射研究中心.

[106] http://en.wikipedia.org/wiki/Insertion_device

[107] http://en.wikipedia.org/wiki/Wiggler_(synchrotron)

[108] Nicholas A. Geisse, "AFM and Combined Optical Techniques" Materials Today **12**, 40-45. (2009)

[109] Spence, John C. H. "Experimental high-resolution electron microscopy" New York: Oxford U. Press. ISBN 0-19-505405-9. **(1988) [1980]**

[110]http://en.wikipedia.org/wiki/Transmission_electron_microscopy#cite_note-rose-20

[111] H. Stragier, J. O. Cross, J. J. Rehr, and L. B. Sorensen, "Diffraction

anomalous fine structure: A new x-ray structural technique" Phys. Rev. Lett. **69**, 3064-3067. (1992)

[112] L. B. Sorensen, J. O. Cross, M. Newville, B. Ravel, J. J. Rehr, H. Stragier, C. E. Bouldin, and J. C. Woicik, "In Resonant Anomalous X-Ray Scattering: Theory and Applications" G. Materlik, C. J. Sparks, K. Fischer, Eds.; Elsevier Science North-Holland: Amsterdam, The Netherlands, p 389. (1994)

[113] Y. T. Liu, S. J. Chiu, H. Y. Lee, and S. Y. Chen, "Preparation of $BiFeO_3/LaNiO_3$ Multiferroic Oxide Superlattice Structure by RF Sputtering" Surf. Coat. Technol. **206**, 1666-1672. (2011)

[114] http://en.wikipedia.org/wiki/Secondary_ion_mass_spectrometry

[115] W. Känzig. "Ferroelectrics and Antiferroelectrics". In Frederick Seitz, T. P. Das, D. Turnbull, E. L. Hahn. Solid State Physics 4. Academic Press. p. 5. ISBN 0-12-607704-5. (1957)

[116] M. Lines, and A. Glass. "Principles and applications of ferroelectrics and related materials" Clarendon Press, Oxford. ISBN 0-19-851286-4. (1979)

[117] TF Analyzer 2000E Hysteresis Software Version 2.3, aixACCT.

[118] H. Naganuma, Y. Inoue, and S. Okamura, "Estimation of Leakage Current Density and Remanent Polarization of $BiFeO_3$ Films with Low Resistivity by Positive, Up, Negative, and Down Measurements" Jpn. J. Appl. Phys **47**, 5558-5560. (2008)

[119] J. Wu, and J. Wang, "$BiFeO_3$ thin films of (1 1 1)-orientation deposited on $SrRuO_3$ buffered $Pt/TiO_2/SiO_2/Si$(1 0 0) substrates" Acta Materialia **58**, 1688-1697. (2010)

[120] J. S. Cross, S. H. Kim, S. Wada, and A. Chatterjee, "Characterization of Bi and Fe co-doped PZT capacitors for FeRAM" Sci. Technol. Adv.

Mater. **11**, 044402-1-044402-6. (2010)

[121] S. M. Feng, Y. S. Chai, J. L. Zhu, N. Manivannan, Y. S. Oh, L. J. Wang, Y. S. Yang, C. Q. Jin, and K. H. Kim, "Determination of the intrinsic ferroelectric polarization in orthorhombic $HoMnO_3$" New J. Phys. **12**, 073006-1-073006-13. (2010)

[122] A. R. Chaudhuri, and S. B. Krupanidhi, "Investigation of true remnant polarization response in heterostructured artificial biferroics" Solid State Commun. **150**, 660-662. (2010)

[123] H. Chen, and S. M. Heald, "Concentration profiling using x-ray reflectivity: Application to Cu-Al interfaces" J. Appl. Phys. **66**, 1793-1799. (1989)

[124] M. Sugawara, M. Kondo, S. Yamazaki, and K. Nakajima, "Exact determination of superlattice structures by small-angle x-ray diffraction method" Appl. Phys. Lett. **52** ,742-744. (1988)

[125] S. K. Sinha, "Reflectivity using neutrons or X-rays? A critical comparison" Physica B **173**, 25-34. (1991)

[126] Y. Yoneda, "Anomalous Surface Reflection of X Rays" Phys. Rev. **131**, 2010-2013. (1963)

[127] S. Y. Tseng, and C. H. Lee, "X-Ray Reflectivity Measurement of a Silicon Oxide Layer on Si Wafer" J. Vac. Soc. ROC. **6**, 4-11. (1993)

[128] B. Berini, N. Keller, Y. Dumont, E. Popova, W .Noun, M. Guyot, J. Vigneron, A. Etcheberry, N. Franco, and R.M.C. da Silva, "Reversible phase transformation of $LaNiO_{3-x}$ thin films studied in situ by spectroscopic ellipsometry" Phys. Rev. B **76**, 205417-1-205417-9. (2007)

[129] J. W. Matthews, and A. E. Blakeslee, "Defects in epitaxial multilayers: I.

Misfit dislocations" J. Cryst. Growth **27**, 118-125. (1974)

[130] Y. C. Liang, T. B. Wu, H. Y. Lee, and Y. W. Hsieh, "Structural characteristics of epitaxial $BaTiO_3/LaNiO_3$ superlattice" J. Appl. Phys. **96**, 584-589. (2004)

[131] U. Pietsch, H. Metzger, S. Rugel, B. Jenichen, and I. K. Robinson, "Depth -resolved measurement of lattice relaxation in $Ga_{1-x}In_xAs/GaAs$ strained layer superlattices by means of grazing-incidence x-ray diffraction" J. Appl. Phys. **74**, 2381-2387. (1993)

[132] D. Fuchs, M. Adam, P. Schweiss, and R. Schneider, "Dielectric tunability of coherently strained $LaAlO_3/SrTiO_3$ superlattices" J. Appl. Phys. **91**, 5288-5295. (2002)

[133] B. Mikolajczyk, M. Bedzyk, J. Klug, and J. C. Lin, "X-ray Characterization of a multiferroic bismuth ferrite thin film" Nanoscape **5**, 94-105. (2008)

[134] J. Kim, Y. Kim, Y. S. Kim, J. Lee, L. Kim, and D. Jung, "Large nonlinear dielectric properties of artificial $BaTiO_3/SrTiO_3$ superlattices" Appl. Phys. Lett. **80**, 3581-3583. (2002)

[135] H. Béa, M. Bibes, A. Barthélémy, K. Bouzehouane, E. Jacquet, A. Khodan, J. P. Contour, S. Fusil, F. Wyczisk, A. Forget, D. Lebeugle, D. Colson, and M. Viret, "Influence of parasitic phases on the properties of $BiFeO_3$ epitaxial thin films" Appl. Phys. Lett. **87**, 072508-1-072508-3. (2005)

[136] R. Ranjith, W. Prellier, J. W. Cheah, J. Wang, and T. Wu, "dc leakage behavior and conduction mechanism in $(BiFeO_3)_m(SrTiO_3)_m$ superlattices" Appl. Phys. Lett. **92**, 232905-1-232905-3. (2008)

[137] O. I. Lebedev, J. F. Hamet, G. Van Tendeloo, V. Beaumont, and B. Raveau, "Structure and properties of the $YBa_2Cu_3O_{7-x}/LaAlO_3$ superlattices" J. Appl. Phys. **90**, 5261-5267. (2001)

[138] H. H. Lee, M. S. Yi, H. W. Jang, Y. T. Moon, S. J. Park, D. Y. Noh, M. Tang, and K. S. Liang, "Determination of absolute indium content in InGaN/GaN multiple quantum wells using anomalous x-ray scattering" Appl. Phys. Lett. **81**, 5120-5122. (2002)

[139] K. Numata, "Justification of the Schottky emission model at the interface of a precious metal and a perovskite oxide with dilute oxygen vacancies" Thin Solid Films **515**, 2635-2643. (2006)

[140] J. Wang, T. Zhang, J. Xiang, and B. Zhang, "High-tunability and low-leakage current of the polycrystalline compositionally graded $(Ba,Sr)TiO_3$ thin films derived by a sol–gel process" Mater. Chem. Phys. **108**, 445-448. (2008)

[141] S. P. Alpay, I. B. Misirlioglu, V. Nagarajan, and R. Ramesh, "Can interface dislocations degrade ferroelectric properties?" Appl. Phys. Lett. **85**, 2044-2046. (2004)

[142] S. Bose, and S. B. Krupanidhi, "Improved ferroelectric and leakage properties in symmetric $BiFeO_3/SrTiO_3$ superlattice" Appl. Phys. Lett. **90**, 212902-1-212902-3. (2007)

[143] S. Mathews, R. Ramesh, T. Venkatesan, and J. Benedetto "Ferroelectric Field Effect Transistor Based on Epitaxial Perovskite Heterostructures" Science **276**, 238-240. (1997)

[144] G. Catalan, and J. F. Scott, "Physics and Applications of Bismuth Ferrite" Adv. Mater. **21**, 2463-2485. (2009)

[145] K. Y. Yun, M. Noda, and M. Okuyama, "Prominent ferroelectricity of $BiFeO_3$ thin films prepared by pulsed-laser deposition" Appl. Phys. Lett. **83**, 3981-3983. (2003)

[146] X. Qi, J. Dho, R. Tomov, M. G. Blamire, and J. L. MacManus-Driscoll, "Greatly reduced leakage current and conduction mechanism in aliovalent-ion-doped $BiFeO_3$" Appl. Phys. Lett. **86**, 062903-1-062903-3. (2005)

[147] V. Shelke, V. N. Harshan, S. Kotru, and A. Gupta, "Effect of kinetic growth parameters on leakage current and ferroelectric behavior of $BiFeO_3$ thin films" J. Appl. Phys. **106**, 104114-1-104114-7. (2009)

[148] H. J. Liu, K. Yao, P. Yang, Y. H. Du, Q. He, Y. L. Gu, X. L. Li, S. H. Wang, X. T. Zhou, and J. Wang, "Thickness-dependent twinning evolution and ferroelectric behavior of epitaxial $BiFeO_3$ (001) thin films" Phys. Rev. B **82**, 064108-1-064108-6. (2010)

[149] A. I. Chou, K. Lai, K. Kumar, P. Chowdhury, and J. C. Lee, "Modeling of stress-induced leakage current in ultrathin oxides with the trap-assisted tunneling mechanism" Appl. Phys. Lett. **70**, 3407-3409. (1997)

[150] Y. T. Liu, S. Y. Chen, and H. Y. Lee, "Fabrication and ferroelectric properties of $BiFeO_3/LaNiO_3$ artificial superlattice structures grown by radio-frequency magnetron-sputtering" Thin Solid Films **529**, 66-70. (2013)

[151] C. S. Ku, H. Y. Lee, and J. M. Huang, "Annealing effect on the optical response and interdiffusion of n-ZnO/p-Si (111) heterojunction grown by atomic layer deposition" Appl. Phys. Lett. **97**, 181915-1-181915-3. (2010)

[152] Y. Wang, Y. Lin, and C. W. Nan, "Thickness dependent size effect of $BiFeO_3$ films grown on $LaNiO_3$-buffered Si substrates" J. Appl. Phys. **104**,

123912-1-123912-4. (2008)

[153] R. Y. Zheng, J. Wang, and S. Ramakrishna, "Electrical and magnetic properties of multiferroic $BiFeO_3/CoFe_2O_4$ heterostructure" J. Appl. Phys. **104**, 034106-1-034106-6. (2008)

[154] C. S. Yeh, and J. M. Wu, "Characterization of Pt/multiferroic $BiFeO_3$ /(Ba,Sr)TiO_3/Si stacks for nonvolatile memory applications" Appl. Phys. Lett, **93**, 154101-1-154101-3. (2008)

[155] Y. H. Chu, T. Zhao, M. P. Cruz, Q. Zhan, P. L. Yang, L. W. Martin, M. Huijben, C. H. Yang, F. Zavaliche, H. Zheng, and R. Ramesh, "Ferroelectric size effects in multiferroic $BiFeO_3$ thin films" Appl. Phys. Lett. **90**, 252906-1-252906-3. (2007)

[156] S. Jose, In "*The International Technology Roadmap for Semiconductors"*; Front End Processes Section; Semiconductor Industry Association: CA; pp 7-26. (2011)